الجمهورية الجزائرية الديمقراطية الشعبية

People's Democratic Republic of Algeria

وزارة التعليم العالي والبحث العلمي

Ministry of Higher Education and Scientific Research


جـــامعة زيان عاشور بالجلفة

**Ziane Achour University of Djelfa**

كلية العلـــوم والتكنولوجـــيا

**Faculty of Science and Technology**

Department: Electrical Engineering


**Order N°: ... /2026**

Defense authorization N°: …. / 2026

# DOCTORAL THESIS

3rd Cycle Doctoral (D-LMD)

Presented by


**Kellal Cherif**


With a view to obtaining the doctoral degree in 3rd Cycle Doctoral (D-LMD)

Branch: Electrical Engineering

Specialty: Electrical engineering

**Topic**

## Investigation on the control of a hybrid renewable energy system connected to HVDC-VSC

Supported, on .. /../ 2026, before the jury composed of:

| Last and first name | Grade | Institution of affiliation | Designation |
|---|---|---|---|
| Mr. Boudiaf Mohamed | Prof | University of Djelfa | President |
| Mr. Lakhdar MAZOUZ | Prof | University of Djelfa | Supervisor |
| Mr. Abdellah KOUZOU | Prof | University of Djelfa | Co-Supervisor |
| Mr. Hadjadj Abdelchafik | Prof | University of Laghouat | Examiner |
| Mr. Bendjedia Bachir | MCA | University of Laghouat | Examiner |
| Mr. Toual Belkacem | Prof | University of Djelfa | Examiner |

**Djelfa University, FST- 2026**

**Acknowledgement**

In the name of Allah, the Most Merciful, the Most Compassionate.
All praise belongs to Allah, Who grants patience in hardship, clarity in doubt, and light in the darkest paths. Without His grace, no effort finds completion and no journey finds meaning.

To the memory of my late mother—whose silent strength and enduring love guided me through every step—and to my father, whose presence has been both a guide and a steadfast support, I dedicate this work with deepest gratitude. To my family, friends, and loved ones, who stood by me with patience and encouragement, I remain profoundly thankful.

I owe special thanks to my supervisor, **Prof. Lakhdar Mazouz**, and to my assistant supervisor, **Prof. Abdellah Kouzou**, for their invaluable guidance and support. I am also grateful to **Dr. Ali Teta**, whose assistance was of great importance, to **Prof. Haitham Abu-Rub** for his hospitality at the Smart Grid Center–Qatar, Texas A&M University at Qatar, and to **Prof. Matilde Pietrafesa** and **Prof. Mario Versaci** for their warm welcome and inspiring environment at the *Energy and Environment Laboratory, Mediterranean University, Italy.*

***I close with a reflection: Falling is not the end; it is the ground from which we rise—wiser, stronger, and more determined to carry hope forward.***

**Cherif Kellal**

# Table of Contents

# List of Figures

# List of Tables

# Nomenclature

**List of abbreviations**

ANN Artificial Neural Network

CNN Convolutional Neural Network

CSC Current Source Converter

DO Dandelion Optimization

FFNN Feed Forward Neural Network

FLC Fuzzy Logic Control

GMPP Global Maximum Power Point Tracking

GSC Grid Side Converter

GWO Grey Wolf Optimization

HRES Hybrid Renewable Energy System

HVAC High Voltage Alternative Current

HVDC High Voltage Direct Current

IC Incremental Conduction

IEA International Energy Agency

IGBT Insulated Gate Bipolar Transistor

LCC Line Commutated Converter

MOSFET Metal Oxide Semiconductor Field-Effect Transistor

MPPT Maximum Power Point Tracking

MSC Machine Side Converter

MSE Mean Squared Error

MTDC Multi Terminal Direct Current

NPC Neutral Point Clamped

OTC Optimal Torque Control

P&O Perturbation and Observation

PCC Point of Common Coupling

PI Proportional Integral

PLL Phase Locked Loop

PMSG Permanent Magnet Synchronous Generator

PSF Power Signal Feedback

PSO Particle Swarm Optimization

PV Photovoltaic

PWM Pulse With Modulation

RBFN Radial Basis Function Network

RNN Recurrent Neural Network

SRF Synchronous Reference Frame

SSE Sum Squared Error

STC Standard Test Condition

SVPWM Space Vector Pulse With Modulation

TSR Tip Speed Ratio

VOC Voltage Open Circuit

VSC Voltage Source Converter

VSI Voltage Source Inverter

WECS Wind Energy Conversion System

**List of symbols**

$\beta$ Blade pitch angle

$\lambda$ Tip speed ratio

$\lambda_f$ Permanent magnet flux

$\lambda_{Gd}, \lambda_{Gq}$ Stator flux in $dq$ frame

$\omega_R$ Angular speed

$\rho$ Air density

$\theta_G, \theta_R$ Generator and rotor rotational angles

$A$ Ideality factor of the diode

$C_p$ Power factor

$C_{in}, C_{out}$ Input capacitor and Output capacitor

$D$ DC-DC boost duty ratio

$D_G, D_R$ Generator and rotor damping

$f_{sw}$ Switching frequency

$G, G_n$ Actual and nominal irradiance

$I_0$ Diode saturation current

$I_d$ Current of Shockley diode

$I_F$ Current generated by the wind turbine

$i_{fabc}$ Filter currents

$i_{Gd}, i_{Gq}$ Stator currents in $dq$ frame

$I_{ph}$ Photocurrent generated by incident light

$I_{pv}$ Current generated by the PV panel

$i_{sabc}$ Source currents

$I_{scn}, V_{ocn}$ Nominal short-circuit current and nominal open circuit voltage

$J_G, J_R$ Moments of inertia for rotor and generator wind turbines

$K$ Shaft stiffness

$L$ Inductor

$L_f, R_f$ Filter inductor and resistance

$L_{fabc}, R_{fabc}$ Coupling filter inductance and resistance

$L_{Gd}, L_{Gq}$ Stator inductance in $dq$ frame

$N_p, N_s$ Number of parallel and series cells

$p$ Number of pole pairs of the generator

$P_G$ Electric power

$P_m$ Mechanical power

$P_{aero}$ Aerodynamic power

$P_{pv}$ PV power

$q$ Charge of an electron

$R_0$ Equivalent load resistance

$R_G$ Equivalent stator resistance

$R_s$ Series resistance

$R_{sh}$ Shunt resistance

$S_a, S_b, S_c$ Control signals

$T$ Cell temperature

$T_A$ Mechanical torque

$T_G$ Electric torque

$T_n$ Nominal temperature

$T_s$ Time period

$V_\omega$ Wind speed

$V_{dc-m}$ DC-link voltage measured

$V_{dcref}$ Reference DC-link voltage

$V_{Fd}, V_{Fq}$ Grid voltages in $dq$ frame

$v_{Gd}, v_{Gq}$ PMSG voltages in $dq$ frame

$V_{in}, V_{out}$ Input voltage and Output voltage

$V_{pv}$ PV voltage

$V_{pv}$ Voltage across the cell

$V_{Wd}, V_{Wq}$ Dynamic voltages in $dq$ frame

# General introduction

The continuous rise in global energy demand, driven by population growth, industrialization, and technological development, has made energy one of the most essential elements for sustaining modern life. It is indispensable not only for basic human needs, such as cooking, heating, cooling, and lighting, but also for economic development, supporting vital sectors including agriculture, industry, services, and transportation. However, the heavy reliance on conventional fossil fuels to meet these needs has resulted in serious environmental concerns, such as greenhouse gas emissions and climate change, in addition to challenges related to resource depletion and energy security [1].

In response to these challenges, renewable energy sources such as solar and wind power have emerged as viable and sustainable alternatives. Their abundance, environmental compatibility, and potential to reduce dependence on conventional fuels make them key contributors to the future global energy mix. However, the integration of renewable energy into existing electrical grids poses several challenges, particularly due to the intermittent and fluctuating nature of these resources. This has motivated the development of advanced energy transmission and control systems to ensure efficient, stable, and reliable operation.

Among these, high-voltage direct current (HVDC) transmission systems based on voltage source converters (VSCs) have become increasingly attractive. Unlike conventional AC transmission, HVDC-VSC technology provides long-distance power transfer with reduced losses, independent control of active and reactive power, and enhanced grid stability. Such characteristics make HVDC-VSC systems particularly well-suited for connecting large-scale renewable energy plants, such as offshore wind farms and remote photovoltaic installations, to the main grid. Nevertheless, effective integration requires accurate system modeling and advanced control strategies to manage dynamic interactions, ensure power quality, and maintain voltage stability under variable operating conditions [2].

The efficiency of renewable energy systems is also highly dependent on their control strategies. For photovoltaic (PV) systems, maximum power point tracking (MPPT) algorithms are essential to adapt to changing irradiance and temperature conditions, thereby

maximizing energy harvesting. Similarly, wind energy systems based on permanent magnet synchronous generators (PMSGs) require robust control schemes to optimize torque, regulate DC-link voltage, and meet grid code requirements under fluctuating wind speeds. The coordination of such control techniques, particularly when combined in hybrid renewable energy systems (HRES), is critical for ensuring reliable energy generation and seamless integration with HVDC-VSC transmission networks.

Recent advances in artificial intelligence and metaheuristic optimization methods have further enhanced system performance. Techniques such as particle swarm optimization (PSO), grey wolf optimization (GWO), and dandelion-inspired optimization (DO) have been employed to enhance the accuracy, convergence speed, and overall operational stability of MPPTs in PV systems [3]. Likewise, intelligent controllers, such as feed-forward neural networks (FFNNs), have been employed to enhance the robustness of HVDC-VSC systems by improving DC-link voltage regulation and optimizing active and reactive power flow management. These approaches address the limitations of conventional controllers, particularly under rapidly changing environmental and operating conditions.

Motivated by these considerations, this thesis investigates the modeling, control, and integration of PV and wind energy sources with HVDC-VSC transmission systems. The objective is to implement effective strategies that enhance system efficiency, stability, and reliability. The dissertation is organized into four main chapters:

**Chapter 1** provides an overview of renewable energy resources, focusing on solar and wind power, and discusses their integration with HVDC-VSC transmission systems as a solution for long-distance and large-scale energy transfer. **Chapter 2** presents the modeling and analysis of PV systems, wind energy systems, and HVDC-VSC transmission, highlighting the main challenges of hybrid integration. **Chapter 3** examines advanced control strategies for PV and wind energy systems, including MPPT techniques for PV and control schemes for PMSG-based wind turbines, as well as the role of VSC-HVDC systems in hybrid renewable energy integration. **Chapter 4** focuses on the application of optimization-based MPPT methods and intelligent control strategies for HVDC-VSC systems, evaluating their performance under varying environmental conditions.

# Chapter I

# State of the art: Hybrid renewable energy and HVDC-VSC system

## I.1 Introduction

Since its discovery, energy has become an essential part of daily life and directly impacts climate change and development. It is necessary to meet the increasing basic human needs such as cooking, Heating, cooling, lighting, and boiling water, in addition to supporting the economic aspect and facilitating production such as agriculture, industry, services, transportation, and all activities that require an energy source.

At present, many nations rely heavily on conventional sources like fossil fuels to generate a significant proportion of the global energy supply. Nonetheless, the dependence on fossil fuels poses several adverse consequences on the environment and exacerbates climate change. Given the finite and unsustainable nature of fossil fuel reserves, countries are shifting their focus towards renewable energy sources to enhance their production and diminish their reliance on traditional sources. They are promoting and facilitating the implementation of renewable energy initiatives to meet the escalating global energy demand.

Renewable energy is expected to emerge as a premier and major energy resource in the coming years, so researchers are working to develop it, increase its efficiency, and increase the quality of energy transmission. This chapter discusses renewable energies, with a focus on solar energy and wind energy as the most common sources, to present and clarify its potential as a basic source of energy in the upcoming years and decades for humanity, besides, the HVDC-VSC transmission system is discussed to demonstrate its benefits in connecting remote solar panel farms and wind turbines to the terrestrial AC power grid.

## I.2 History and statistics of renewable energies

The exploration and application of renewable energy sources have a storied history, stretching back to antiquity when civilizations utilized wind and hydropower for various mechanical operations. The genesis of contemporary renewable energy technology, however, can be traced to the latter half of the 19th century. A seminal moment in this trajectory was the establishment of the world's first commercial hydropower plant in 1882, which marked the advent of harnessing water for electricity generation [4, 5].

The development of renewable energy technologies accelerated dramatically during the 20th century, as a result of the intensive exploitation of fossil fuels [6]. The limitations of these non-renewable resources and the deleterious environmental repercussions precipitated a burgeoning interest in alternative energy sources. In the nascent stages of this shift during the 1950s and 1960s, experimental initiatives were undertaken to ascertain the feasibility of wind and solar power, effectively laying the base for future technological innovation [7].

The oil embargo of the 1970s served as a critical inflection point, as the resultant spike in oil prices and heightened cognizance of the ecological ramifications of fossil fuel dependency catalyzed a resurgence in the pursuit of renewable energy alternatives [8]. Subsequently, governments across the globe commenced substantial investments in the development and research of renewable energy technologies, culminating in pronounced enhancements in both the efficiency and economic viability of these energy sources.

By the dawn of the 21st century, exponential growth characterized the renewable energy sector, with diminishing costs and escalating investments underscoring this trend. According to (IEA), renewables accounted for approximately 15% of global electricity generation by 2020 [9].

Technological advancements in energy technologies have reduced dependence on fossil fuels. Increased public awareness of climate change has accelerated the adoption of renewable energy, underscoring its importance in addressing current energy needs and reducing human-induced climate impacts [9, 10]. Figure I.1 shows the projected trajectory of electricity production from different sources, while Figure I.2 shows the evolution of electricity

production from renewable energies.

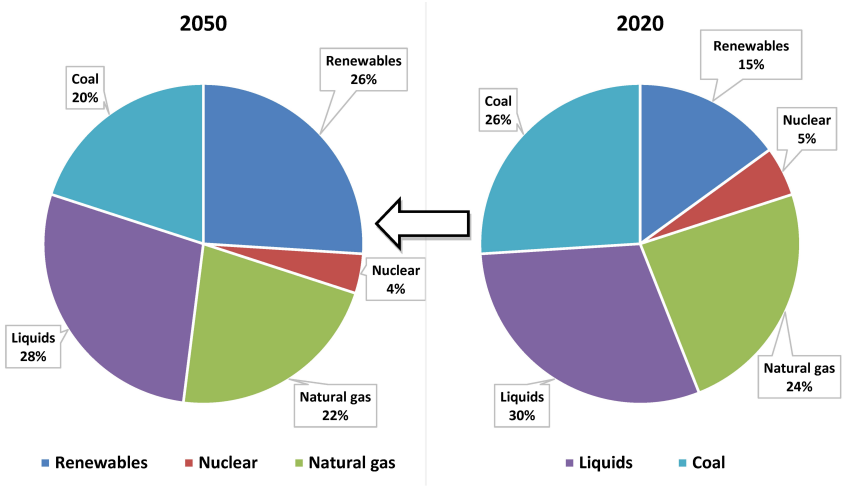


Figure I.1: Share of electricity production from different sources, Global

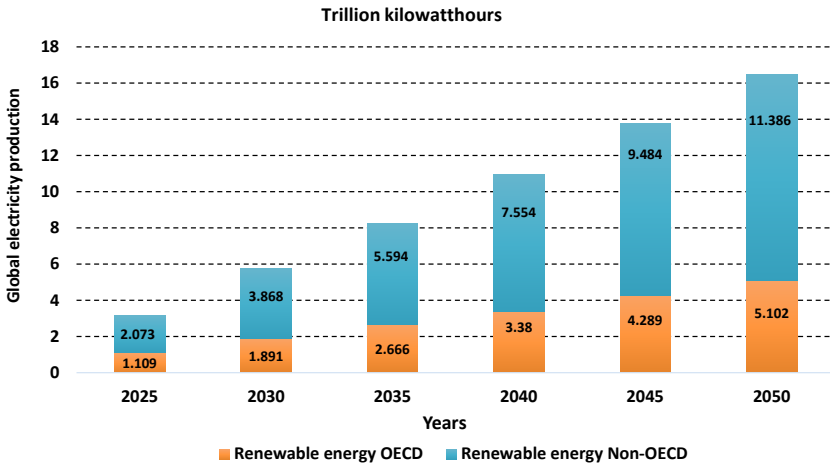


Figure I.2: World electricity generation by renewable energy

### I.2.1 Renewable Energy Benefits

The adoption of renewable energy sources offers significant environmental advantages over the conventional reliance on fossil fuels. Chiefly, the shift toward renewables facilitates a substantial diminution in the emission of greenhouse gases, which are pivotal in exacerbating global climate change phenomena [11]. The combustion of fossil fuels has been demonstrably linked to increased carbon levels within oceanic ecosystems, catalyzing a process of acidification with detrimental effects on marine biodiversity [12]. Moreover,

the implementation of renewable energy systems is conducive to the abatement of pollution, thereby contributing to the enhancement of both air quality and public health. This improvement could potentially manifest in reduced incidences of respiratory ailments, cardiovascular complications, malignancies, and reproductive health issues [13].

Beyond the reduction of atmospheric pollutants, renewable energy sources also offer a pathway to alleviate water consumption demands. Traditional power stations, including fossil fuel and nuclear power plants, are intensive users of water for cooling and other operational processes. In Germany, for instance, these power plants account for a substantial 75% of the national water demand [11]. The progression towards a renewable energy paradigm is poised to diminish water utilization, thereby contributing to the conservation of this critical resource, renewable energy, derived from inexhaustible natural resources such as sunlight, wind, and water, is replenished more rapidly than it is consumed, presenting a sustainable alternative to finite fossil fuels [7]. The array of benefits associated with the deployment of renewable energy includes:

- **Minimal emissions:** Technologies such as PV panels and wind turbines operate devoid of gas emissions [14].

- **Amelioration of air and water quality:** Renewable energy systems do not emit the noxious pollutants associated with the burning of fossil fuels, resulting in improved quality of both air and water, which has favorable implications for environmental and human health [15].

- **Enhancement of energy security:** The availability of renewable resources can mitigate the importation of fossil fuels, reducing the risk of volatile energy prices and sudden supply disruptions. disruptions [16].

- **Stimulation of employment:** The burgeoning renewable energy sector creates job opportunities in various domains, including engineering, installation, and maintenance, fostering economic advancement [17].

- **Cost-effectiveness:** The decreasing costs of renewable energy technologies have rendered them increasingly economical, often outcompeting fossil fuel-based energy generation, thus offering potential savings for consumers [18].

- **Diminished environmental impact:** Renewable energy systems typically incur a lower ecological footprint, utilizing fewer resources and generating less waste compared to their fossil fuel counterparts, which is integral to preserving natural habitats and reducing human environmental impact [19].

### I.2.2 A brief history and statistics of wind power

In the latter half of the twenty-first century, the conceptualization of wind as a viable energy source was actualized through the advent of electricity-generating windmills in both the UK and the USA circa 1887 and 1888, However, the genesis of contemporary wind energy can be traced to Denmark in 1891 with the establishment of wind turbines with horizontal-axis, and in 1897, wind turbines reached a length of 22.8 m. The sector's maturation was evident by the 1980s, marking the inception of the modern wind power industry [20]. The Figure I.3 shows the world's first and largest windmill [21].

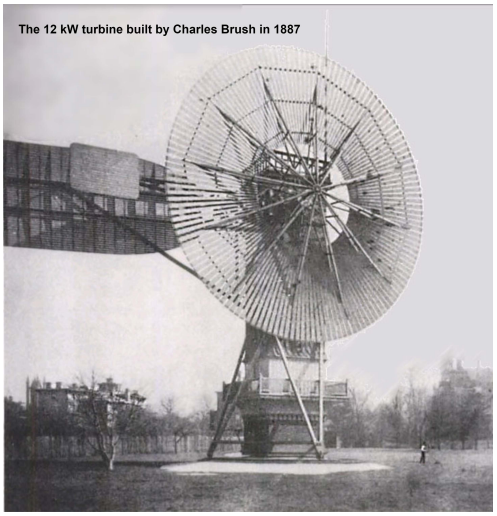


Figure I.3: The first windmill 12kW

Wind energy is widely appreciated and considered one of the most prominent and important sources of promising renewable energy, owing to its remarkable cost competi-

tiveness and undeniable environmental benefits. As of 2020, wind energy accounted for approximately 6.6% of global electricity generation [22], a testament to its rapidly growing significance in the energy landscape. Regarding specific figures, onshore wind energy played a pivotal role with a substantial contribution of 1488.5 TWh, while offshore wind energy made a noteworthy impact with a contribution of 100.1 TWh.

By Figure I.4, we can discern a notable upward trajectory in electricity generation from wind turbines across the past eight years, thereby showcasing the growing importance of this sustainable energy source.

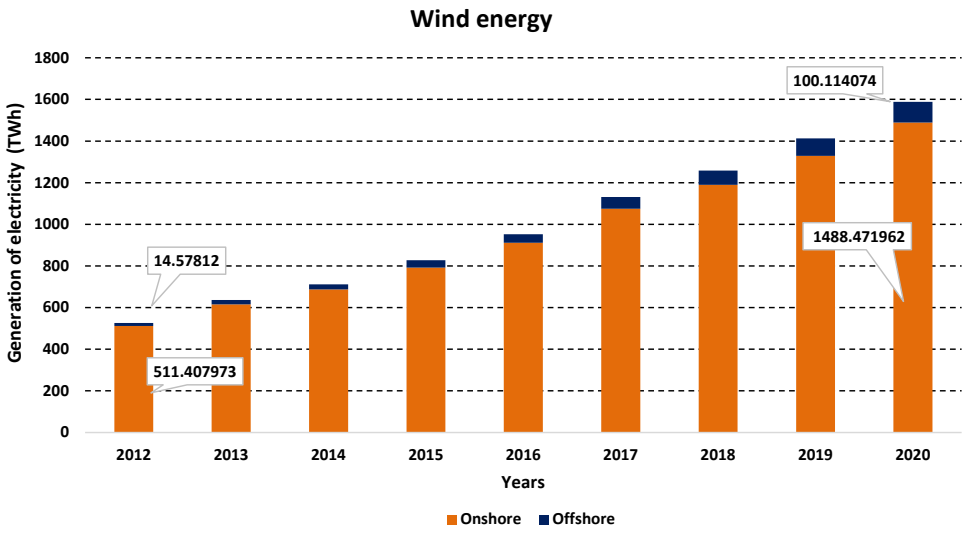


Figure I.4: World electricity generation by Wind energy

The global capacity of onshore wind energy has soared to an impressive 770 GW by the end of 2021, with an equally notable capacity of approximately 54.3 GW for offshore wind energy. Remarkably, this represents an 11% surge in capacity for both technologies when compared to the preceding year [23]. Figure I.5, which offers a comprehensive view of the total installed capacity of electricity from wind turbines in the world throughout the past decade.

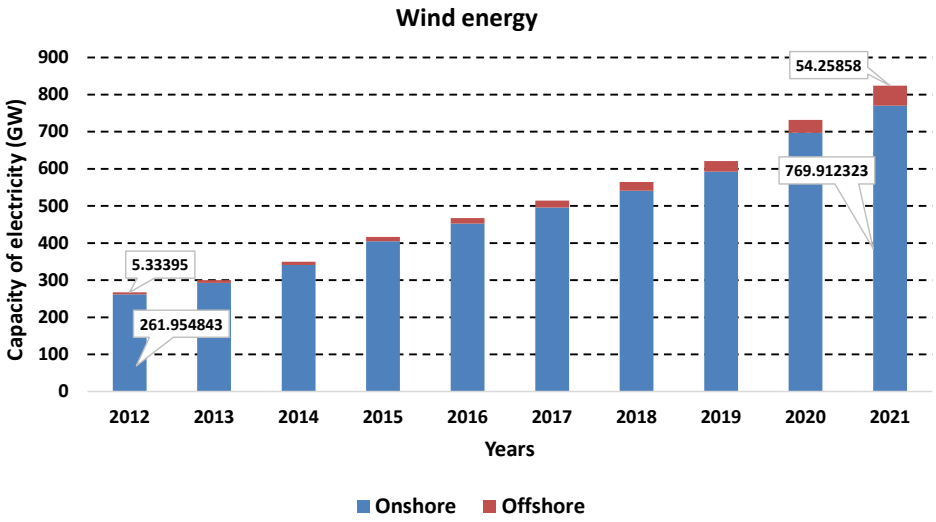


Figure I.5: Total installed capacity of electricity by wind turbines

This analysis leads us to the overarching conclusion that this growth is poised to persist and even intensify in the foreseeable future, as the IEA, with great confidence, predicts that the global capacity of wind energy will achieve an astonishing 1,110 GW by the year 2025, subsequently escalating to an overwhelming 2,110 GW by 2030 [24]. Based on these compelling figures, through Figure I.6 and I.7, it becomes apparent that China and the US dominate as the most prominent and fiercely competitive nations in this emerging field of renewable energy, as emphasized by the latest data from the IREA [25].

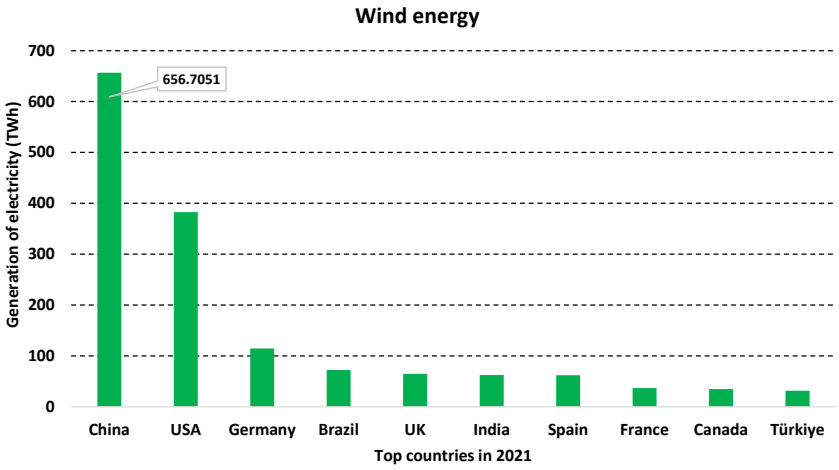


Figure I.6: Top 10 countries of electricity generation by wind turbines

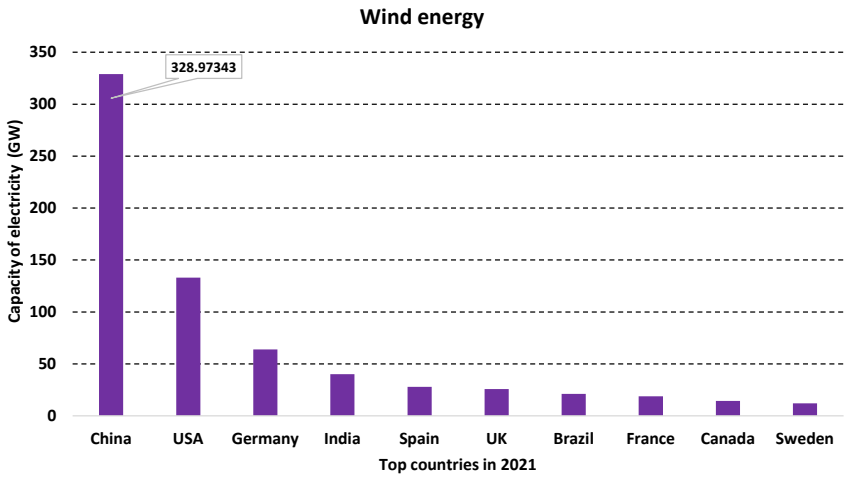


Figure I.7: Top 10 countries of installed capacity of electricity by wind turbines

The price competitiveness of wind energy is a key element driving its rise. According to the IEA, the levelized cost of electricity produced by onshore wind has undergone a significant fall of 69% during 2010. Consequently, it has emerged as one of the most economically feasible sources of electricity in several. Offshore wind is likewise heading toward cost competitiveness, experiencing a drop of 30% between 2015 and 2020 [26]. The combination of this cost competitiveness alongside supportive policy frameworks and ongoing technological advancements has led to substantial expansion within the sector.

### I.2.3 Categories and construction of wind energy

From the Figure I.8, the categories of wind energy systems can be classified according to the specific types of wind turbines utilized and their respective applications, which can be described as follows:

1. **Horizontal-Axis Wind Turbines:** Common turbines with a horizontal rotor shaft and three blades are used in utility and residential settings for high efficiency and substantial electricity generation.

2. **Vertical-Axis Wind Turbines:** Turbines with a vertical rotor shaft, that captures the wind from any direction. They are suited for urban or turbulent environments due to easier maintenance and less wind direction dependence.

3. **Offshore Wind Turbines:** Large turbines installed in water, generating more power from stronger, consistent winds and benefiting from fewer land-based obstacles.

4. **Onshore wind turbines:** These are large, land-mounted turbines that are typically installed in locations with strong, sustainable airflow and are less expensive than offshore turbines, as they do not require the infrastructure for installation in the water.

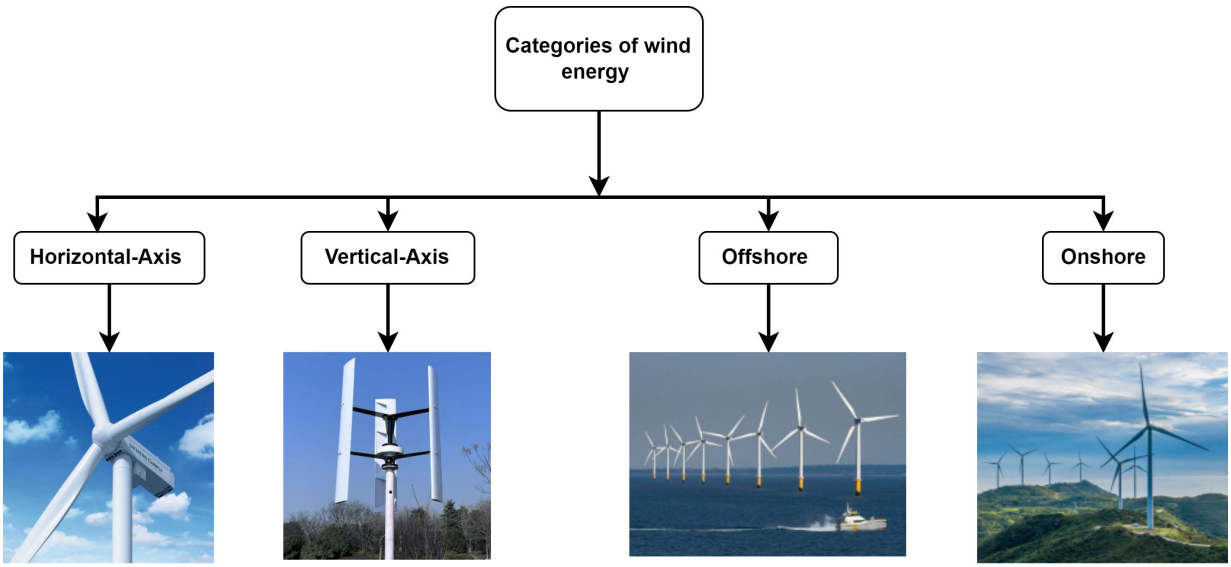


Figure I.8: Categories and construction of wind energy

### I.2.4 Advantages and disadvantages of wind power

Wind energy represents a swiftly expanding sector within renewable energy, holding substantial promise for substantial reductions in emissions and decreased reliance on fossil fuels. Wind energy utilization has exhibited a consistent growth trajectory over recent decades, propelled by advancements in technology, cost efficiencies, and supportive governmental policies. Nevertheless, like any energy source, it is accompanied by advantages and disadvantages necessitating thoughtful evaluation, the most important of which are summarized in the table I.1.

| Advantages | Disadvantages |
|---|---|
| **Reducing dependence on fossil fuels**: Wind energy lowers reliance on fossil fuels by producing electricity without greenhouse gas emissions. | **Intermittency of wind energy**: Wind energy's variability due to changing weather and wind speeds complicates electricity production forecasting and grid integration. |
| **Positive environmental impact**: Wind energy benefits the environment by avoiding habitat destruction, reducing toxic pollution, using less land than other energy sources, and improving air quality, which results in fewer respiratory and cardiovascular diseases. | **Impact on wildlife**: Wind turbines can negatively impact wildlife, such as fires caused by falling equipment and bird collisions. |
| **Economic stimulus**: Wind farms boost local economies by creating jobs in turbine manufacturing, installation, and maintenance, and enhance energy security by diversifying energy sources and mitigating fossil fuel price volatility. | **Noise pollution**: Wind turbines can generate noise pollution, which can be a concern for people living near wind farms. |
| **Energy independence**: Countries can achieve energy independence and reduce their dependence on energy imports by utilizing wind energy. | **Visually undesirable**: Some individuals find wind turbines visually unappealing and may oppose having wind farms in their areas. |

Table I.1: Advantages and disadvantages of wind power

### I.2.5 A brief history and statistics of PV system

In 1954, scientists from Bell Labs developed the first efficient PV panel, creating a silicon solar cell with 6% efficiency, representing a major advance in solar technology. The panel was demonstrated by operating a radio transmitter and a Ferris wheel. Before that, in 1883, Charles Fritz made the first solar cell using selenium, but it was low efficiency (1-2%) and impractical. The development of the silicon cell in the 1950s is considered the real breakthrough of modern PV technology [27], the Figure I.9 shows the first solar panels on the roof of New York City [28].

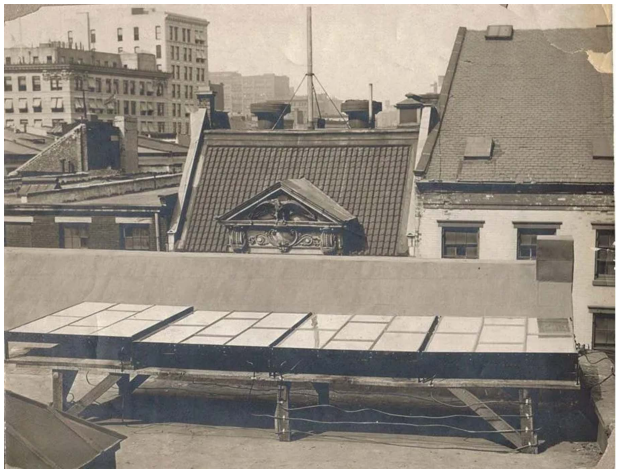

Figure I.9: The first installed solar panels

PV systems have seen significant growth in recent years as a renewable energy source. According to the IEA, global PV capacity reached 855 GW by the end of 2021, an almost 16.5% increase from last year. Figure I.10 depicts the rising expansion of electricity capacity in PV within the last ten years, While global electricity generation was approximately at about 831TWh in 2020, Figure I.11 also shows the rising trend of electricity generation from PV energy. This is due to the growth of the PV industry has been driven by declining costs and increasing efficiency of PV systems, as well as the increasing urgency to reduce carbon emissions.

PV energy is used in many applications such as buildings and factories, grid-connected systems, and off-grid systems in remote areas, elucidating the surge in the proliferation of this energy source.

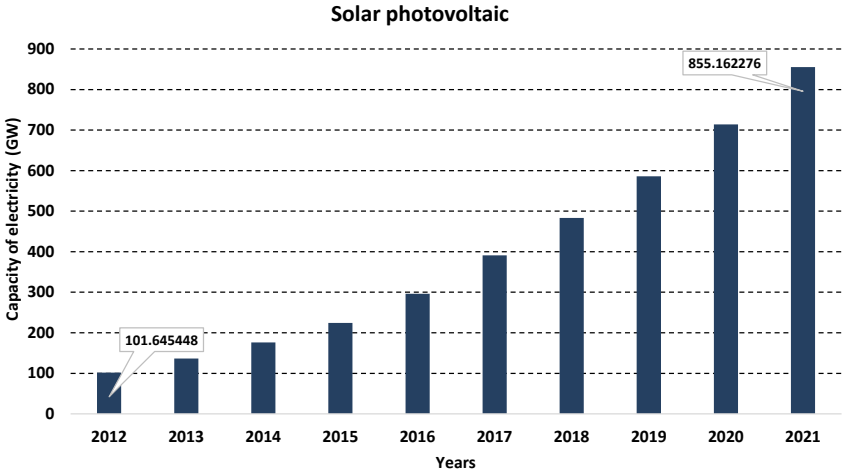


Figure I.10: World electricity capacity by PV

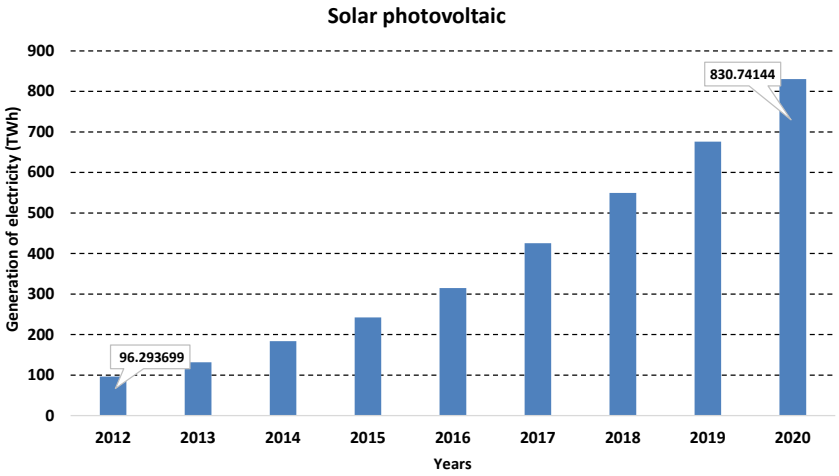


Figure I.11: World electricity generation by PV

China leads globally in PV power with over 306 GW, accounting for nearly half of the world's total installed capacity. The US, Europe, and Japan are also important markets for PV energy. Figure I.12 highlights the ten most important countries in this field in 2021, while Figure I.13 shows the global ranking in electricity generation and also indicates that China is a strong competitor in this field with a generating capacity of 327.5 TWh in 2021. The International Energy Agency (IEA) expects PV to play a crucial role in the global demand for energy in the coming decades, as the agency expects PV capacity to reach 4,000 GW by 2030, which is a logical value in light of the facilities and development in this field [26].

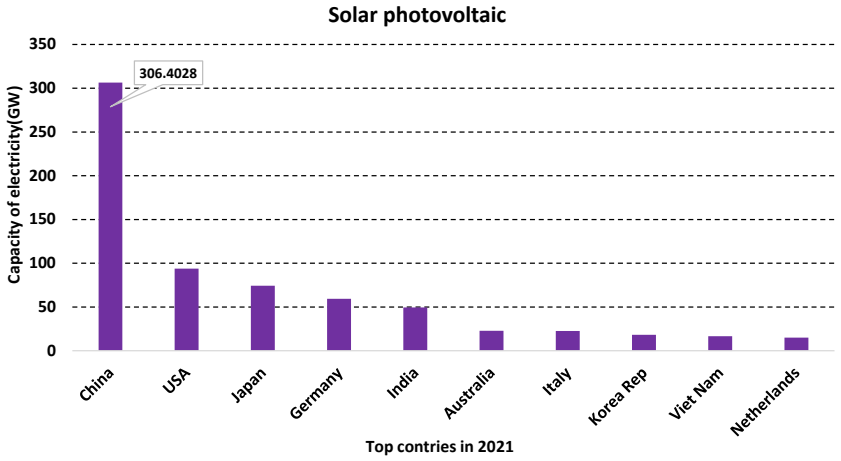


Figure I.12: Top 10 countries of installed capacity of electricity by PV

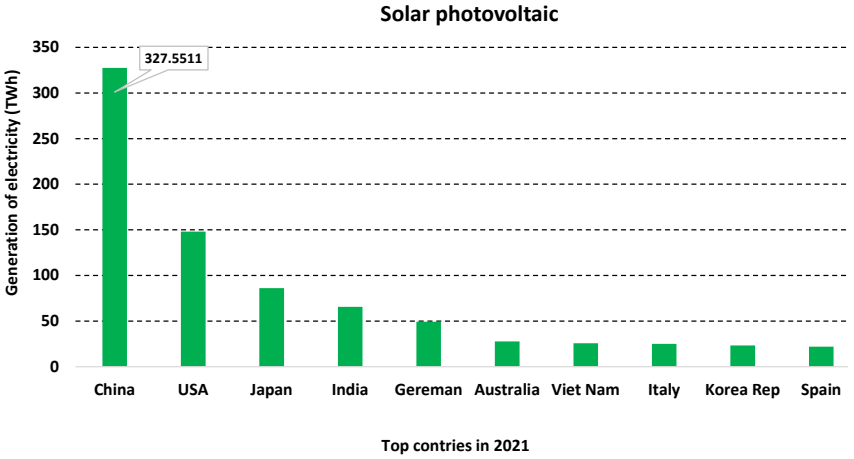


Figure I.13: Top 10 countries of electricity generation by PV

### I.2.6 Advantages and disadvantages of PV system

PV systems offer several advantages, but they also have several disadvantages. The table I.2 summarizes the main advantages and disadvantages.

| Advantages | Disadvantages |
|---|---|
| **Clean and sustainable energy production**: PV provides clean, sustainable energy by producing no greenhouse gases or air pollution, which helps reduce carbon emissions and combat climate change. | **Dependence on weather conditions**: PV is less efficient in cloudy weather and can be impacted by extreme temperatures, leading to lower energy production and higher maintenance costs. |
| **Versatility and scalability**: PV is versatile and scalable, allowing installation in various locations and adaptable to different energy needs, making them ideal for both grid-connected and off-grid applications. | **High initial cost of installation**: Despite recent cost reductions, installing PV remains costly, particularly for large-scale projects. |
| **Declining costs**: PV costs have dropped significantly in the past decade and are expected to keep decreasing, making them more affordable. | **Need for energy storage**: PV requires energy storage for times when sunlight is unavailable, adding to their cost and complexity. |
| **High energy conversion efficiency**: PV efficiently converts a significant portion of solar energy into electricity, making it highly effective. | **Ineffective in low light levels**: PV produces less energy in low-light conditions, such as cloudy days or at night. |
| **Reduced dependence on fossil fuels**: PV lessens global reliance on fossil fuels, enhancing energy security and conserving finite resources. | **Limited lifespan**: PV panels generally last 25 to 30 years before needing replacement, potentially increasing long-term costs. |
| **No noise pollution**: PV generates no noise pollution, making it ideal for residential and urban areas compared to fossil fuel-based energy sources. | **Dispose and recycle**: PV panels contain materials that can be harmful to the environment if not disposed of or recycled properly. |

Table I.2: Advantages and disadvantages of PV systems

### I.2.7 Types of PV installations

Figure I.14 exhibits various categories of solar PV installation, which can be described as follows:

1. **Ground-mounted solar PV:** This type of installation consists of solar panels that are mounted on the ground using a metal or wooden structure. They are often used in large-scale projects and are ideal for sites with much available land.

2. **Floating PV:** This type of installation involves floating solar panels on bodies of water, such as lakes or reservoirs. FPV systems can provide additional cooling for the panels and reduce the pressure on land use.

3. **Roof-mounted solar PV:** This type of installation consists of solar panels that are mounted on the roof of a building. This is the most common type of installation and is suitable for homes and businesses with suitable roof space.

4. **Building-integrated solar PV:** This type of installation involves integrating solar panels into the building design and structure, replacing traditional building materials such as roofing or walls.

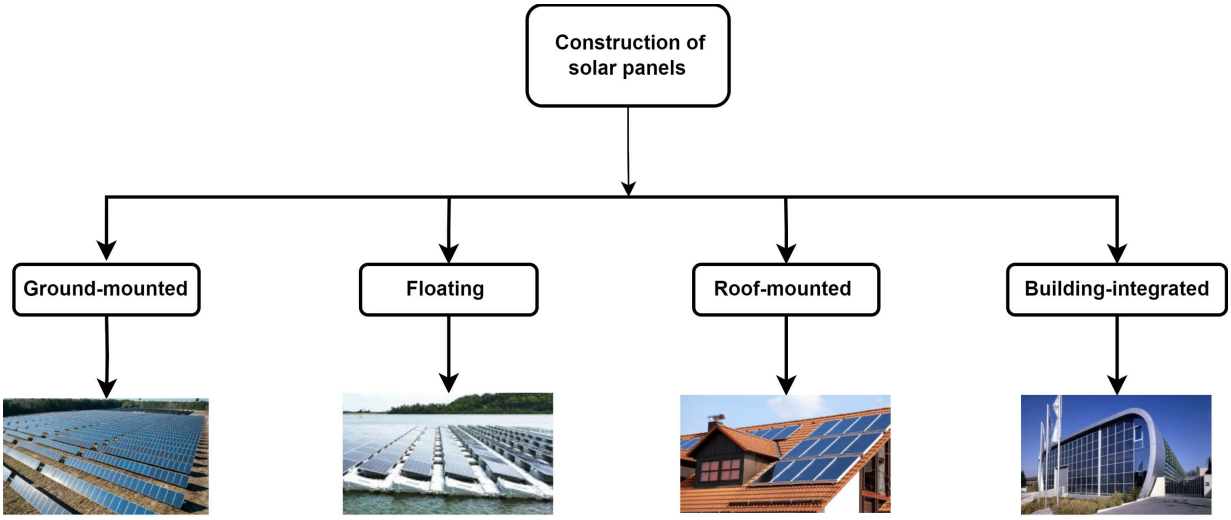


Figure I.14: Categories of solar panels installation

## I.3 Topologies for offshore wind farms

Turbine assembly and interconnection system design will become critical as wind farms are installed in far offshore locations. Proper selection of the assembly system topology is essential to maximize the captured energy and ensure a high-reliability design. Researchers have proposed different topologies, with the radial system being the most common. Therefore, appropriate topologies must be chosen in terms of losses, reliability, and costs. The following will describe some topologies for internal AC and DC grids.

### I.3.1 Topologies of offshore wind farms on AC grid

Three basic internal AC grid connections are utilized in offshore wind farms: Radial, radial loop, and cluster/Star topology.

#### I.3.1.1 AC Radial topology

Figure I.15 shows a radial configuration of a wind farm, where turbines in series that generate AC power are connected using common cables based on the current carrying capacity of the cable. These turbines are tied together at a substation mounted on an offshore platform in the case of offshore wind farms, where the collector system voltage is increased to transmit power to shore. This is the most common and cost-effective radial configuration, however, this method may face reliability issues. If the cable between the first turbine and the feeder is faulty, all the turbines connected after it will fail, resulting in the loss of the power generated [29].

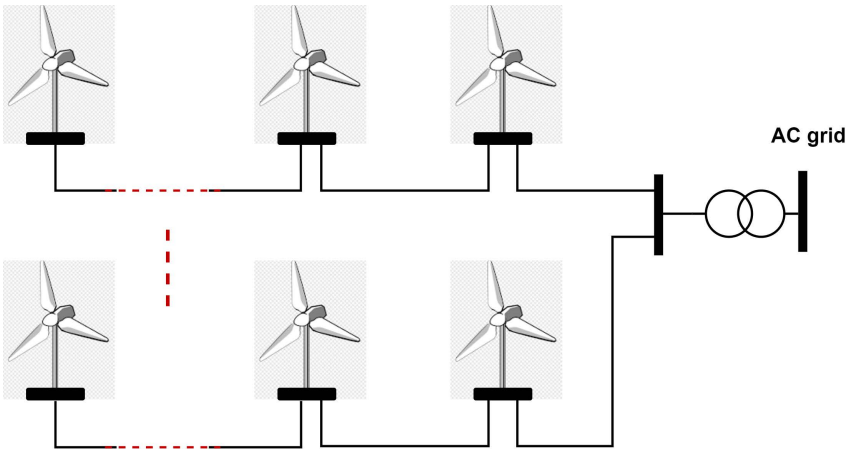


Figure I.15: AC radial topology

#### I.3.1.2 AC Radial loop topology

The Figure I.16 presents two types of radial loop topologies commonly used in offshore wind farms: the double-radial loop and the single-radial loop, as illustrated in Figure I.16 (a) and (b) respectively. In the single-radial loop topology, all wind turbines are connected via a single cable that runs through the entire array to the substation, forming a partial loop where energy flows in one direction.

While this setup is cost-effective and straightforward, it lacks redundancy; any fault in

the cable can disrupt the connection for all turbines downstream. On the other hand, the double-radial loop topology involves two parallel cables connecting each turbine, forming a complete loop and ensuring redundancy.

In this configuration, power can still be transmitted via the second cable in the event of a failure, providing greater reliability. However, this increased redundancy comes with higher costs and complexity due to the additional infrastructure required [29, 30].

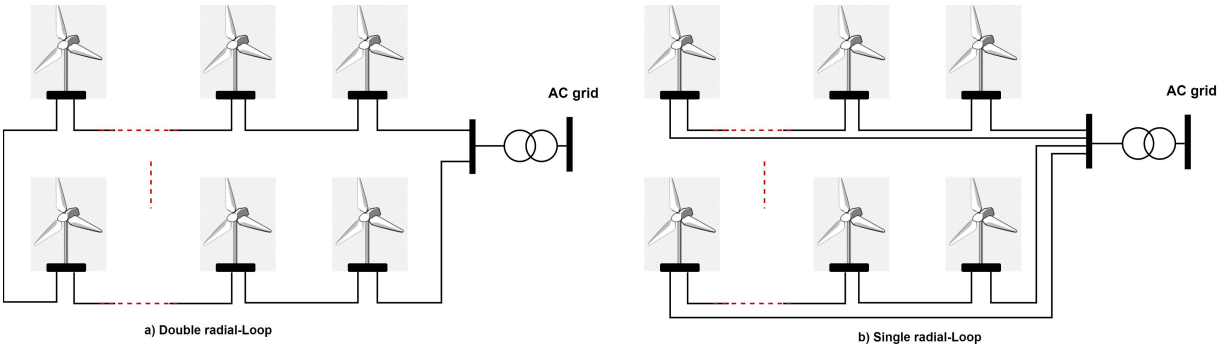


Figure I.16: AC radial-loop topology

#### I.3.1.3 AC Cluster/Star topology

In this topology as in the Figure I.17, each wind turbine is to a central collection point through separate cables (star/cluster), which in turn is connected to the power grid via an underwater link.

This configuration offers several benefits including straightforward maintenance, as issues with one turbine or cable do not impact the others, allowing for efficient repairs. It also provides flexibility for expanding the farm by adding more turbines without significant changes to the existing setup, and reduces the amount of underwater cabling compared to other topologies. However, the system can be costly due to the high expenses associated with the central collection station and the potential for increased costs and transmission losses due to the lengthy individual cables. Additionally, the complexity of managing protection systems for each connection poses a challenge [29].

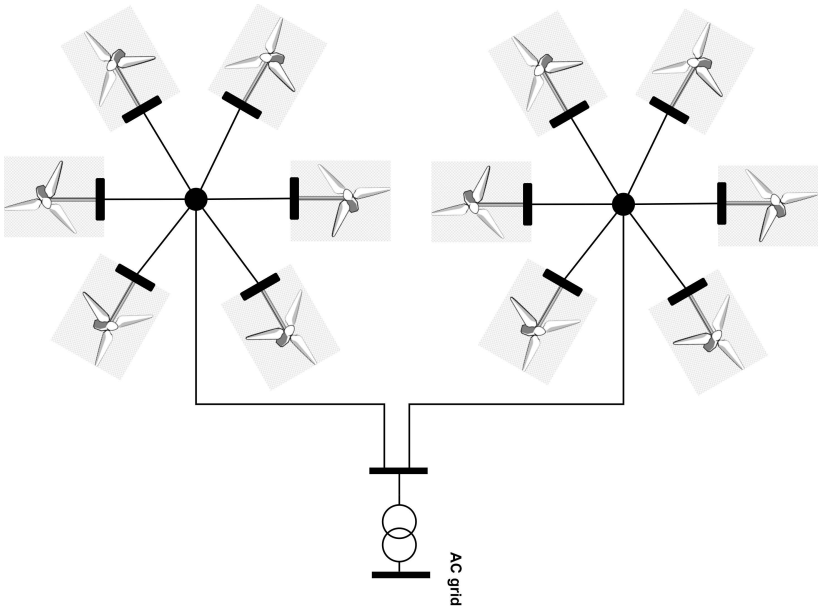


Figure I.17: AC cluster/star topology

### I.3.2 Topologies of offshore wind farms on DC grid

Systems integrating HVDC connections to the grid generate AC power and employ converter stations for converting AC/DC/AC for grid compatibility. However, experience with offshore converter stations remains limited. Consequently, some researchers advocate for medium-voltage DC collection systems paired with HVDC for grid interconnection. This approach aims to enhance efficiency and reduce the need for large offshore converter stations.

A proposed design involves a series-parallel configuration of turbines with DC collection, which does not require a converter station to elevate the voltage to transmission levels. Researchers have explored both series and series-parallel configurations for DC wind farms, where turbines are connected in a series similar to batteries, thus increasing the voltage to transmission levels [31,32]. three basic internal DC grid connections are utilized in offshore wind farms: DC radial, DC Series, and DC Series-Parallel topology.

#### I.3.2.1 DC radial

Figure I.18 illustrates a DC radial topology of a parallel-connected wind farm, where the turbines generate DC power output. The turbines produce medium-voltage DC (MVDC),

which is transmitted as HVDC. Alternative DC radial systems have been proposed in which power is initially collected as AC from the turbines and then transmitted as HVDC. Offshore platforms with converter stations are used to step up the MVDC to the required transmission voltage. In the system shown in Figure I.18, HVDC transmission is employed, with an onshore converter station facilitating interconnection with the AC grid onshore [33].

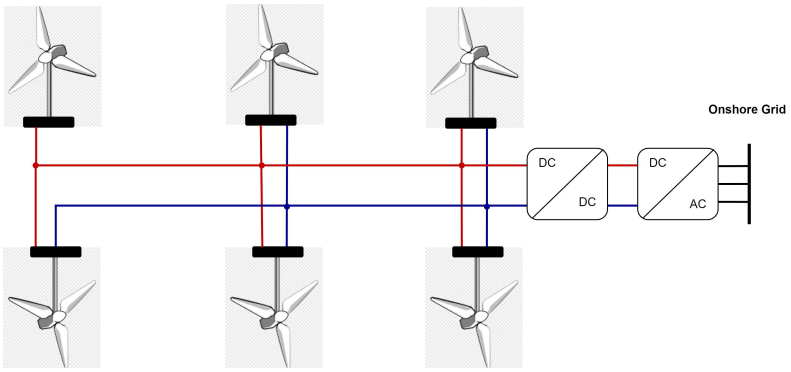


Figure I.18: DC radial topology

### I.3.2.2 DC series

The DC series topology in wind turbines involves connecting turbines in a sequence, as shown in Figure I.19. This setup allows the DC output from each turbine to accumulate, raising the overall voltage as power passes through each turbine. This method eliminates the necessity for large offshore converter stations, as the voltage is directly increased through the series connection to reach transmission levels, thereby reducing power losses over extended distances.

The primary benefits of this configuration include improved transmission efficiency due to higher voltage and lower current, as well as a simpler infrastructure that avoids the complexities of large converter stations. However, a potential issue is that a failure in one turbine could affect the entire series, impacting the performance of the wind farm. This approach is gaining attention for its use in MVDC and HVDC collection and transmission in offshore wind farms [31].

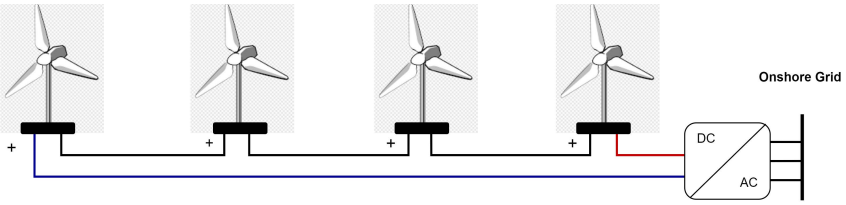


Figure I.19: DC series topology

#### I.3.2.3 DC series-parallel

The DC series-parallel topology combines both series and parallel connections to enhance power transmission, as presented in Figure I.20. In this design, turbines are first arranged in series to increase voltage levels, and then these series groups are connected in parallel to maintain appropriate current and introduce redundancy.

This configuration effectively raises transmission voltage while offering better reliability than a purely series system. Key benefits include improved transmission efficiency due to increased voltage, enhanced system reliability through redundancy, and minimized power losses. This makes it an ideal solution for offshore wind farms, where both efficient long-distance power transmission and reliability are critical [32].

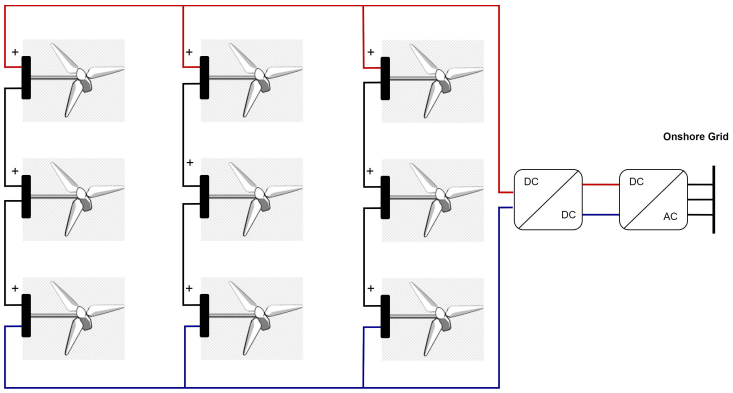


Figure I.20: DC series-parallel topology

## I.4 Topologies of PV system connected grid

In grid-connected PV systems, the design and operation of the inverter focus on improving efficiency and production across different power levels. The main factors include maximum power point tracking (MPPT), ensuring high efficiency, regulating power injection into the grid, and reducing harmonic distortion in the charged current.

The performance of the inverter is closely related to the applied control strategy. This section presents a review and comparison of the main power inverter topologies as shown in Table I.3, identifying four basic configurations for grid-connected PV setups without battery storage [34].

### I.4.1 Topologies centralized inverter

In the centralized inverter configuration for the PV system, numerous PV modules are arranged either in series, in parallel, or both to create a large array as presented in the Figure I.21. This array is connected to a single, central inverter that transforms the direct current (DC) produced by the modules into alternating current (AC) for grid supply.

The primary benefits of this setup include its straightforward design, cost-efficiency for large-scale operations, and relatively simple maintenance. However, it faces challenges such as reduced efficiency due to module mismatch losses, reliance on a single inverter (a potential failure point), and the need for long DC cables. This topology is most commonly utilized in large utility-scale solar farms [35].

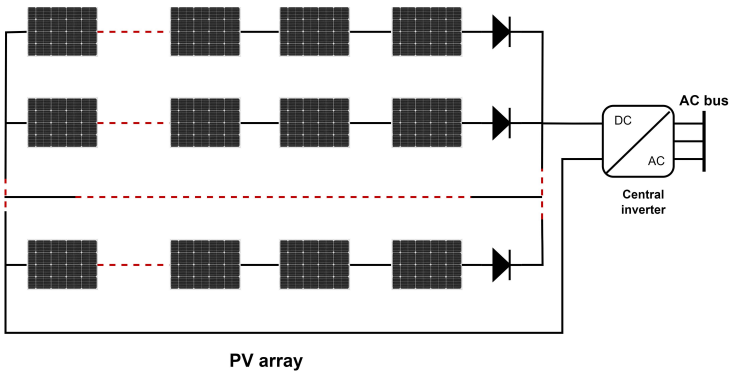


Figure I.21: Diagram of centralized inverter

### I.4.2 Topologies string inverter

In the string inverter topology, several strings of PV modules are connected to their dedicated inverters, with each string typically composed of 8 to 20 modules connected in series as shown in the Figure I.22, and the power range is around 5 kW. This configuration offers improved efficiency over centralized systems by minimizing mismatch losses.
Its modular nature also makes it easier to expand and provides greater flexibility in handling

shading issues. However, the wiring is more complex, and it tends to be costlier for large-scale applications compared to centralized inverters. This topology is commonly used in residential, commercial, and industrial solar installations [36].

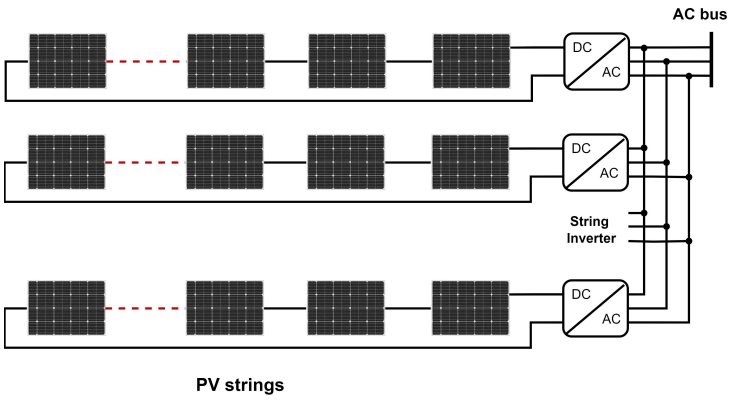


Figure I.22: Diagram of string inverter

### I.4.3 Topologies multi-string

As shown in Figure I.23, this topology is similar to the string inverter topology, but with the distinction that multiple strings of PV modules are linked to a single inverter that features several MPPT inputs. This allows each string to function independently, enhancing power conversion efficiency. This configuration improves overall performance, reduces mismatch losses, and accommodates varying module orientations and technologies more effectively than single-string systems. However, it is more costly and complex to design and install [37]. It is typically used in medium to large commercial solar installations.

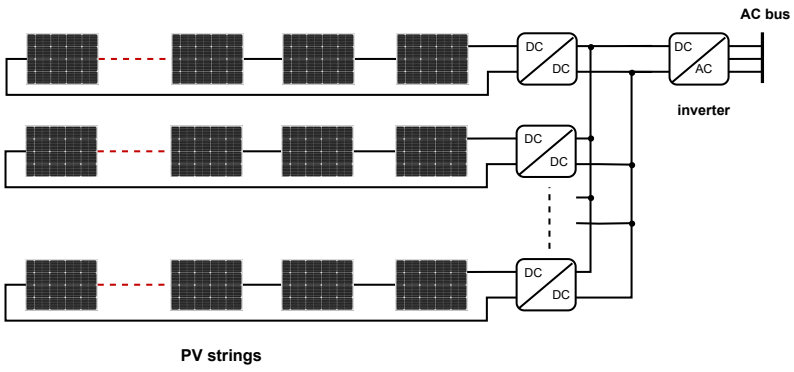


Figure I.23: Diagram of Multi-String

### I.4.4 Topologies Microinverter

In the microinverter topology, as shown in Figure I.24, each PV module is equipped with its microinverter that directly converts the DC power from the panel into AC. This design allows for individual MPPT for each module, which enhances energy production and removes the issue of mismatch losses between modules. It also simplifies installation and expansion while offering better performance in scenarios where shading is a concern.

However, the initial setup is more expensive and involves more components, and the increased number of inverters can raise the likelihood of system failures [38]. This configuration is often used in residential systems, small commercial setups, and rooftops with shading challenges.

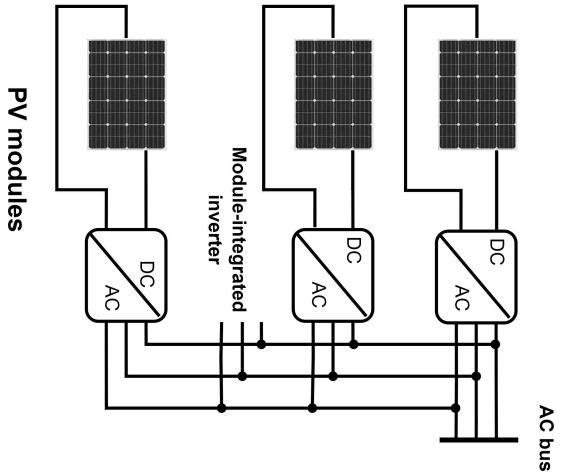


Figure I.24: Diagram of Microinverter

| Topology | Efficiency | Cost | Complexity | Applications |
|---|---|---|---|---|
| **Centralized Inverter** | Medium | Low | Simple | Utility PV farms |
| **String Inverter** | High | Medium | Moderate | Residential, commercial |
| **Multi-String Inverter** | High | Medium-High | Moderate | Medium to large commercial |
| **Microinverter** | High | High | Complex | Residential, small commercial |

Table I.3: Comparison of PV system topologies

## I.5 The HVDC system

High-voltage direct current (HVDC) transmission relies on two primary technologies, as shown in the Figure I.25: (A) HVDC based on Voltage Source Converter (VSC) and (B) HVDC based on Current Source Converter uses thyristors. HVDC-VSC uses transistors such as IGBT, which allows it to independently control both active and reactive power. This adaptability makes it ideal for integrating renewable energy sources and supporting weak grids, especially in urban or offshore environments [39].

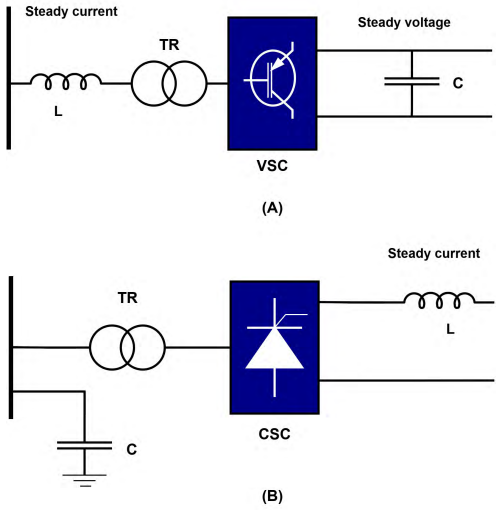


Figure I.25: (A)-Self Commutated Voltage Source Converter(VSC), (B)-Line Commutated Current Source Converter (CSC)

In contrast, CSC-HVDC, which relies on thyristor-based line-commutated converters (LCC), is particularly suited for long-distance, high-capacity power transmission due to its generally lower losses and higher efficiency over extensive distances. However, CSC-HVDC requires a strong AC grid for commutation and lacks the capability to support reactive power. Recent studies have aimed to enhance VSC-HVDC's efficiency and scalability, often by incorporating modular multi-level converters (MMCs) to boost fault tolerance and reduce power losses [40].

For CSC-HVDC, researchers are exploring hybrid systems that combine features from both converter types, increasing CSC's adaptability and resilience in changing grid conditions. These innovations are essential as HVDC technology continues to play a key role in

updating power grids and advancing the global transition to renewable energy sources [41].

Figure I.26 shows the proposed system for offshore wind farms and PV plants connected to the HVDC system from a controlled rectifier (VSC) and an inverter (VSC); the next chapter will describe the system components in detail.

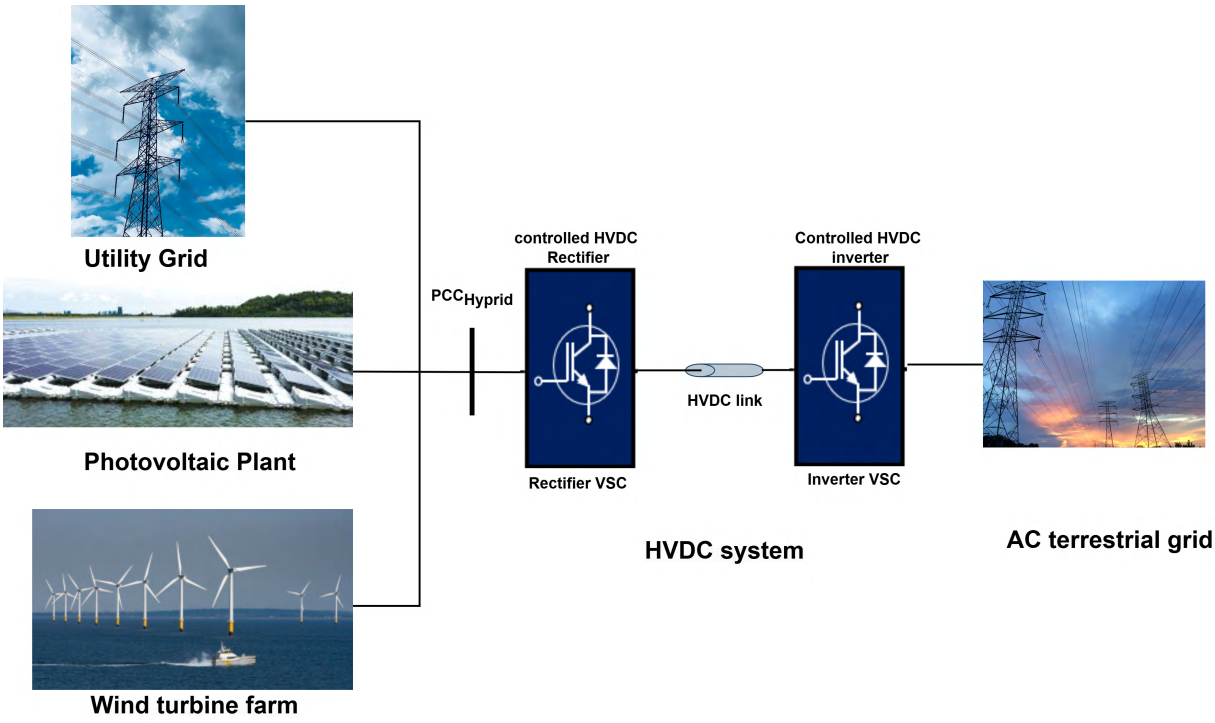


Figure I.26: Scheme of the proposed system

### I.5.1 The HVDC-VSC transmission system

The HVDC-VSC transmission system was introduced to address the challenge of transmitting electricity over long distances, especially from offshore wind farms. This system converts AC generated by wind or solar power into DC, allowing efficient transmission through underwater cables to the grid. The system enhances transmission efficiency and enables voltage and frequency control, ensuring stable power delivery. Notably, HVDC-VSC technology supports two-way power flow, allowing energy transfer in both directions. Furthermore, these systems improve grid reliability by incorporating advanced power management, like active and reactive power control [42, 43].

### I.5.2 A brief history of HVDC systems

Thomas Edison built the 1st electrical power system located in New York's Pearl Street station. This system, which started operating in 1882, was a DC system that served 59 consumers within a radius of approximately 1.5 km. The generator, cables, and loads were all part of this system. HVDC technology was first commercialized in 1954 with the installation of a power transmission link connecting Gotland to mainland Sweden. This link used a 96 km submarine cable to transmit 20 MW of electricity at a nominal voltage of 100 kV. Today, there are more than 50 operational HVDC systems globally, with numerous additional projects under development [44].

In the 1960s, numerous HVDC connections were developed, sparking significant international attention. Notable projects included the Konti-Skan link between Denmark and Sweden, Japan's Sakuma link with 50/60 Hz frequency converters, the connection between New Zealand's North and South Islands, the Italy-Sardinia link, and the link to Vancouver Island in Canada [45].

In 1965, General Electric's laboratories produced the thyristor, a semiconductor device capable of performing the function of static switching with controlled closing. In 1970, the first thyristor valve was tested on the Gotland link, and in 1972, the inaugural back-to-back converter station was established by General Electric in Eel River, Canada [45].

The largest HVDC transmission project is the Itaipu link in Brazil, which was launched in 1979 with a transmission capacity of 6300 MW. This connection was completed and commissioned in several stages between 1984 and 1987, this link is crucial to Brazil's electric power supply [46].

The significant reduction in the cost of converters, facilitated by the new thyristor technology, has greatly contributed to the growth of DC connections. After Itaipu, the most ambitious project was the Quebec-New England interconnection, which was the inaugural significant multi-terminal HVDC link, with a transmission capacity of 2000 MW at ±450 kV, was established in 1992, In Sweden in 1999, the HVDC Light, an IGBT-based voltage source HVDC system, commenced electricity transmission between Grangesberg and

Hellsjon. [47].

### I.5.3 Description of the HVDC-VSC system

The HVDC-VSC system is a form of DC transmission that utilizes modern power electronics technology, specifically IGBT, to facilitate the conversion between AC and DC. Unlike conventional HVDC systems, which rely on LCC with thyristors, the HVDC system uses VSCs, providing greater flexibility and improved transmission efficiency. As shown in the Figure I.27, the HVDC-VSC system is composed of several essential components, including:

- **Transformer**: Steps up or steps down the voltage from the AC system.
- **AC Filter**: Removes unwanted harmonics from the AC power to ensure smooth operation of the system.
- **Phase Reactor**: Controls the flow of current and helps in managing the voltage and reactive power.
- **Station VSC 1 (AC/DC Rectifier)**: Converts the AC power from the first system into DC for transmission.
- **DC Line (cable)**: The transmission line through which the DC power is transmitted between the two converter stations.
- **Station VSC 2 (DC/AC Inverter)**: Converts the transmitted DC power back into AC power to be fed into the second AC system.

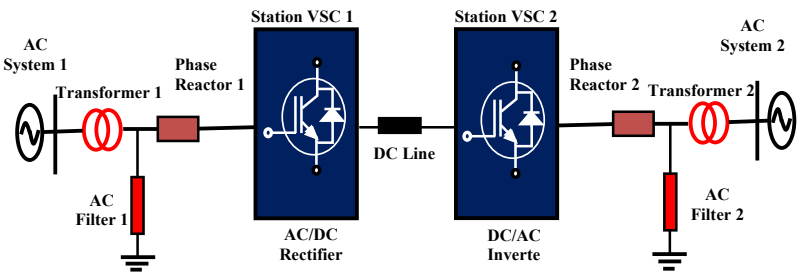


Figure I.27: Diagram of HVDC-VSC system

### I.5.4 Advantages of the HVDC-VSC transmission

The following are the principal advantages of HVDC-VSC technology:

- **Autonomous energy regulation**: HVDC-VSC allows for separate control of active and reactive power, improving system stability and reducing the need for extra equipment.
- **Rapid response**: With high-frequency switching and PWM, VSC systems quickly adjust to maintain power quality and stability.
- **Improved grid connectivity**: VSC systems can connect different grids and integrate renewable energy sources.
- **Black start capability**: VSC systems can restart the grid after a blackout without external power, enhancing system resilience.
- **Complex DC grid**: VSC supports multi-terminal DC grids, allowing for sophisticated interconnections and integration of various renewable sources.
- **Power quality enhancement**: VSC systems help regulate voltage and address issues like flicker and voltage sags, improving overall power quality.

### I.5.5 HVAC Transmission System

The HVAC system is widely used in the transmission of global power systems. It consists of two main components: converters and transmission lines. HVAC systems have a lower cost advantage than HVDC-VSC systems. HVAC systems have fewer components and are easier to install and maintain than HVDC-VSC systems. The HVAC system also has a high degree of reliability because it has been extensively used and tested for many years. Despite the advantages of the system, it also has many disadvantages, such as:

1. **Transmission inefficiencies and voltage Instabilities**: Long-distance power transmission can result in inefficiencies, increased costs, and issues with voltage regulation, affecting connected equipment.

2. **Signal disruption**: Electromagnetic interference can disrupt signals, potentially leading to system malfunctions.

3. **Power quality and safety concerns**: Harmonic distortions and poor grounding can impair power quality and present safety hazards, causing potential damage to equipment.

4. **System overload and insulation failures**: Overloading the system can lead to failures, while aging or environmental factors can cause insulation to degrade, resulting in safety risks and reduced performance.

5. **Instability problems**: Frequency and transient instability can cause synchronization issues, power interruptions, and fluctuations that may damage equipment.

All these disadvantages make the HVDC-VSC system a suitable and promising option, especially in terms of efficiency and long distances, despite the high initial cost.

### I.5.6 Comparison of classic HVDC and HVDC-VSC

In HVDC-VSC system, it functions as a voltage source while synchronizing with the frequency of the connected AC system. It can autonomously control reactive and active power, offering a distinct advantage over a traditional HVDC system, which uses reactive power and requires an external voltage source for switching.

In the power reversal case, a traditional HVDC modifies the polarity of direct voltage while a VSC switches the direction of the current, making the conventional HVDC system unsuitable in MTDC configurations, as a change in polarity from one converter would reverse the polarity of all converters connected to the same DC grid, thus obstructing the required power flow. VSC, however, ensures that the power flow can be reversed at a single converter without affecting the DC voltage of the entire system. Additionally, power flow inversion for a conventional HVDC system can be time-consuming, whereas, with a VSC, it can be achieved instantaneously [48, 49].

In addition, the conventional HVDC system requires a robust AC network connection due to potential voltage or frequency fluctuations that could result in switching errors and

disrupt power transmission. Conversely, in a VSC setup, power flow is only impacted by voltage drops, which are dependent on the level of reduction in the AC voltage. However, a major challenge associated with utilizing HVDC-VSC is the higher switching losses, the table I.4 presents a comparison between classic HVDC and HVDC-VSC [48, 50].

| Category | Classic HVDC | VSC-HVDC |
|---|---|---|
| **Converter Technology** | Uses thyristor-based, LCCs with limited adaptability to dynamic grid conditions. | Employs IGBT-based converters with PWM, enabling fast, flexible, and independent control of active and reactive power. |
| **Control and Flexibility** | Limited controllability and reactive power support; less effective in modern grids. | Highly controllable with robust reactive power support, ideal for renewable-rich and weak grids. |
| **Transmission Distance and Capacity** | Best suited for long-distance, high-capacity power transfers. | Effective for medium to long distances and variable power sources such as offshore renewables. |
| **Installation and Infrastructure** | Requires large converter stations and extensive infrastructure; unsuitable for urban deployment. | Compact converter design allows easier integration into existing or space-limited systems. |
| **Economic Considerations** | Cost-effective for large-scale, long-distance projects. | Increasingly viable for smaller-scale or modular applications due to technological advances. |

Table I.4: Comparison between classic HVDC and VSC-HVDC

### I.5.7 Topologies of HVDC transmission system

A variety of configurations exist in HVDC systems as shown in Figure I.28, each with distinct characteristics. The monopolar HVDC system (a) uses a single conductor, typically with a ground or sea return. This setup is cost-efficient for certain installations, like submarine cables, but has the downside of higher losses when relying on ground return.

In contrast, the bipolar HVDC system (b) consists of two conductors with opposite polarities. This design offers increased reliability as if one line fails, the system can continue to function at reduced capacity using the remaining pole and ground return. However, it requires more infrastructure, raising installation costs.

The back-to-back HVDC system (c), designed for connecting two asynchronous AC networks, converts AC to DC and back again without needing long-distance transmission. It is ideal for connecting grids with differing frequencies, though it is unsuitable for long-distance transmission. A more complex option, the multi-terminal HVDC system (d), features multiple converter stations connected to a single HVDC line [51]. This configuration allows for power injections and withdrawals at several points, providing flexibility but complicating control and protection schemes.

Lastly, the tripolar HVDC system (f) employs three conductors, including a neutral return conductor, allowing for continued operation if one pole fails. While this enhances fault tolerance, it adds complexity and cost compared to more conventional systems. Each of these configurations serves specific needs depending on the operational requirements, geographical constraints, and economic considerations [52]. The table I.5 summarizes these configurations.

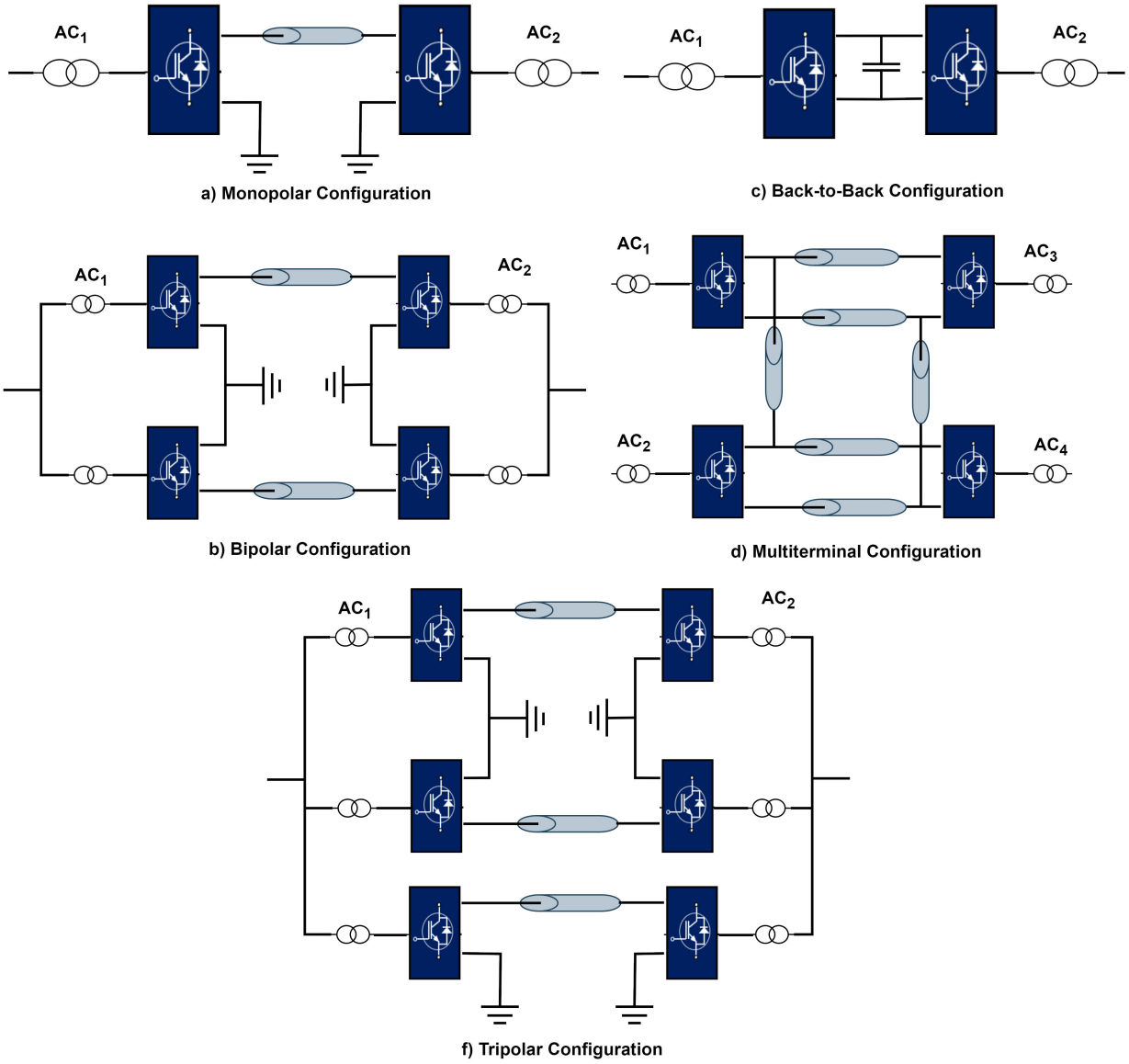


Figure I.28: Topologies of HVDC transmission system

| Configuration | Description | Advantages | Disadvantages |
|---|---|---|---|
| Monopolar | Uses a single conductor for power transmission, with a return path through the ground or a metallic conductor. | Simplest and most economical for long-distance transmission. | Lacks redundancy; if the conductor fails, the system goes offline. |
| Bipolar | Consists of two conductors, one positive and one negative, allowing for greater power transfer capacity. | If one conductor fails, the system can still operate at reduced capacity using the remaining conductor with ground return. | More complex than monopolar; higher cost. |
| Back-to-Back | Both the rectifier and inverter are located at the same station, connecting two asynchronous AC systems without a DC transmission line. | Useful for interconnecting systems with different frequencies. | Limited to specific applications; no long-distance transmission. |
| Multi-terminal DC (MTDC) | Connects multiple converter stations, allowing for complex power distribution and flexible power transfer. | High flexibility and allows for more complex power distribution. | More complex control and design. |
| Tripolar | Utilizes three conductors, enhancing reliability and capacity while reducing space needed for converter stations. | Increased reliability and capacity, particularly effective in space-constrained areas like urban environments. | Newer design; potentially higher cost and complexity. |

Table I.5: HVDC Transmission System Configurations

### I.5.8 Projets of technologies HVDC-VSC

HVDC-VSC technology has become a preferred solution for developers and grid operators, supporting large-scale renewable integration, underground and submarine links, and interconnections between grids. With projects reaching capacities of up to 3,000 MW, it

plays a vital role in advancing reliable long-distance power transmission. The table I.6 presents some of the most important projects [53, 54].

| Project | Capacity (MW) | Length (km) | Countries/Region | Year | Details |
|---|---|---|---|---|---|
| North Sea Link (NSL) | 1,400 | 720 | Norway, UK | 2021 | The longest subsea link. |
| DolWin3 | 900 | 160 | Germany (North Sea) | 2017 | Linking offshore wind farms to the grid. |
| INELFE Interconnector | 2,000 | 64 | France, Spain | 2015 | Underground HVDC link. |
| Zhongtianshi ±500 kV | 3,000 | 531 | China | 2020 | China's first large-scale HVDC-VSC project. |
| Skagerrak 4 | 700 | 240 | Norway, Denmark | 2014 | Enhances power exchange between hydro and wind/thermal grids. |
| NordBalt | 700 | 450 | Sweden, Lithuania | 2016 | Integrates the Baltic region with the Nordic power market. |
| Caithness-Moray | 1,200 | 160 | Scotland (UK) | 2018 | Connects renewable energy from northern Scotland to UK grid. |
| BorWin3 | 900 | 160 | Germany (North Sea) | 2019 | Transmits offshore wind power to the German grid. |
| Murraylink | 220 | 180 | Australia | 2002 | Connects South Australia and Victoria via HVDC-VSC. |
| Shanwei | 2,000 | 285 | China | 2020 | Supports renewable integration and inter-regional transmission. |

Table I.6: Top 10 Largest HVDC-VSC Projects

## I.6 Conclusion

The global community is confronted with significant obstacles in the provision of energy for its expanding population. To address these challenges, the employment of HVDC technology becomes imperative due to its advanced stage of development and rapid evolution within the energy sector. The supply of energy must occur in an environmentally benign manner.

Numerous solutions have been devised to safeguard the environment while simultaneously fulfilling the escalating energy demand. Illustrative instances encompass offshore wind energy and solar power harnessed in desolate regions, both of which are regarded as clean and adaptable energy sources. Nonetheless, these energy sources are frequently located in isolated areas, far removed from urban centers, necessitating the transmission of substantial electrical power across extensive distances.

To tackle this quandary, the utilization of HVDC technology emerges as one of the potential remedies to facilitate the delivery of energy from these distant regions. Consequently, HVDC technology is expected to be essential in make a more sustainable world in the coming years . Furthermore, it becomes evident that HVDC-VSC technology embodies a resilient and cost-efficient alternative for the upcoming expansion of the transmission grid. HVDC-VSC is the favored option for transmitting power from offshore wind farms and PV plants to AC grids and can strengthen the AC grid.

This chapter provided an overview of renewable energies and presents a historical summary and statistics of wind and PV power systems. We have conducted several bibliographic searches for different topologies to interconnect offshore wind farms and PV plants in AC and DC. Finally, we presented the transmission system using HVDC-VSC converters based on IGBTs.

In the next chapter, we present a PV and wind energy conversion model with a PMSG generator, in addition, modeling an HVDC-VSC link and all its components.

# Chapter II

# Modeling of systems: Photovoltaic, wind energy conversion, HVDC-VSC

## II.1 Introduction

The rapid development of the energy sector over the past decades has imposed the need to fundamentally rethink how energy systems are designed, managed, and operated. Challenges related to environmental issues, security of energy supply, and increasing demand for electricity have led to a growing interest in renewable energy sources and advanced transportation technologies.

The importance of PV and wind power generation technologies has increased significantly in recent years. Photovoltaics, which results from converting sunlight into electricity, is a clean and abundant source of energy. For their part, wind farms take advantage of the power of the wind to generate electricity.

The HVDC-VSC transmission system, an advanced technology, plays a crucial role in enabling the efficient transportation of electricity over long distances. Unlike the traditional HVAC transmission system. HVDC-VSC offers significant advantages in reducing power loss, grid stability, and power control. However, modeling this energy and integrating it into existing electricity networks presents complex challenges due to the need to ensure coordination with intermittent renewable energy sources.

This chapter aims to model and analyze three main components of a power system based on PVs, a wind turbine, and an HVDC-VSC transmission system.

## II.2 Description of the general system

The Figure II.1 illustrates the general configuration of the proposed system, comprising four main components: a hybrid renewable energy system (HRES) connected to an utility grid. This hybrid system includes two PV station, each with a rated power output of 100 kW, and a 100 kW wind farm. These are connected at the hybrid point of common coupling $PCC_{Hybrid}$ to an HVDC-VSC, which is ultimately connected to the terrestrial AC grid. The details of the main component and its modeling will be described in this chapter.

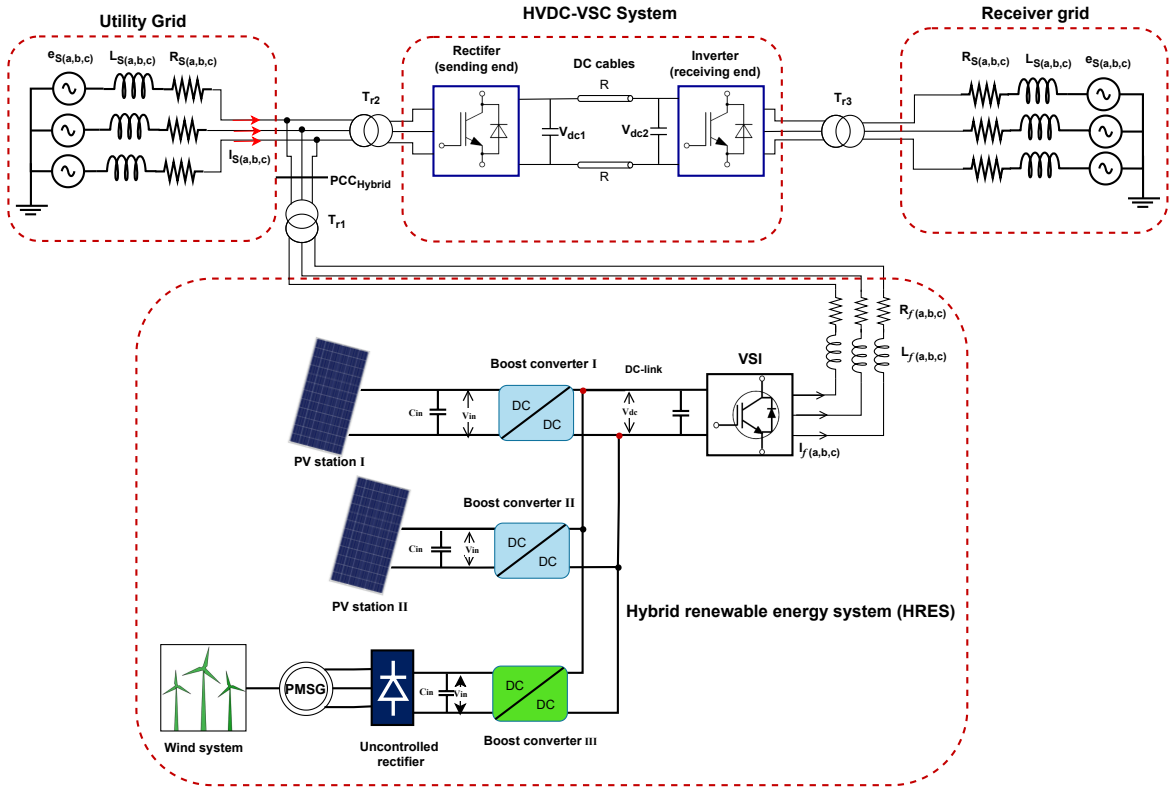


Figure II.1: The general configuration of the proposed system

### II.2.1 Modeling a PV generator

The PV cells are designed as semiconductors, with a series arrangement of cells in parallel to achieve the desired output power. A mathematical representation of the PV cell can be found in the equivalent circuit model with a single diode. This model includes a light-generating current source, a p-n junction for the single cell represented by a solitary

diode, (Rs) series resistance, and (Rsh) shunt resistance. The shunt resistance describes the internal resistance of the cell for current flow [55], as illustrated in Figure II.2.

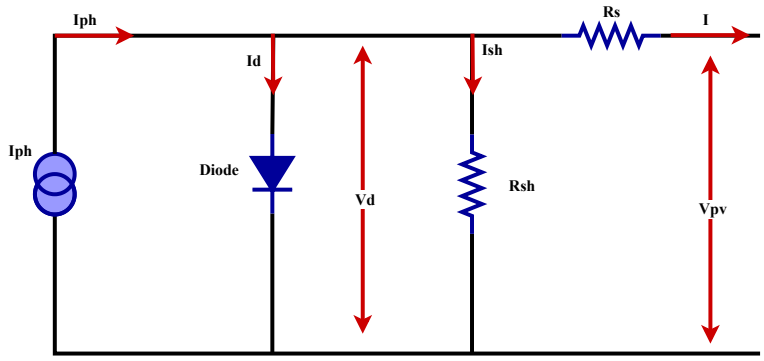


Figure II.2: Equivalent electrical diagram of a PV cell

The current generated by the cell is given by the following equation:

$$I_{pv} = I_{ph} - I_d - I_{sh} \tag{II.1}$$

The current passing through the shunt resistor $I_{sh}$ is given by the expression:

$$I_{sh} = \frac{V_{pv} + R_s I}{R_{sh}} \tag{II.2}$$

The Current of Shockley diode is given by the expression:

$$I_d = I_0 \left[ \exp \left[ \frac{q\,(V_{pv} + R_s I)}{AkT} \right] - 1 \right] \tag{II.3}$$

Where

$I_0$: diode saturation current (A).

$I_{ph}$: The photocurrent generated by the incident light.

$R_s$: The series resistance ($\Omega$).

$R_{sh}$:The shunt resistance ($\Omega$).

$T$: Cell temperature (Kelvin).

$q$: The charge of an electron ( $1.6 \times 10^{-19}$C).

$V_{pv}$: voltage across the cell.

$A$: ideality factor of the diode.

$k$: Boltzmann constant ($1.38 \times 10^{-23}$J/K).

By replacing Eq (II.2) and Eq (II.3) in Eq (II.1) we will have:

$$I_{pv} = I_{ph} - I_0 \left[\exp\left[\frac{q\left(V_{pv} + R_s I\right)}{AkT}\right] - 1\right] - \left[\frac{V_{pv} + R_s I}{R_{sh}}\right] \tag{II.4}$$

The expression for the current $I_{ph}$ generated from light is as follows:

$$I_{ph} = \frac{G}{G_n}\left[I_{sc,n} + k_i(T - T_n)\right] \tag{II.5}$$

And the saturation current $I_0$ can be expressed by the following formula:

$$\mathrm{I}_0 = I_{sc,n} \cdot \exp\left(\frac{qV_{oc,n}}{AkT}\right) \tag{II.6}$$

with $G$ and $G_n$ are the actual and nominal irradiance (STC conditions) $[W/m^2]$, respectively, $Isc_n$,$Voc_n$ are nominal short-circuit current and nominal open-circuit voltage, respectively,$k_i$ is coefficient of temperature effect on $Isc_n$.$T$, $T_n$ are the actual and nominal temperatures (STC conditions) [ Kelvin], respectively.

A PV panel is created by connecting multiple PV cells in series and parallel configurations. Through Eq (II.7), the output current ($I_{\text{panel}}$) and output voltage ($V_{\text{panel}}$) produced by the PV panel can be calculated as follows [56]:

$$\begin{cases} I_{\text{panel}} = N_p \cdot I_{\text{pv}} \\ V_{\text{panel}} = N_s \cdot V_{\text{pv}} \end{cases} \tag{II.7}$$

With $N_s$, $N_p$ is the number of series and parallel cells.

Therefore, by substituting Eq (II.7) into Eq (II.4), we can find the mathematical equation that describes the current generated by the PV panel [56]:

$$I_{pv} = N_p \times I_{ph} - N_p \times I_0 \left[\exp\left\{\left(\frac{q\left(\frac{V_{pv}}{N_s} + \frac{R_s}{N_p} I\right)}{nkT}\right)\right\} - 1\right] - \frac{\left(\frac{N_p}{N_s} V_{pv} + R_s I\right)}{R_{sh}} \tag{II.8}$$

The following equation gives the power of the Ppv generator:

$$P_{pv} = V_{pv}.I \tag{II.9}$$

Parameter values can be determined from the experimental data provided by the manufacturer in the PV panel technical data sheet. The table II.1 provides the panel characteristics.

| Parameters | Values (STC) | Parameters | Values (STC) |
|---|---|---|---|
| Power (W) | 414.801 | Tc of Isc (%/°C) | 0.0307 |
| Voc (V) | 85.3 | Iph (A) | 6.098 |
| Isc (A) | 6.09 | I0 (A) | 7.17e-13 |
| Vmp (V) | 72.9 | Diode Ideality Factor | 0.872 |
| Imp (A) | 5.69 | Rsh (Ω) | 419.78 |
| Tc of Voc (%/°C) | -0.229 | Rs (Ω) | 0.5371 |

Table II.1: Characteristics of the PV Module SPR-415E-WHT-D (Ns=7, Np=88)

### II.2.2 Characteristics of PV

The PV generator consists of interconnected cells to generate sufficient power. The generator's properties are determined by the current and voltage of the cells. Various models of PV devices exhibit different I-V and P-V characteristics. Three key points on the characteristic curve of a device are crucial: short-circuit, open-circuit, and maximum power points. These points are illustrated in Figure II.3 [57].

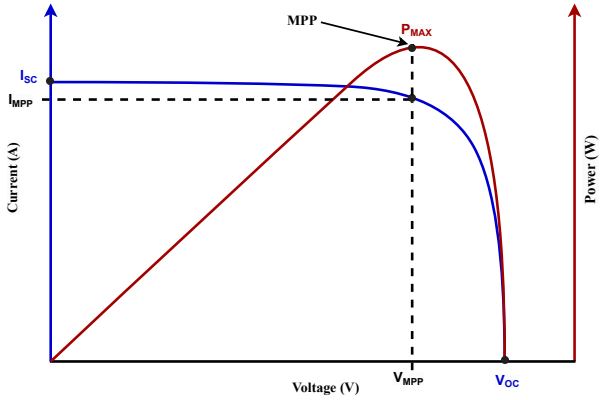


Figure II.3: Characteristic of a PV cell V-I and P-V

### II.2.2.1 Effect of radiation

Figure II.4 shows P-V curves that illustrate how the power output varies with voltage under different irradiation conditions from $100W/m^2$ to $1000W/m^2$. Higher irradiance generates a higher short-circuit current (Isc) and thus increases the power output of the PV cell while the open-circuit voltage (Voc) has similar values. Partial shading on the PV cell significantly affects the output power.

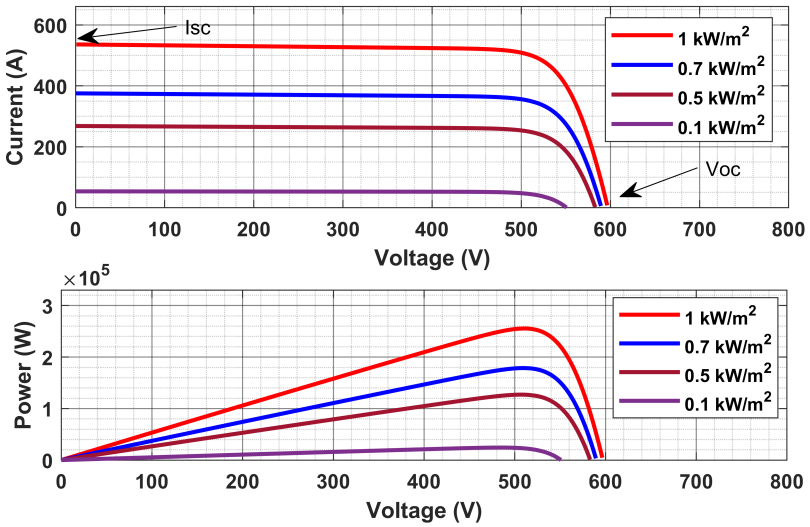


Figure II.4: P-V characteristics with different irradiance for the PV array

### II.2.2.2 Effect of temperature

Temperature has a significant impact on the voltage characteristics of a PV cell or module (P-V) when the temperature changes from 25°C to 55°C. As the temperature rises, the open-circuit voltage (Voc) decreases, while the short-circuit current (Isc) changes less. These adjustments result in a decrease in the maximum power output and efficiency of the PV device. The Figure II.5 shows the effect of temperature on output power.

## II.2.3 DC-DC converters

A DC-DC converter is a circuit that converts DC voltage levels. This circuit is widely used in a variety of applications and is based on inductors, capacitors, and switches such as MOSFET or IGBT. It is possible to define three basic topologies for DC-DC converter circuits. As shown in Table II.2, in this section, we introduce the principle of the boost converter.

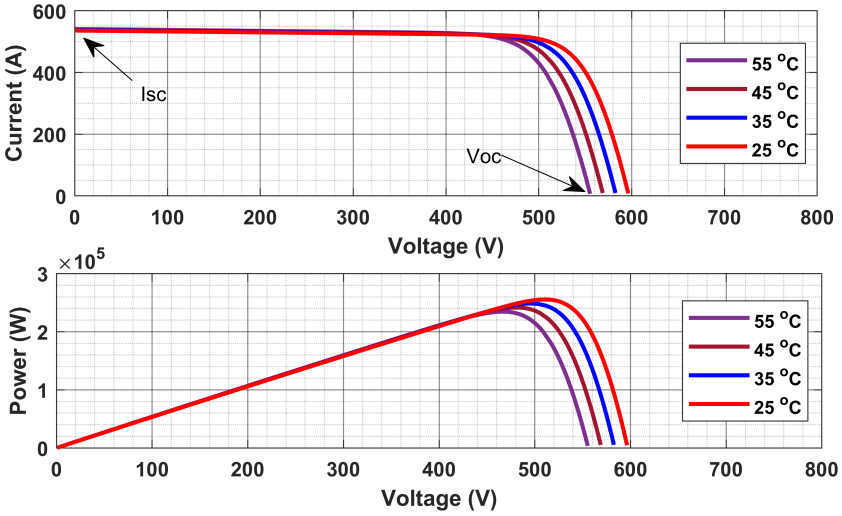


Figure II.5: Temperature effect on the PV characteristics

| Type of Converter | Equivalent Circuit | Duty Cycle | Function |
|---|---|---|---|
| Buck Converter | 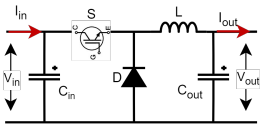 | $D = \frac{V_{out}}{V_{in}}$ | Reduces the DC output voltage $V_{out}$ relative to the input voltage $V_{in}$. |
| Boost Converter | 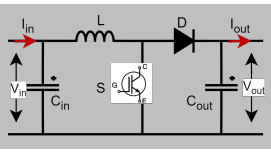 | $D = 1 - \frac{V_{in}}{V_{out}}$ | Increases the DC output voltage $V_{out}$ relative to the input voltage $V_{in}$. |
| Buck–Boost Converter | 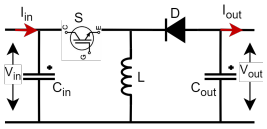 | $\frac{V_{out}}{V_{in}} = -\frac{D}{1-D}$ | Produces an output voltage $V_{out}$ that can be higher or lower than the input voltage $V_{in}$, depending on the duty cycle $D$. |

Table II.2: Types of converter topologies

### II.2.3.1 Modeling of DC/DC boost converter

The boost converter functions as a step-up converter, thereby increasing the output voltage relative to the input voltage at the same time. It operates in a manner opposite to that of the buck converter [58]. The underlying operating idea is the utilization of a Pulse Width Modulation (PWM) pulse to regulate the switch's opening and shutting. In the active state of the switch (case $S_{on}$), the circulation of electric current via the inductor

(L) produces a magnetic field, which is then storing it as an inductive voltage.

On the other hand, in the event that the switch is inactive (case $S_{off}$), the coupled effect of the induced voltage and the input voltage results in the charging of the output capacitor (Cout) to a magnitude that exceeds the original input voltage [59]. Figure II.6 presents an illustration of the design of the boost converter, whereas Figure II.8 showcases the configurations corresponding to the two distinct operating states. Figure II.7 shows a schematic diagram of the dynamic variables X of the boost converter relative to the Ts period during switch states.

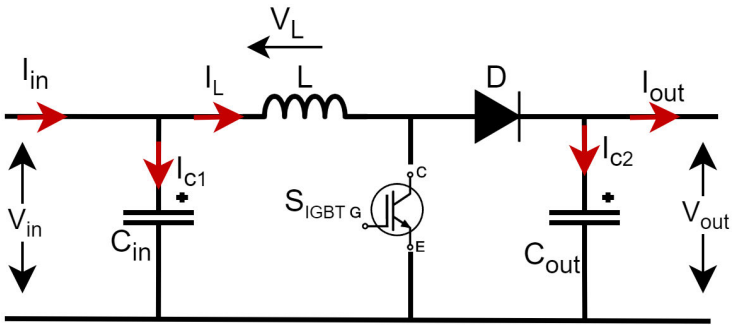


Figure II.6: Design of the boost converter

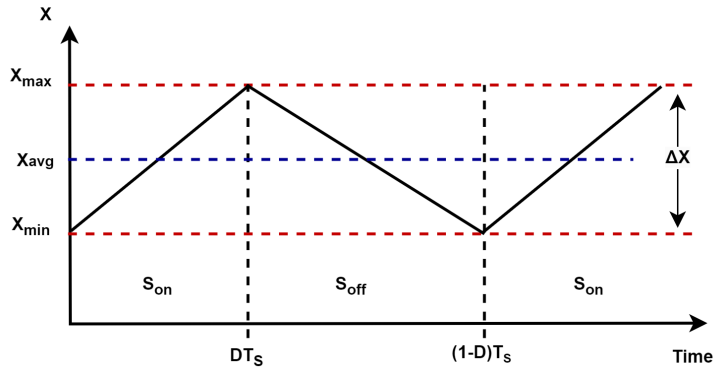


Figure II.7: Waveform of dynamic variables X of a boost converter

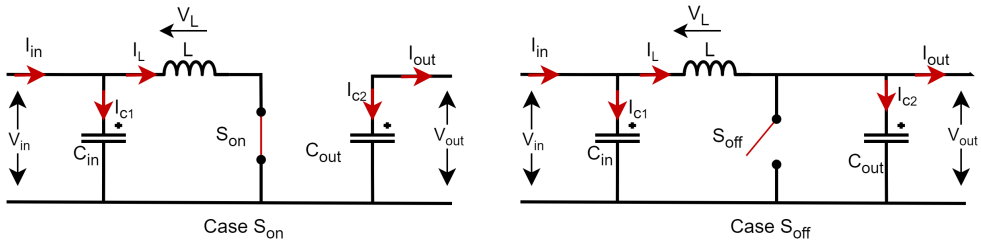


Figure II.8: Configuration of boost converter in the two operating cases ($S_{on}$ and $S_{off}$)

**- in the case $S_{on}$ :** $(0 \leq \mathrm{t} \leq \mathrm{DT_s})$

By applying Kirchhoff's law the equations can be written for the current $I_{c1}$ and $I_{c2}$ entering the capacitor $C_{in}$ and $C_{out}$ respectively and the inductor voltage $V_L$ :

$$\begin{cases} I_{C1}(t) = C_{in}\frac{dV_{in}(t)}{dt} = I_{in}(t) - I_L(t) \\ I_{C2}(t) = C_{out}\frac{dV_{out}(t)}{dt} = -I_{out}(t) \\ V_L(t) = L\frac{dI_L(t)}{dt} = -V_{in}(t) \end{cases} \tag{II.10}$$

**- in the case $S_{off}$ :** $(\mathrm{DT_s} \leq \mathrm{t} \leq \mathrm{T})$

In this case, the equations can be written for the current $I_{c1}$ and $I_{c2}$ entering the capacitor $C_{in}$ and $C_{out}$ respectively and the inductor voltage $V_L$ :

$$\begin{cases} I_{C1}(t) = C_{in}\frac{dV_{in}(t)}{dt} = I_{in}(t) - I_L(t) \\ I_{C2}(t) = C_{out}\frac{dV_{out}(t)}{dt} = I_L(t) - I_{out}(t) \\ V_L(t) = L\frac{dIL(t)}{dt} = V_{in}(t) - V_{out}(t) \end{cases} \tag{II.11}$$

To find a dynamic representation valid for the entire Ts period, the following expression is generally used [60]:

$$< \frac{dx}{dt} > T_s = \frac{dx}{d_{DTs}} + \frac{dx}{dt_{(1-D)TS}}(1-D) \tag{II.12}$$

Where $\frac{dx}{dt}$ is the average value of the derivative of x over a period Ts.

Applying Eq (II.12) to the systems of Eq (II.10) and (II.11), we obtain the equations governing the system over a whole period. This gives us the approximate model of the boost converter as follows:

$$\begin{cases} I_L = I_{in} - C_{in}\frac{dV_{in}(t)}{dt} \\ I_{out} = (1-D)I_L - C_{out}\frac{dV_{out}(t)}{dt} \\ V_{in}(t) = L\frac{dI_L}{dt} + (1-D)V_{out} \end{cases} \tag{II.13}$$

We can calculate the duty cycle (D) is related to the output voltage Vout and the input voltage Vin by the following equation where D is value ranges 0 and 1:

$$D = 1 - \frac{V_{\text{in}}}{V_{\text{out}}} \tag{II.14}$$

### II.2.3.2 Selection of the inductor

The boost inductance value is determined using the maximum allowable ripple current typically ranging from 20% to 30% of the maximum expected input DC current $I_{in}$ the minimum duty cycle, and maximum input voltage. The switching frequency determines the optimal value, typically set at 95% or higher, to optimize the boost inductor's operation. The inductor value can be expressed using Eq (II.15) at the threshold between continuous and discontinuous modes [61].

$$\begin{cases} L_b = \frac{D \cdot R_0 \cdot (1-D)^2}{2 \cdot f_{sw}} \\ L = \frac{V_{in} \cdot D}{f_{sw} \cdot \Delta I_L} \\ \Delta I_L = 20\% \times I_{\text{in(max)}} \end{cases} \tag{II.15}$$

The value of inductance must be greater than the critical inductance ($L > L_{boundary}$).

### II.2.3.3 Selection of the capacitor

The capacitor is chosen based on the change in voltage ripple, taking into account a voltage ripple value of 5%. The following equation is used to determine the minimum capacitor value [58].

$$C_{min} = \frac{V_{\text{out}} \cdot D}{R_0 \cdot f_{sw} \cdot \Delta V_{\text{ri}}} \tag{II.16}$$

### II.2.4 Modeling the three-phase inverter

Figure II.9 shows a common configuration of a three-phase forced-switching VSC based on IGBTs with antiparallel diodes. Current is delivered in both directions through each bridge arm due to the unidirectional characteristic of the diodes and the voltage polarity applied to each IGBT and switching diode combination, giving three diodes with a phase shift of 120 degrees.

The flow of power is reversed by changing the direction of the DC, which is achieved by

adjusting the DC voltage of the converter's opposite terminals, allowing the DC to flow in the desired direction. The DC power supply is provided by capacitors that can store a large amount of energy. Design aspects to consider include active and reactive power generation capability, injected harmonics limits, switching losses, and the cost of the design [62].

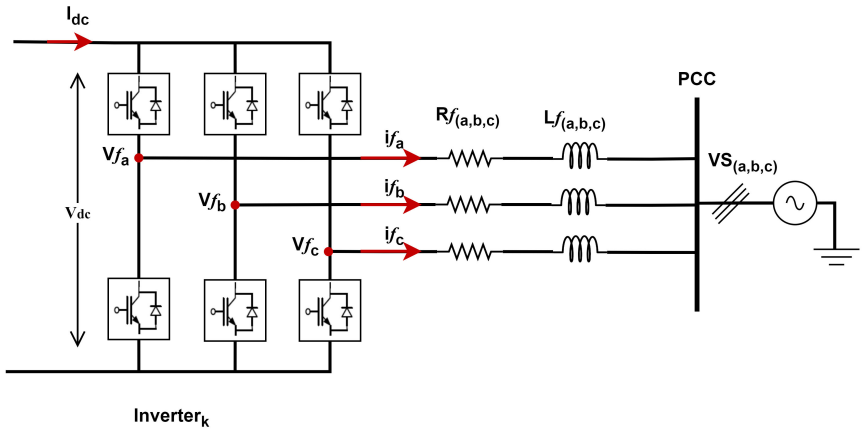


Figure II.9: Equivalent diagram of a three-phase inverter

In systems in balance, the source voltage is represented as follows:

$$\begin{cases} Vs_a(t) = V_m \cos(\omega t) \\ Vs_b(t) = V_m \cos(\omega t - 2\pi/3) \\ Vs_c(t) = V_m \cos(\omega t + 2\pi/3) \end{cases} \tag{II.17}$$

The inverter is linked to a filter inductor $L_f$ and resistance $R_f$, a voltage equation in $(abc)$ coordinates is given by:

$$\begin{cases} Vs_a = V_{f_a} - L_{f_a} \frac{dif_a}{dt} - R_{f_a} i_a \\ Vs_b = V_{f_b} - L_{f_b} \frac{dif_b}{dt} - R_{f_b} i_b \\ Vs_c = V_{f_c} - L_{f_c} \frac{dif_c}{dt} - R_{f_c} i_c \end{cases} \tag{II.18}$$

By applying the Concordia-Clark transform and the Park transform ,respectively to equations III.5 [63], the model can be represented in the synchronous frame by:

$$\begin{cases} L_f \frac{di_d}{dt} = -R_f i_d + L_f \omega i_q + V_d - V s_d \\ L_f \frac{di_q}{dt} = -R_f i_q - L_f \omega i_d + V_q - V s_q \end{cases} \tag{II.19}$$

### II.2.5 Modeling of wind energy conversion system

Wind turbine modeling is an intricate endeavor that seeks to represent the physical and mechanical properties of wind turbines within a computational framework or an analogous environment. The complexity of the modeling task is compounded by the diverse range of factors that influence wind turbine functionality [64]. To simulate a wind turbine effectively, the process involves replicating the essential constituents of its modeling dimensions. Within the realm of wind energy conversion systems, a plethora of topologies exists, each aligned with a particular genre of generator technology [65]. In the current study for a wind turbine configuration that incorporates a permanent magnet synchronous generator (PMSG) in conjunction with a switching mode rectifier-diode and a DC/DC boost converter. The rationale for this selection is anchored in several key features intrinsic to the system [66]:

- The PMSG is capable of self-excitation, negating the need for external power sources to initiate electricity generation.
- The output voltage of the accompanying boost converter is adjustable, facilitating compatibility with the input demands of the subsequent inverter stage.
- The system boasts simplicity in control, which streamlines the management of power output and system stability.
- The cost-effectiveness of this arrangement, when compared to alternative setups, presents a financially viable solution for wind power generation.

These attributes collectively justify the selection of the topology based on PMSG, underscoring its suitability for effective and efficient wind energy harnessing. A simplified

diagram of the components of the wind turbine is depicted in Figure II.10. The elements of the wind turbine are:

1. Aerodynamic model (Wind turbine rotor).
2. Mechanical model ( Drive train).
3. Permanent magnet synchronous generator (PMSG).
4. Electrical model (Rectifier-diode/Boost converter DC-DC/Inverter)
5. Transformer.

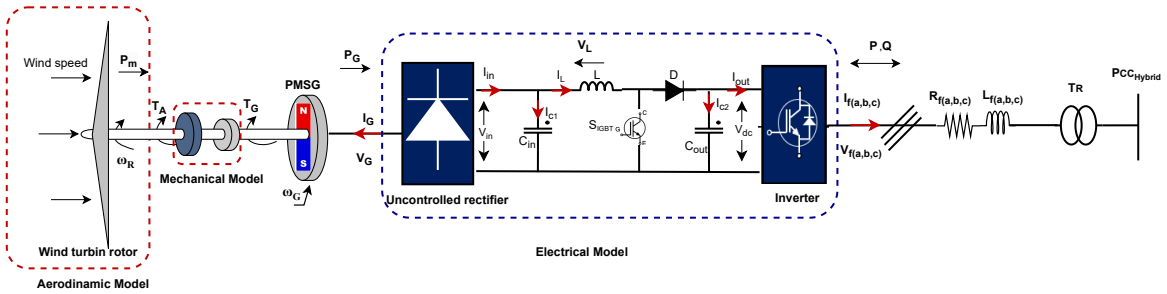


Figure II.10: the components of the wind turbine

### II.2.5.1 Aerodynamic modeling

The mathematical equation for the aerodynamic force of wind turbines is essential in modeling wind energy. It is typically derived from principles of aerodynamics and mechanics and relates to various concepts within wind energy. According to [67], to analyze wind turbine performance, several factors are essential. Air density ($\rho$) in $[kg = m^3]$ affects the kinetic energy available for electricity generation. The swept area (A) in $[m^2]$ is calculated using ($\pi R^2$), where (R) in [m] is the radius of the blade's rotation. Wind speed ($V_\omega$) in [m/s] significantly influences power output, which increases with the cube of wind speed. The power factor (Cp) measures the turbine's efficiency and varies depending on design and operating conditions.

The tip speed ratio ($\lambda$) is crucial for optimizing aerodynamic efficiency by comparing the speed at the blade tips to the wind speed. Adjusting the blade pitch angle ($\beta$) helps

regulate the turbine's rotational speed and maximizes power generation across different wind conditions. It can be expressed by the following mathematical aerodynamic model:

$$P_{aero} = \frac{1}{2}\rho A V_{\omega}^{3} \tag{II.20}$$

The mechanical power $P_m$ in [Nm= s], is given by the formula :

$$P_m = P_{aero}.C_p(\lambda, \beta) \tag{II.21}$$

Therefore, by substituting Eq (II.20) into Eq (II.21), the equation takes the form:

$$P_m = \frac{1}{2}\rho A V_w^3 C_p(\lambda, \beta) \tag{II.22}$$

$C_p(\lambda, \beta)$ is a nonlinear function related to $\lambda$ and $\beta$ which can be described as follows:

$$C_p(\lambda, \beta) = 0.5176 \cdot \beta \left(\frac{116}{\lambda_i} - 0.4 \cdot \beta - 5\right) \exp\left(\frac{-21}{\lambda_i}\right) + 0.0068 \cdot \lambda \tag{II.23}$$

where is $\lambda_i$ determined using :

$$\frac{1}{\lambda_i} = \frac{1}{(\lambda + 0.08 \cdot \beta)} - \frac{0.035}{1 + \beta^3} \tag{II.24}$$

The mechanical torque $T_A$ in [Nm] in a wind turbine can be related to the mechanical power $P_m$ using the angular speed $\omega_R$ of the rotor as given by the equation:

$$T_A = \frac{P_m}{\omega_R} \tag{II.25}$$

And the angular speed $\omega_R$ is given by :

$$\omega_R = \lambda \cdot \frac{V_w}{R} \tag{II.26}$$

#### II.2.5.2 Characteristics of wind turbine power

The power characteristics of wind turbines are essential to understanding how to optimize their design and operation. Weather conditions, blade design, and operating strategies significantly impact performance; generally, wind speed and blade pitch angle are the most important effects on performance.

### II.2.5.3 Effect of pitch angle

The pitch angle significantly affects the power curve of a wind turbine. Changes in tilt angle can lead to significant changes in power output, especially at low wind speeds, and from Figure II.11, it is clear that the power factor (Cp) is affected by changes in tilt angle and affects the power production as shown in Eq II.21.

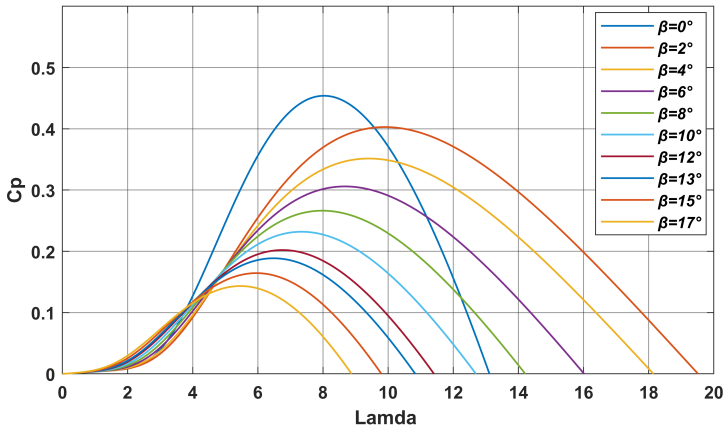


Figure II.11: Characteristic curves of a wind turbine at various pitch angles.

### II.2.5.4 Effect of wind speed

Figure II.12 shows that a higher wind speed increases the output power up to (12 m/s), where the output power reaches the maximum value. Higher speeds produce more power, but the turbine must be carefully controlled to avoid damage.

Different wind speeds make it possible to define four power zones, as shown in Figure II.12, the power curve of a wind turbine (Siemens-WT-2.3-108) [68] where Zone 1 refers to an area where there is no power generation due to wind speeds being below the minimum speed required for the wind turbine to start generating power. Zone 2, also known as the Cut-in Speed area, refers to the speed range of 3 to 4 m/s at which the turbine starts generating electricity. Within Zone 3, which corresponds to the turbine's rated speed, it achieves its maximum power output, often ranging from 11 to 15 m/s.

Beyond this speed, the turbine may decrease its output to prevent any potential harm. Within Zone 4, which is the Cut-out Speed range, the wind turbines will cease operation automatically as a safeguard for the wind turbine components when the wind speed exceeds 25 m/s.

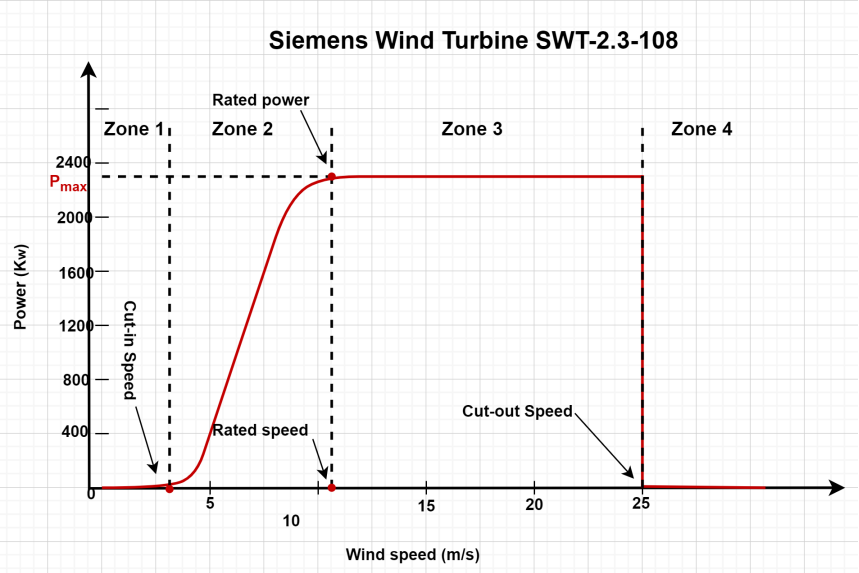


Figure II.12: characteristics of wind turbine power

### II.2.5.5 Mechanical modeling

The Figure II.13 illustrates the mechanical two-masses configuring of the drive train, indicating the moments of inertia for the rotor and generator wind turbines as $J_R$ and $J_G$, in $[Kg.m^2]$ respectively, are coupled by a rigid shaft.

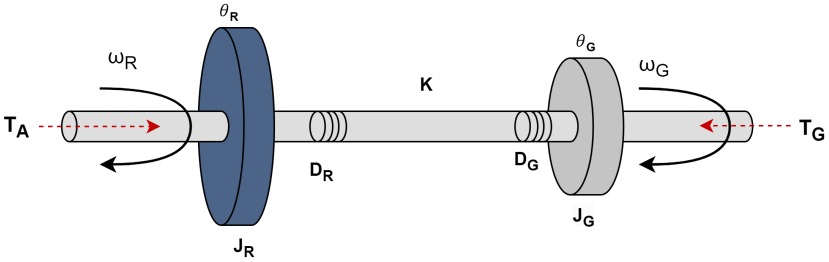


Figure II.13: Two-masses configuring of the drive train

The dynamic equations for the two-mass model of the drive train can be described as follows:

$$\begin{cases} J_R \frac{\mathrm{d}}{\mathrm{d}t}\omega_{\mathrm{R}} = T_A - D_R \frac{\mathrm{d}}{\mathrm{d}t}\omega_{\mathrm{R}} - k\left(\theta_R - \theta_G\right) \\ J_G \frac{\mathrm{d}}{\mathrm{d}t}\omega_{\mathrm{G}} = T_G - D_G \frac{\mathrm{d}}{\mathrm{d}t}\omega_{\mathrm{G}} + k\left(\theta_R - \theta_G\right) \end{cases} \tag{II.27}$$

The rotor and generator angular speeds are in [rad/s] and are given by:

$$\begin{cases} \omega_R = \frac{d\theta_R}{dt} \\ \omega_G = \frac{d\theta_G}{dt} \end{cases} \tag{II.28}$$

where $D_R$ and $D_G$ are the rotor and generator damping in [Nm/Rad/s], respectively. K is the shaft stiffness in [Nm/Rad], while $\theta_R$ and $\theta_G$ are the rotor and generator rotational angles in [Rad], respectively.

#### II.2.5.6 Modeling of PMSG

PMSGs have become integral to the advancement of wind turbine technologies, primarily due to their operational efficiency and durability. The absence of a gearbox in their design simplifies the mechanical structure, leading to reduced maintenance needs [69]. The PMSG's stator is characterized by a trio of sinusoidally distributed windings, phase-shifted by 120 degrees electrically, which is a standard approach to modeling for accurate analysis [70]. These generators are particularly advantageous in direct-drive applications for offshore wind turbines, where they convert mechanical to electrical energy with high reliability, attributed to the consistent magnetic field provided by the embedded permanent magnets, thus negating the requirement for external electrical excitation [71]. The PMSG model is simplified in the d-q axis. Figure II.14 presents the equivalent circuit diagram of the PMSG .

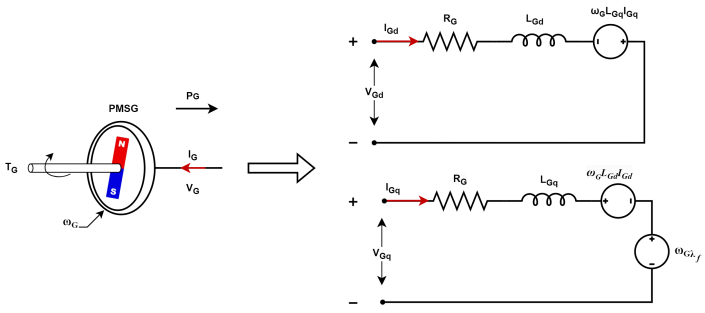


Figure II.14: Diagram equivalent of a PMSG Circuit in d-q axes

From the simplified circuit in Figure II.14, the voltages $v_{Gd}$ and $v_{Gq}$ of the PMSG in the d-q axis are as follows:

$$\begin{cases} v_{Gd} = R_G i_{Gd} + L_{Gd}\frac{di_{Gd}}{dt} - \omega_G \lambda_{Gq} \\ v_{Gq} = R_G i_{Gq} + L_{Gq}\frac{di_{Gq}}{dt} + \omega_G \lambda_{Gd} \end{cases} \tag{II.29}$$

Where

$v_{Gd}$ and $v_{Gq}$: The voltage of stator across the d-q axis in [V], respectively.

$i_{Gd}$ and $i_{Gq}$: The current of stator across the d-q axis in [A], respectively.

$R_G$: The equivalent resistance of the stator winding [Ω] .

$L_{Gd}$ and $L_{Gq}$: The equivalent inductance of the stator in the d-q axis in [H], respectively.

The flux of the stator can be defined as follows:

$$\begin{cases} \lambda_{Gd} = L_{Gd} I_{Gd} + \lambda_f \\ \lambda_{Gq} = L_{Gq} I_{Gq} \end{cases} \tag{II.30}$$

with

$\lambda_{Gd}$ and $\lambda_{Gq}$ :The flux of stator across the d-q axis in [Wb], respectively.

$\lambda_f$ :The permanent magnet flux. [Wb]

By neglecting losses, the electric torque developed by the generator $T_G$ is expressed in units of [N.m] :

$$T_G = 3/2 \cdot p\,(\lambda_{Gd} I_{Gq} - \lambda_{Gq} I_{Gd}) \tag{II.31}$$

Here, (p) represents the number of pole pairs of the generator. Furthermore, the electric power $P_G$ on the converter side of the generator, as given by:

$$P_G = \omega_G T_G = -3/2(V_{Gd} I_{Gd} + V_{Gq} I_{Gq}) \tag{II.32}$$

#### II.2.5.7 Modeling the three-phase diode rectifier

A diode rectifier operates as an AC/DC converter, enabling the transformation of electrical power from an AC source into a DC output, as shown in Figure II.15. Widely

recognized for its simplicity, cost-effectiveness, and durability, the diode rectifier remains a foundational component in power electronics applications. Despite its advantages, this type of rectifier is limited by its unidirectional power flow, meaning it cannot facilitate energy transfer back to the AC side. [72].

This rectifier structure includes six diodes arranged in a three-phase bridge configuration: diodes D1, D3, and D5 with cathodes aligned to permit the forward flow of the DC, $I_{dc}$, and diodes D4, D6, and D2 with anodes positioned to establish the return path for $I_{dc}$. When connected to a PMSG, the three-phase AC power is rectified, producing a pulsating DC voltage.

However, one challenge of the diode rectifier is the generation of harmonic distortion on the AC side, primarily the 5th and 7th harmonics [73]. These harmonics can impact power quality and require additional filtering measures to meet grid compliance standards. Moreover, since the rectified output has a ripple, additional capacitive or inductive filtering may be necessary to smooth the DC voltage. The rectifier's reliance on passive components further adds to its ruggedness but can limit efficiency at higher power levels due to conduction losses in the diodes.

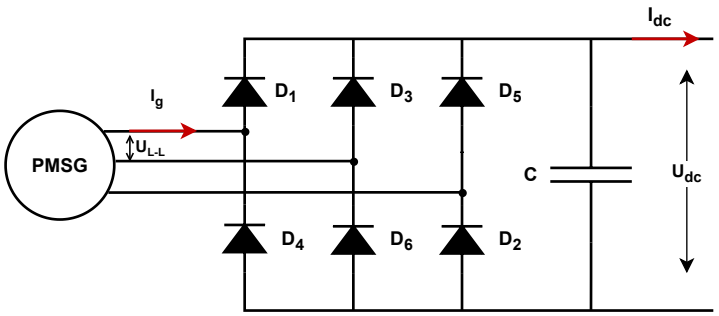


Figure II.15: Diagram of diode rectifier

### II.2.5.8 Transformer and offshore grid model

The wind turbine transformer $T_W$ is responsible for stepping up the grid-side converter voltage. In this modeling approach, the shunt branches of the transformer are omitted because their impedances are considerably larger than those of the series components.

As a result, the effect of the shunt impedances on power dynamics can be safely ignored without affecting the model's precision. Figure II.16 presents the electrical schematic of the grid converter of the wind turbine linked to the offshore AC grid via the transformer $T_W$. It is noteworthy that the transformer is depicted using its equivalent impedance, with $R_{TW}$ and $L_{TW}$ representing the resistive and inductive elements, respectively.

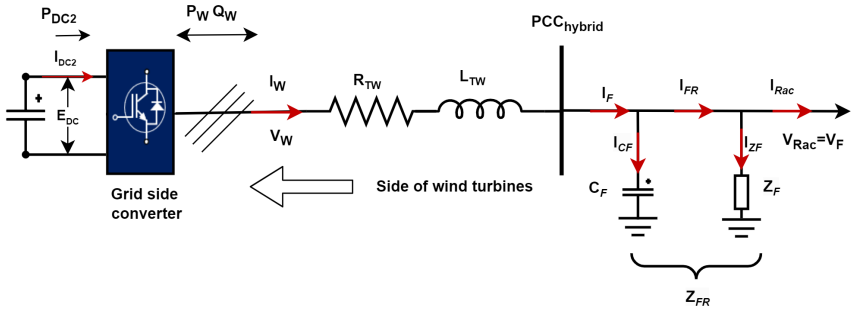


Figure II.16: Integration of wind turbines into the grid

The dynamic voltages of this simplified model in synchronous (dq) coordinates can be written as follows:

$$\begin{cases} V_{Wd} = R_{Tw} I_{Fd} + L_{Tw} \frac{dI_{Fd}}{dt} - L_{Tw} I_{Fq} \omega_{dq} + V_{Fd} \\ V_{Wq} = R_{Tw} I_{Fq} + L_{Tw} \frac{dI_{Fq}}{dt} + L_{Tw} I_{Fd} \omega_{dq} + V_{Fq} \end{cases} \tag{II.33}$$

Here, the frequency $\omega_{dq}$ represents the rotational synchronous frame in [rad/s]. The grid voltages $V_W$ and $V_F$ are stated in [V], while the current generated by the wind turbine $I_F$ is expressed in [A].

### II.2.6 Modelling a distributed offshore wind farm

After acquiring a single model of the wind turbine, it is feasible to create a corresponding model for the entire offshore wind farm. The aerodynamic and mechanical parameters will remain consistent with those of the individual wind turbines. Figure II.17 depicts the distributed configuration of an offshore wind farm consisting of (n) wind turbines.

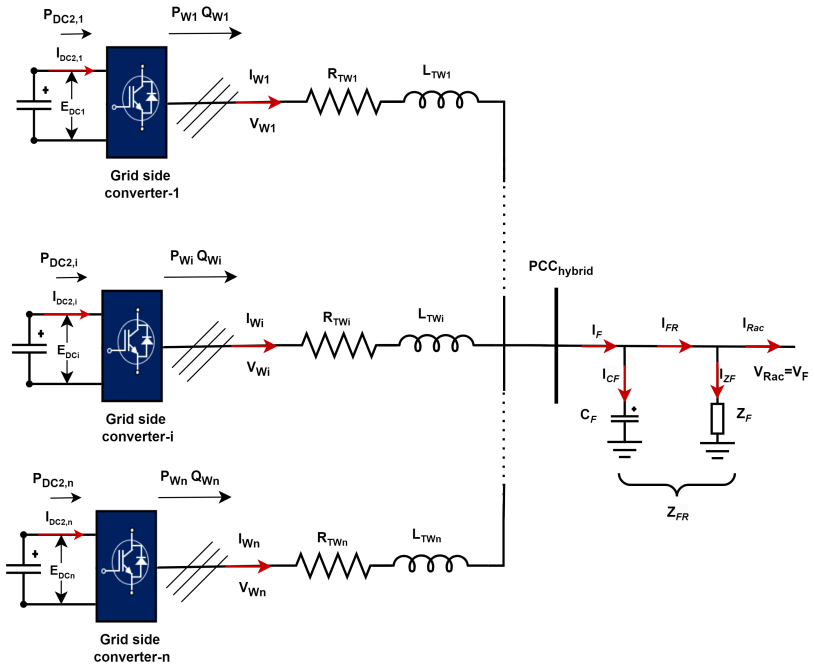


Figure II.17: Model of offshore wind farm (i=1,2,3,..)

The equations following illustrate the model electrical of the wind turbine (i-th) connected to ($PPC_W$) of the offshore (AC) grid.

The equations of modeling a PMSG on the d-q axis:

$$\begin{cases} \frac{dI_{\mathrm{Gdi}}}{dt} = -\frac{R_{\mathrm{Gi}}}{L_{\mathrm{Gdi}}} I_{\mathrm{Gdi}} + \frac{L_{\mathrm{Gqi}}}{L_{\mathrm{Gdi}}} \omega_{\mathrm{Gi}}\, I_{\mathrm{Gqi}} + \frac{1}{L_{\mathrm{Gdi}}} V_{\mathrm{Gdi}} \\ \frac{dI_{\mathrm{Gqi}}}{dt} = -\frac{L_{\mathrm{Gdi}}}{L_{\mathrm{Gqi}}} \omega_{\mathrm{Gi}}\, I_{\mathrm{Gdi}} - \frac{R_{\mathrm{Gi}}}{L_{\mathrm{Gqi}}} I_{\mathrm{Gqi}} + \frac{1}{L_{\mathrm{Gqi}}} V_{\mathrm{Gqi}} - \frac{1}{L_{\mathrm{Gqi}}} \omega_{\mathrm{Gi}}\, \lambda_{fi} \end{cases} \tag{II.34}$$

The equation of power balance at the generator side converter:

$$\begin{cases} P_{Gi} = -3\,(V_{Gdi} I_{\mathrm{Gdi}} + V_{Gqi} I_{\mathrm{Gqi}}\,) \\ P_{DC1i} = E_{DCi} I_{DC1i} \end{cases} \tag{II.35}$$

The equation of the dynamic DC-Link for Back-to-Back :

$$I_{DC1} - I_{DC2} = C_{DCi} \frac{dE_{DCi}}{dt} \tag{II.36}$$

The equation of power balance at the grid side converter with $n_i$ represents a number of wind turbines in the group :

$$\begin{cases} P_{DC2i} = E_{DCi}(I_{DC2i})n_i \\ P_{Wi} = 3(V_{Wdi}I_{Wdi} + V_{Wqi}I_{Wqi}) \end{cases} \tag{II.37}$$

The equation for the dynamics of the offshore grid integration can be expressed in d-q coordinates at synchronized rotation ($\omega_{dq}$) as follows:

$$\begin{cases} \frac{dI_{\mathrm{Wdi}}}{dt} = -\frac{R_{T_{Wni}}}{L_{T_{Wni}}}I_{Wdi} + \omega_{dq}I_{Wqi} + \frac{1}{L_{T_{Wni}}}V_{Wdi} - \frac{1}{L_{T_{Wni}}}V_{Fd} \\ \frac{dI_{\mathrm{Wqi}}}{dt} = -\omega_{dq}I_{Wdi} - \frac{R_{T_{Wni}}}{L_{T_{Wni}}}I_{Wqi} + \frac{1}{L_{T_{Wni}}}V_{Wqi} - \frac{1}{L_{T_{Wni}}}V_{Fq} \end{cases} \tag{II.38}$$

The dynamic voltages of the offshore grid can be expressed in d-q coordinates at synchronized rotation $\omega_{dq}$ as follows:

$$\begin{cases} \frac{dV_{\mathrm{Fd}}}{dt} = \frac{1}{C_F}\sum_{i=1}^{m} I_{Wdi} - \frac{1}{C_F}I_{FRd} + \omega_{dq}V_{Fq} \\ \frac{dV_{\mathrm{Fq}}}{dt} = \frac{1}{C_F}\sum_{i=1}^{m} I_{Wqi} - \frac{1}{C_F}I_{FRq} - \omega_{dq}V_{Fd} \end{cases} \tag{II.39}$$

## II.3 Modeling of HVDC-VSC link

The HVDC-VSC link used in the studied system consists of a controlled rectifier (VSC), a submarine DC cable, and an onshore inverter (VSC). This connection is linked to the offshore $PCC_{Hybrid}$ point at the first terminal, which uses two transformers and a compensation bank ($Z_{FR}$) to provide the required reactive power. At the opposite station, another transformer is connected to the terrestrial grid. Figure II.18 shows the basic elements of the proposed HVDC transmission system.

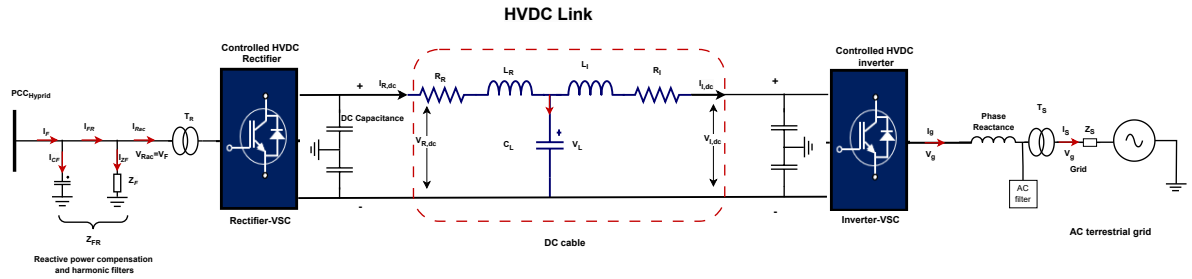


Figure II.18: Configuration of HVDC transmission, a compensation bank, and transformer

### II.3.1 Transformers

The fundamental role of transformers is the conversion of AC voltage into suitable levels to guarantee the correct operation of converters. Moreover, transformers support ancillary tasks like adjusting voltage, incorporating conversion modules, and providing insulation from the homopolar element. The leakage inductance of transformers employed in this transmission mode generally falls within the range of 0.1 pu to 0.2 pu [74].

### II.3.2 The phase reactance

Phase reactance is of paramount importance in AC systems, especially in the context of interfacing conversion units with the network, as it facilitates a reliable power exchange and diminishes the presence of harmonic distortion. This reactance, which emanates from the inductance or leakage inductance characteristics of an interface transformer, permits voltage discrepancies between the converter and the grid to manifest as circulating current, thereby enabling an efficient interaction between the two voltage sources. Phase reactors play a critical role in regulating both active and reactive power flows while simultaneously serving as AC filters, effectively addressing high-order harmonics generated by VSC. Generally, a phase reactance value of 0.15 per unit is implemented to bolster system stability and enhance power quality [75].

### II.3.3 Filters and DC capacitors

Depending on the AC grid, filters may be required to prevent harmonics from entering the converter station. On the other hand, the high frequency of switching in the converter unit makes the harmonics it generates more harmful to the equipment, but also easier to filter. ($Z_{FR}$) represents both the rectifier ($C_F$) shunt capacitor and the harmonic filter bank. Filters can be installed on the DC bus to limit DC voltage ripple without increasing the value of the DC capacitance. In addition, a DC capacitor is added to maintain a stable DC voltage while switching the switches of the switching unit.

### II.3.4 Voltage source converters

VSCs represent a pivotal technological advancement within HVDC systems. They facilitate the efficient transmission of electrical power and the adaptable management of electrical energy. Their prominence has escalated significantly owing to their capacity to enhance the integration of renewable energy resources and bolster electrical grids' stability.

The inverter-VSC utilizing the three-level neutral point clamped (NPC) topology marks a significant milestone in the power electronics field, especially for applications with medium and high power [76]. A primary benefit of the three-level NPC inverter is its capability to minimize harmonic distortion in output voltage and current, outperforming traditional two-level inverters.

An additional voltage level facilitates harmonic reduction by more accurately approximating a sinusoidal waveform, thereby enhancing the quality of power supplied to the load. The inverter incorporates clamping diodes and semiconductor switches such as IGBTs, with DC-link capacitors used to divide the input DC voltage into two equal parts, forming the neutral point. Clamping diodes link the neutral point to the middle point of the DC link capacitors, producing three voltage levels: positive, neutral, and negative. The semiconductor switches are configured in pairs, each governing the interaction between DC link capacitors and the output phase. This configuration allows for precise regulation of the output voltage through a carefully designed switching sequence [77]. This approach ensures uniform voltage distribution across the switches and minimizes switching losses.

We add the bank filter connected to the inverter and the grid to reduce harmonics in the output current. This configuration promotes the reduction of high-frequency harmonics, which is critical for maintaining power quality, minimizing interference with sensitive equipment, and ensuring stability and efficient performance. To enhance the harmonic composition of the voltage, three-level systems have been constructed, featuring levels of +1/2 Vdc, 0, and -1/2 Vdc. Figure II.19 illustrates a three-level HVDC converter that employs a configuration integrating three-level clamping diodes [78] [79].

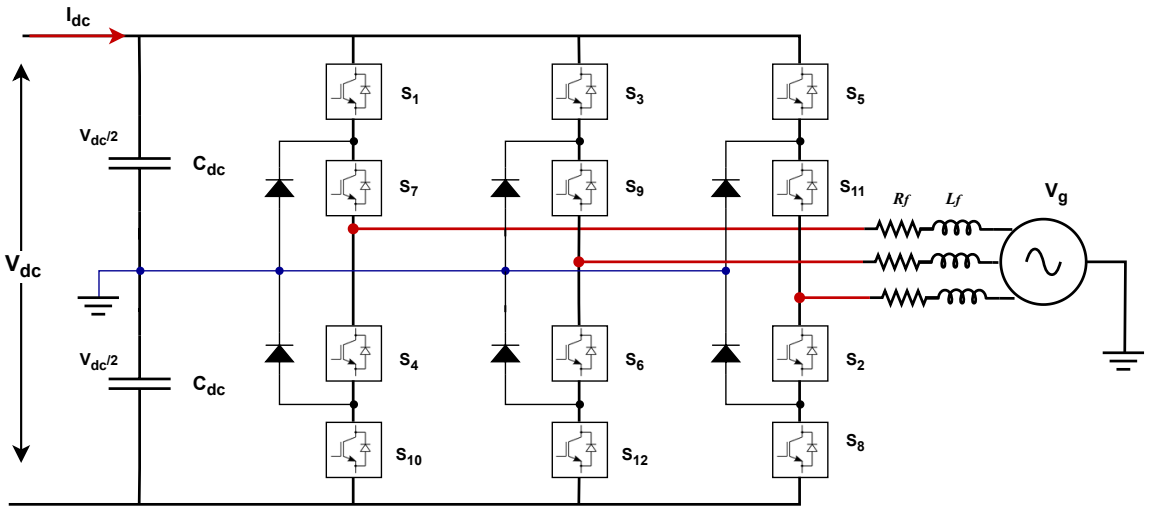


Figure II.19: The three-level HVDC converter

### II.3.5 DC cables

Due to the cable's sensitivity to DC faults, this type of connection is primarily implemented using underground or submarine cables. In addition, since the polarity of the DC voltage is never reversed, industrially insulated cables are used, which are more economical than conventional cables. The cable used in links of HVDC source converters is a recently designed variant, distinguished by insulation composed of an extruded polymer that exhibits exceptional resistance to DC voltage. This type of cable is the preferred choice for HVDC connections due to its mechanical strength, flexibility, and lightweight [80].

### II.3.6 Submarine cable modeling

A submarine cable is used to transmit electricity from an offshore facility to an onshore facility. The cable design incorporates a parabolic T-shaped DC transmission line, illustrated in Figure II.20. This cable operates at a voltage of 50 kV and has a power rating of approximately 3 MW.

The diagram of a circuit in Figure II.20 displays the "T" configuration, with $R_R = R_I$= 3.475 mΩ, $L_R = L_I$=0.3975 mH,$C_T$=0.5775 mF. Additionally, it shows $V_{R,dc}$ and $I_{I,dc}$ as the voltages across the rectifier and inverter, while $C_T$ denotes the overall capacitance of the direct current (DC) transmission line. $I_{R,dc}$ and $I_{I,dc}$ denote the DC currents on the

rectifier and inverter sides, respectively.

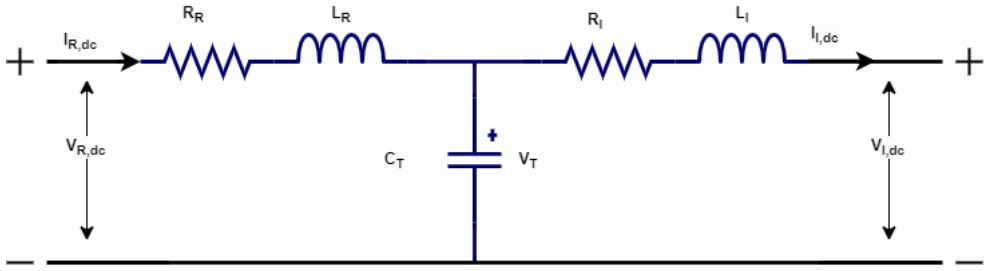


Figure II.20: An equivalent circuit for the DC cable 'T'

The dynamic equations according to the DC line model shown in Figure II.20 can be expressed as follows:

$$\begin{cases} \frac{d}{dt}I_{Rdc} &= -\frac{R_R}{L_R}I_{Rdc} + \frac{1}{L_R}V_{Rdc} - \frac{1}{L_R}V_T \\ \frac{d}{dt}I_{Idc} &= -\frac{R_I}{L_I}I_{Rdc} - \frac{1}{L_I}V_{Idc} + \frac{1}{L_I}V_T \\ \frac{d}{dt}V_T &= \frac{1}{C_T}I_{Rdc} - \frac{1}{C_T}I_{Idc} \end{cases} \tag{II.40}$$

### II.3.7 Power flow in interconnected AC systems

In interconnected AC systems, the active and reactive power flow is governed by a conduction impedance, along with the amplitude and phase angle between the two voltage vectors. Here, a VSC diagram illustrates the voltage source linked to an AC grid through a collected reactance, and Xr is a series inductor of the converter and transformer, as depicted in Figure II.21.

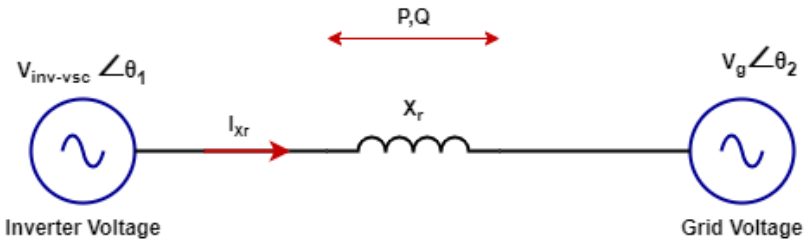


Figure II.21: The Relative angle of voltage and impedance

The flow of active power P from the converter to the AC grid is expressed as:

$$P = \frac{V_g V_{inv-vsc}}{X_r} \sin(\Delta\theta) \tag{II.41}$$

where $V_g$ denotes the AC grid voltage, while $V_{inv-vsc}$ represents the voltage across the VSC. $X_r$ is the reactance linking the VSC to $V_g$, and $\delta$ indicates the voltage angle between the VSC and $V_g$. Moreover, the reactive power exchanged between $V_{inv-vsc}$ and the $V_g$ can be expressed by the following equation:

$$Q = \frac{V_{inv-vsc}\left(V_{inv-vsc} - V_g \cos(\Delta\theta)\right)}{X_r} \tag{II.42}$$

The above equations show that when there is a variation in voltage phase angles, the active power component is zero, while the reactive power component depends on the difference in the magnitudes of the voltage, with the change in angle determined by:

$$\Delta\theta = \theta_1 - \theta_2 \tag{II.43}$$

- If $V_g > V_{inv-vsc}$, then Q is less than zero and indicates an inductive operation, which means that the VSC absorbs the reactive power.

- If $V_g < V_{inv-vsc}$, then Q is greater than zero and indicates a capacitive operation, which means that the VSC exports reactive power to the grid.

For equal voltage magnitudes, reactive power is zero, whereas active power varies with the voltage angle. A positive angle ($\Delta\delta > 0$) indicates that power flows from the VSC to the AC system (inverter mode), while a negative angle ($\Delta\delta < 0$) signifies power flow from the AC system to the VSC (rectifier mode). The power flow equations (II.41)-(II.42) demonstrate that four-quadrant power control is feasible. Although active and reactive power can be controlled independently, there is inherent coupling between the VSC and AC systems. The modulation index regulates the voltage amplitude and reactive power for reactive power control, while the valve ignition timing relative to the AC side voltage determines the phase angle of voltage and power flow [74].

From Figure II.22, the equations for the voltages and currents of the transformer can be defined as follows:

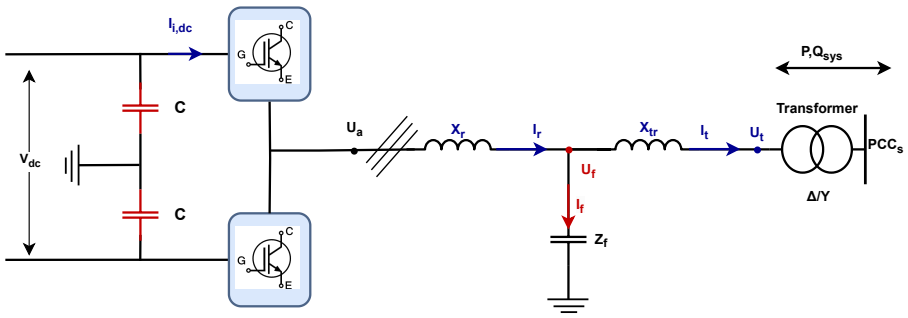


Figure II.22: Equivalent diagram of the VSC circuit

The converter voltage $U_a$ is defined by :

$$U_a = U_f + X_r I_r \tag{II.44}$$

The voltage at the AC filter node is denoted by $U_f$, and $X_r$ represents the reactance of the converter, while $I_r$ represents the current flow across the reactance of the converter.

The current expression $I_r$ is as follows:

$$I_r = I_t + I_f \tag{II.45}$$

where $I_t$ represents the overall current passing through the converter to the transformer and $I_f$ represents the current passing through the impedance of the filter.

$U_f$ is the voltage at the AC filter node given by :

$$U_f = U_t + X_{tr} I_t \tag{II.46}$$

where $U_t$ is the primary voltage of the transformer, and $X_{tr}$ is the reactance of the transformer.

The filter current $I_f$ is defined by the expression below:

$$I_f = \frac{U_f}{Z_f} \tag{II.47}$$

In an inverter-VSC configuration, the capacitor $C_t$ stabilizes the DC voltage and minimizes oscillations. We can draw the vector diagram from the previous converter equations, as shown in Figure II.23.

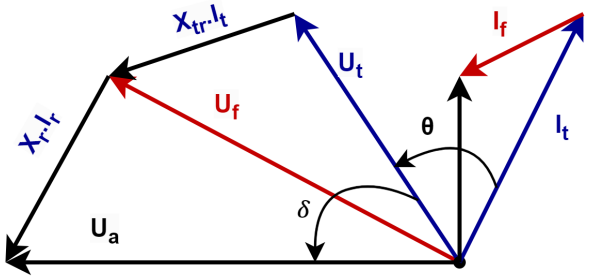


Figure II.23: The Vector diagram of the VSC circuit

From Figure II.23, $U_a$ can be approximately equal to $U - vsc$, considering that losses and distortions in the system are, theoretically, zero or minimal. $U_t$ can be equal to $U_g$ if the transformer ratio does not affect the final voltage, the angle $\delta$ represents the voltage angle between converter inductance and transformer impedances, and the angle $\theta$ indicates the relationship between the output voltage and current.

### II.3.8 The AC terrestrial grid

The generated hybrid renewable energy (PV and wind) is connected to the onshore grid at the station through an HVDC connection. To model the grid at the Pccs connection point, we use an equivalent Thevenin model consisting of an impedance $Z_s$ and a voltage source $V_g$ as shown in Figure II.24 [81]. where $\omega_g$ is the frequency of the grid and an impedance consists of resistance $R_g$ with inductance $L_g$ in series.

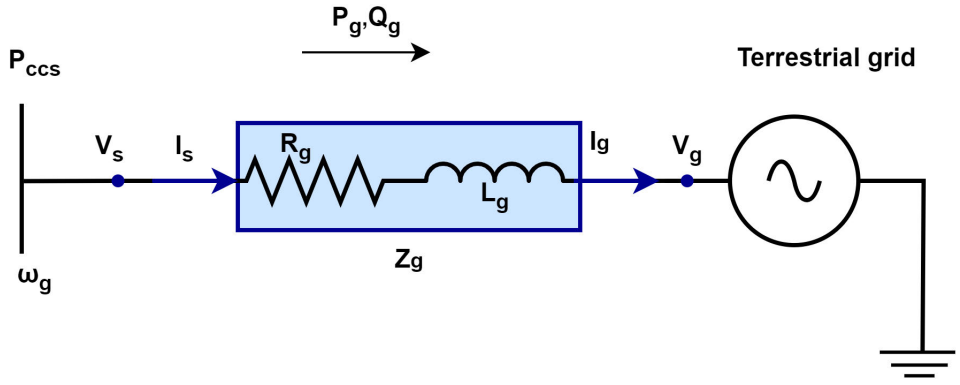


Figure II.24: Model of AC terrestrial grid

## II.4 Conclusion

In this chapter, we have presented the detailed and simplified mathematical modeling of hybrid renewable energy elements ( offshore wind farm and PV power plant ) connected to an HVDC transmission system based on the diode rectifier and inverter-VSC. The HVDC link utilizes a controlled diode bridge rectifier. The effects of this limitation will be processed through the control of the inverters for the renewable energy system.

The VSC is considered optimal, neglecting conduction and switching losses, as well as harmonics. For the AC grid, a simplified Thévenin equivalent model is used, with relatively high short-circuit power.

Based on the modeling of the previous system components, the next chapter will present control strategies and simulations for the system using the MATLAB software.

# Chapter III

# Control of a hybrid renewable energy system connected to a HVDC-VSC

## III.1 Introduction

The control of PV systems is crucial to maximize the efficiency and reliability of the energy generation from solar irradiance. PV systems employ advanced MPPT techniques to adapt to dynamic environmental conditions, such as changes in sunlight intensity and temperature. These systems also integrate grid-connected inverters that regulate active and reactive power, ensuring voltage stability and adherence to grid codes. Sophisticated control methods, including dq-axis control and predictive control algorithms, are commonly implemented to improve the system response to disturbances and improve overall performance in hybrid renewable energy setups.

Wind energy systems utilizing permanent magnet synchronous generators (PMSGs) require precise control to ensure efficient and stable operation under varying wind conditions. The control strategy for PMSG-based systems typically involves a full-scale converter, comprising a machine-side converter (MSC) and a grid-side converter (GSC). The MSC manages the generator's torque to optimize energy capture, while the GSC maintains the DC-link voltage and facilitates grid code compliance. Effective coordination of these converters ensures optimal performance, reduced mechanical stress, and improved energy integration in hybrid systems. The advanced control algorithms also enable the PMSG to operate at variable speeds, enhancing energy extraction efficiency. In our case, we relied on an uncontrolled rectifier on the machine side, tied to a boost converter and tied to a VSI.

HVDC systems based on VSC are essential for integrating hybrid renewable energy

systems into modern power grids. VSC-HVDC technology provides independent control of active and reactive power, supporting grid stability and facilitating long-distance power transmission with minimal losses. The control architecture consists of outer loops for power and voltage regulation, complemented by inner loops for current control to ensure fast dynamic response. When integrating PV and wind energy sources, VSC-HVDC systems enable seamless power exchange, maintaining system stability and ensuring high power quality, even under fluctuating generation and load conditions.

## III.2 Control system design for grid-connected converters

Grid-connected converters are employed in many applications, including distributed generation systems, active power filters, unity power factor (UPF) rectifiers, and high-voltage direct current (HVDC) systems. These converters serve the dual function of inverters when power is transferred from the DC to the AC side and rectifiers when power flows in the opposite direction. Despite variations in operational mode, their structural design and control capabilities remain largely consistent, differing primarily in the direction of power flow.

The principal control functionalities of these converters include the following: (a) regulation of AC voltage, (b) independent management of active and reactive power, (c) synchronization with the grid, (d) compliance with or exceeding harmonic standards, (e) operation under grid faults and distorted grid conditions, and (f) detection and isolation during islanding events. These functionalities are implemented through feedback controllers that regulate various control parameters.

Figure III.1 depicts the standard configuration of a grid-connected converter system. This configuration depicts a DC link feeding a voltage source inverter (VSI), which is managed through multiple control stages. Irrespective of the particular arrangements pertaining to the power stages, the grid-side converter and its control system remain consistent with the structure delineated in Figure III.1. The choice of control strategy is contingent

upon the desired control objectives, system stability requirements, and power quality considerations.

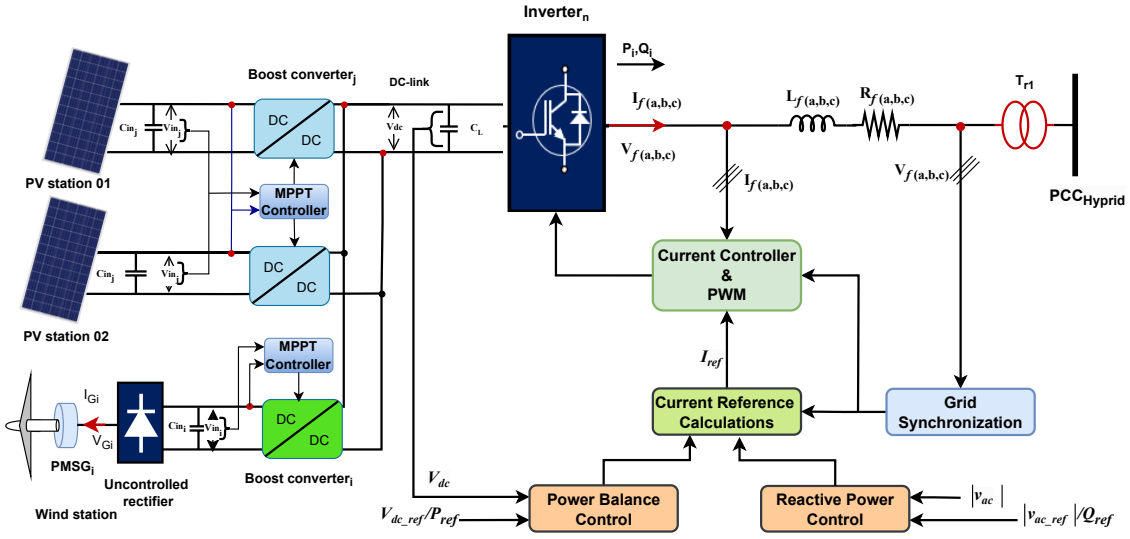


Figure III.1: The general configuration of the control of grid-connected converters

### III.2.1 Power controllers

An active power control loop, typically implemented as an outer loop, serves the function of regulating the active power delivered by the system. This loop generates a reference signal for the inner control loop through the implementation of various strategies, including instantaneous power balance or MPPT algorithms. When the instantaneous power-balance method is employed, the power control block utilizes the DC-link voltage as an input, comparing it with a predefined reference value. The fundamental premise of this methodology is the equilibrium between the energy supplied to the VSI and the energy it delivers [82].

When the power received by the VSI is equal to the power it supplies, the DC-link voltage remains stable. However, if the received power exceeds the delivered power, the excess energy is stored in the DC-link capacitor, thereby increasing its voltage. Conversely, when the delivered power exceeds the received power, the capacitor serves to compensate for the deficit, resulting in a voltage drop. By monitoring and adjusting the DC-link voltage, the system is able to effectively manage the delivery of active power [83].

In the case of renewable energy systems, MPPT algorithms are frequently used to

maximize power extraction [84]. As illustrated in Figure III.1, in microgrids, a central control station often provides active and reactive power references to maintain equilibrium between generation and demand within the local network. In such circumstances, the control loop employs the power reference directly, with the actual power delivered being measured and compared against this reference.

These control loops rely on feedback mechanisms to align actual system parameters with their reference values. A Proportional-Integral (PI) controller is commonly employed, as DC-link voltage and power values are scalar quantities, devoid of phase or frequency information. Using a first-order controller like the PI ensures simplicity and avoids increasing the system's order, thereby preserving phase margin and maintaining system stability [85].

## III.2.2 Current controllers

The output of the power controller serves as the input for the inner, faster-acting current controllers. The current control loops are responsible for generating the requisite voltage and frequency references for the subsequent PWM block. The voltage output from the inverter is calculated as the vector sum of the AC grid voltage and the combined voltage drop across the filter and grid impedances. Therefore, the current control algorithm must calculate the converter's output voltage for a specified power reference, taking into account the filter drop in order to ensure that the power flow aligns with the desired reference [86].

In the literature on grid-connected converters, a variety of current controllers have been proposed, each utilizing a different reference frame based on the specific application or control strategy [87]. The most commonly used reference frame controllers are as follows:

- Natural Reference Frame Controllers.
- Stationary Reference Frame Controllers.
- Synchronous Reference Frame Controllers.

### III.2.2.1 Natural reference frame (abc reference frame controllers)

In this control strategy, the variables are maintained in their original reference frame, which is referred to as the natural reference frame. Figure III.2 illustrates the control of the

VSI in the (ABC) reference frame [88], wherein the phase currents ($i_a$, $i_b$, $i_c$) are directly managed within this frame. It is unnecessary to transform the quantities into another reference frame for control purposes, as the comparison and control actions occur in the same reference frame. To regulate the three-phase currents, three separate controllers are required, and the neutral point of the output transformer must be connected to the inverter's ground point for independent phase current control. The outer loop typically employs simple PI controllers, as the controlled variables are DC values.

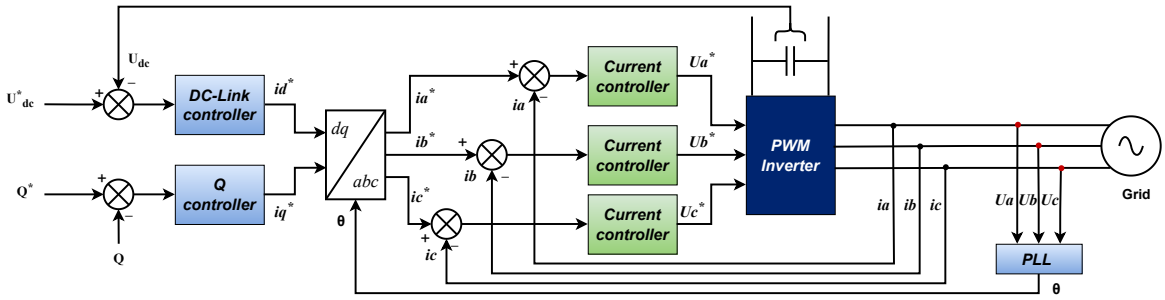


Figure III.2: Control of grid-connected VSI in abc reference frame

### III.2.2.2 Stationary $\alpha$-$\beta$ frame controllers

The control of the grid-connected VSI within the reference frame is illustrated in Figure III.3. This approach reduces the number of controlled parameters from three to two, albeit at the cost of additional computational complexity arising from the transformation of three-phase quantities into two-phase quantities. Conventional PI controllers are unsuitable in this context since the transformed quantities remain time-varying, resulting in persistent steady-state errors when managing AC signals. To address this limitation, Proportional Resonant (PR) controllers have been proposed as an alternative, capable of directly handling time-varying abc quantities effectively.

PR controllers are particularly effective for grid-connected systems. They ensure accurate tracking of AC reference signals with zero steady-state error and minimal phase delay [89]. However, a key drawback is their sensitivity to grid frequency variations. PR controllers rely on infinite gain at the grid frequency, making them susceptible to instability if the operating frequency deviates beyond a certain range. Expanding the width of the control band can mitigate instability but at the cost of increased steady-state er-

ror [90].Another advantage of PR controllers is their capability for harmonic compensation, which allows them to manage higher-order frequency components without impairing the control of the fundamental component. This feature enhances their performance in grid-connected applications by improving power quality and compliance with grid standards.

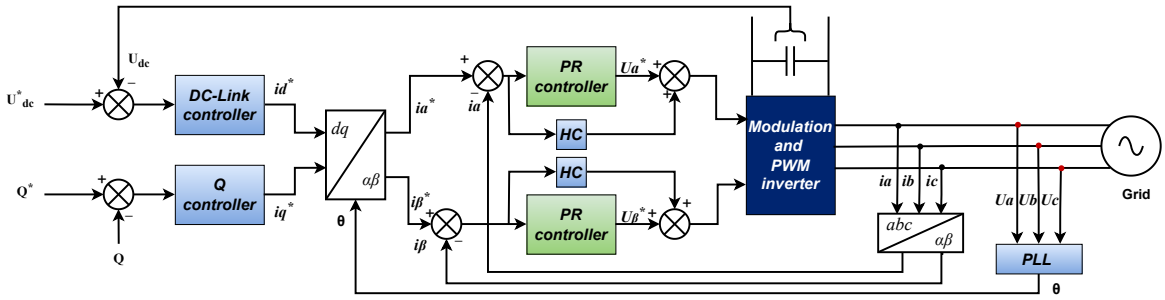


Figure III.3: Control of grid-connected VSI in $\alpha$-$\beta$ reference frame

### III.2.2.3 Synchronous Reference frame controllers

This control approach begins by converting AC signals into DC signals using transformations based on a synchronously rotating reference frame. These transformations enable the design of a DC control loop capable of accurately tracking AC signals with no steady-state error. To perform these transformations, knowledge of the phase of the mains voltage is essential [91]. Several methods for determining the instantaneous phase of the grid voltage have been discussed in the literature. Of these, the SRF-PLL is recognised as the most advanced and has therefore been used in this study.

The transformation of the three-phase load currents to the $\alpha$-$\beta$ system is as follows:

$$\begin{bmatrix} i_\alpha \\ i_\beta \end{bmatrix} = \frac{2}{3} \cdot \begin{bmatrix} 1 & -1/2 & -1/2 \\ 0 & \sqrt{3}/2 & -\sqrt{3}/2 \end{bmatrix} \cdot \begin{bmatrix} i_a \\ i_b \\ i_c \end{bmatrix} \tag{III.1}$$

In a balanced three-phase system, the scaling factor 2/3 is typically employed for amplitude-invariant transformations.

The rotating frame, aligned by $(\pi/2)$ behind the a-axis, is thus oriented at t=0 with the q-axis aligned with the a-axis. Consequently, the (d-q) components of load current can be obtained by:

$$\begin{bmatrix} i_d \\ i_q \end{bmatrix} = \begin{bmatrix} \sin(\theta) & -\cos(\theta) \\ \cos(\theta) & \sin(\theta) \end{bmatrix} \cdot \begin{bmatrix} i_\alpha \\ i_\beta \end{bmatrix} \tag{III.2}$$

Where $\theta$ represents the phase angle obtained through the utilisation of a PLL controller.

Simple PI controllers with a transfer function are used for control as follows:

$$F(s) = K_p + \frac{K_i}{s} \tag{III.3}$$

Here, $K_p$ denotes proportional gain, while $K_i$ represents integral gain.

Figure III.4 illustrates the circuit configuration of a three-phase grid-connected VSI. The inverter's three pole voltages are represented as $V_{fa}$, $V_{fb}$, and $V_{fc}$, while the corresponding grid voltages are denoted as $V_{sa}$, $V_{sb}$, and $V_{sc}$. In the diagram, $L_f$ signifies the filter inductance, $R_f$ accounts for the resistance from the inverter to the grid, and the currents injected into the grid for each phase are indicated as $i_{fa}$, $i_{fb}$, and $i_{fc}$.

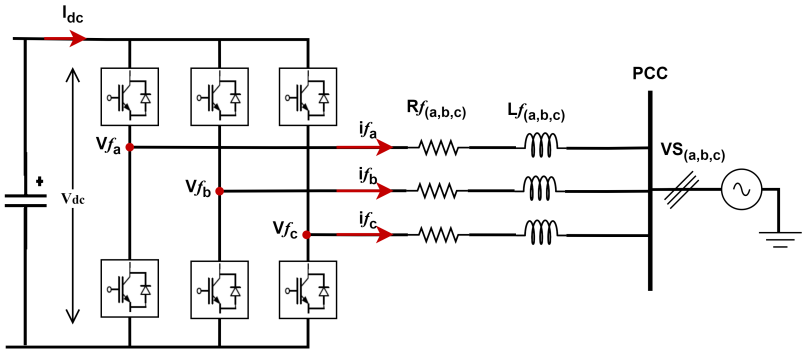


Figure III.4: Configuration of a three-phase grid-connected VSI

In systems in balance, the source voltage is represented as follows:

$$\begin{cases} Vs_a(t) = V_m \cos(\omega t) \\ Vs_b(t) = V_m \cos(\omega t - 2\pi/3) \\ Vs_c(t) = V_m \cos(\omega t + 2\pi/3) \end{cases} \tag{III.4}$$

The inverter is linked to a filter inductor $L_f$ and resistance $R_f$, a voltage equation in $(abc)$ coordinates is given by:

$$\begin{cases} Vs_a = V_{f_a} - L_{f_a}\frac{dif_a}{dt} - R_{f_a}i_a \\ Vs_b = V_{f_b} - L_{f_b}\frac{dif_b}{dt} - R_{f_b}i_b \\ Vs_c = V_{f_c} - L_{f_c}\frac{dif_c}{dt} - R_{f_c}i_c \end{cases} \tag{III.5}$$

By applying the Concordia-Clark transform and the Park transform ,respectively to equations III.5 [63], the model can be represented in the synchronous frame by:

$$\begin{cases} L_f\frac{di_d}{dt} = -R_f i_{_d} + L_f\omega i_q + V_d - Vs_d \\ L_f\frac{di_q}{dt} = -R_f i_q - L_f\omega i_d + V_q - Vs_q \end{cases} \tag{III.6}$$

The inverter output voltages $V_d$ and $V_q$ can therefore be written as follows:

$$V_d = V_{sd} + Ri_d + L_f\frac{di_d}{dt} + L_f\omega i_q \tag{III.7}$$

$$V_q = V_{sq} + Ri_q + L_f\frac{di_q}{dt} - L_f\omega i_q \tag{III.8}$$

The $d$-$q$ mathematical model reveals the inherent coupling between the variables on the $d$-axis and the variables on the $q$-axis, complicating the controller design. To address this challenge, a feedforward decoupling control strategy can be employed. By incorporating a PI regulator, stable closed-loop control of the system is achieved. The corresponding control equations are as follows:

$$\begin{cases} u_d = \left(K_p + \frac{K_i}{s}\right)(i_d^* - i_d) - \omega L i_q + e_d \\ u_q = \left(K_p + \frac{K_i}{s}\right)\left(i_q^* - i_q\right) + \omega L i_d + e_q \end{cases} \tag{III.9}$$

As indicated by Equation III.9, the feedforward decoupling control algorithm enables the independent regulation of active and reactive power within the inner-loop current of

a three-phase grid-connected inverter. Figure III.5 illustrates the diagram of the current controller in the inner loop.

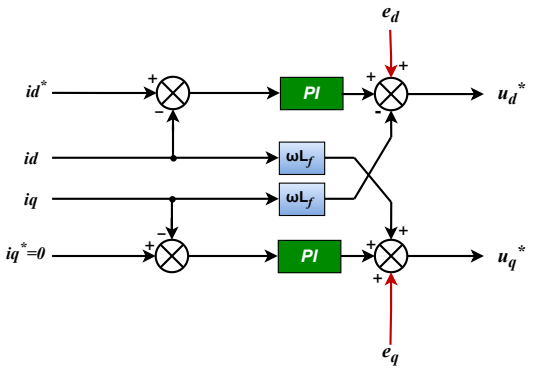


Figure III.5: Diagram of the current controller in the inner loop

Based on the principles of instantaneous power theory, the active power P and reactive power Q within the synchronous rotating dq-reference frame are defined as follows:

$$\begin{cases} P = \frac{3}{2}\left(u_d i_d + u_q i_q\right) \\ Q = \frac{3}{2}\left(u_d i_q - u_q i_d\right) \end{cases} \tag{III.10}$$

When the $d$-axis is aligned with the synthesized grid voltage vector, such that $u_q = 0$, Equation III.10 can be reformulated as follows:

$$\begin{cases} P = \frac{3}{2} u_d i_d \\ Q = \frac{3}{2} u_d i_q \end{cases} \tag{III.11}$$

The inverter control strategy is defined through the application of equations III.7 and III.8. Using these equations, the overall block diagram for current regulation in a grid-connected VSI within the SRF is derived, as illustrated in Figure III.6. Here, $i_d^*$ and $i_q^*$ represent the reference currents along the d and q axes, respectively. The PLL provides the essential phase details of the grid voltage, enabling the abc-dq transformation process.

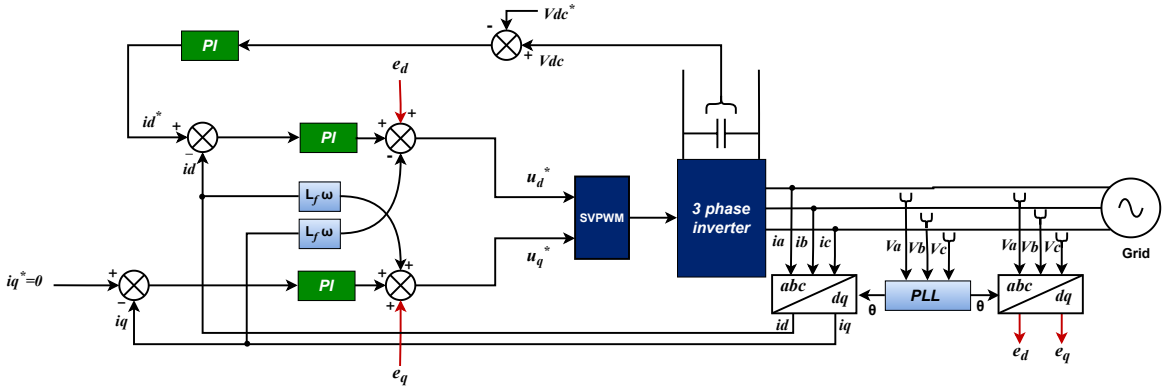


Figure III.6: General block diagram of VSI current control in SRF

### III.2.3 Phase-Locked Loops (PLL)

The PLL system typically comprises three key components: the Phase Detector (PD), the Loop Filter (LF), and the Voltage-Controlled Oscillator (VCO), as depicted in Figure III.7. The PD detects the phase error $e(t)$ between the input signal $i(t)$ and the output signal $o(t)$. This error signal is then passed to the LF for further processing. The VCO adjusts the output signal frequency based on the error signal [63].


Figure III.7: Diagram of PLL Block

The grid voltages are represented as:

$$\begin{cases} vs_a = V_m \cos(\theta) \\ vs_b = V_m \cos(\theta - 2\pi/3) \\ vs_c = V_m \cos(\theta + 2\pi/3) \end{cases} \tag{III.12}$$

where $V_m$ represents the amplitude and $\theta$ denotes the phase angle.

The three-phase grid voltages are converted into a stationary reference frame $\alpha - \beta$ through the application of Clarke transformation, as expressed by the following equation.

$$\begin{bmatrix} vs_\alpha \\ vs_\beta \end{bmatrix} = \frac{2}{3} \cdot \begin{bmatrix} 1 & -1/2 & -1/2 \\ 0 & \sqrt{3}/2 & -\sqrt{3}/2 \end{bmatrix} \cdot \begin{bmatrix} vs_a \\ vs_b \\ vs_c \end{bmatrix} \tag{III.13}$$

The expression for the grid voltage in the synchronous d-q frame is as follows:

$$\begin{bmatrix} vs_d \\ vs_q \end{bmatrix} = \begin{bmatrix} \sin(\theta') & -\cos(\theta') \\ \cos(\theta') & \sin(\theta') \end{bmatrix} \cdot \begin{bmatrix} vs_\alpha \\ vs_\beta \end{bmatrix} \tag{III.14}$$

$\theta'$ denotes the estimated phase angle.

Hence,

$$\begin{cases} vs_d = V_m \cdot \cos(\theta - \theta') \\ vs_q = V_m \cdot \sin(\theta - \theta') \end{cases} \tag{III.15}$$

As the estimated phase angle converges towards the actual phase angle of the grid voltages, the grid voltages in the d-q SRF are expressed as:

$$\begin{cases} vs_d = V_m \\ vs_q = 0 \end{cases} \tag{III.16}$$

Accurate phase angle estimation is achieved by minimizing the error between the estimated and actual phase angles using a PI regulator [63]. The structure of the implemented PLL is shown in Figure III.8.

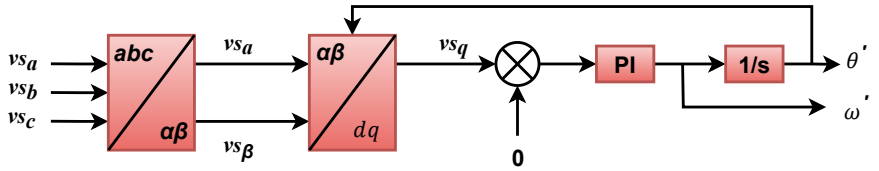


Figure III.8: Diagram of dq-PLL Block

### III.2.4 DC-link voltage regulation

DC-link voltage regulation ensures stability and efficiency in power systems by minimizing fluctuations, improving reliability, and balancing energy flow using methods such

as PI controllers.

The DC voltage dynamics equation is expressed as follows:

$$v_{dc} = \frac{1}{C_{dc}} \int I_{dc} dt \tag{III.17}$$

With:

$I_{dc}$: Current flowing through the capacitor [A].

$v_{dc}$: Voltage across the capacitor terminals [V].

By applying the Laplace transform, we get the following:

$$v_{dc} = \frac{1}{s.C_{dc}} I_{dc} \tag{III.18}$$

As shown in Figure III.9, the closed-loop transfer function can be expressed as follows:

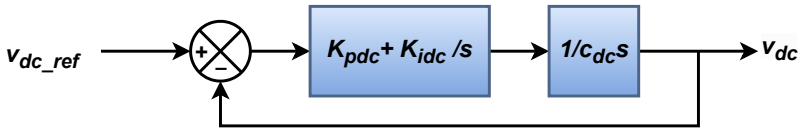


Figure III.9: DC-link voltage control loop

$$G_{vdc} = \frac{\left(1 + \frac{K_{\mathrm{p}}}{K_{\mathrm{t}}} s\right) \omega_c^2}{s^2 + 2\xi\omega_c s + \omega_c^2} \tag{III.19}$$

Estimation of the PI controller parameters can be formulated as follows [92]:

$$\begin{cases} K_{idc} = \omega_c^2 C_{dc} \\ K_{pdc} = 2\xi\sqrt{K_{idc} C_{dc}} \end{cases} \tag{III.20}$$

### III.2.4.1 Selection of DC link voltage

The DC link voltage is determined based on the target AC output voltage requirements and the chosen modulation technique. In the case of space vector pulse with modulation (SVPWM) systems, the relationship is defined as follows [93]:

$$V_{dc} = \frac{V_{L-L(rms)}}{1.15 \times 0.612 \times m_a} \tag{III.21}$$

Where

$V_L - L(rms)$:Line-to-Line RMS Voltage.

$V_{dc}$: The value of the fixed DC link voltage the system requires.

$m_a$:is the ratio of the amplitude of the reference signal to the amplitude of the carrier signal in pulse width modulation (PWM) systems, which ranges between 0 and 1.

1.15 and 0.612 are the correction factors in the SVPWM system and the conversion value between the peak line-to-line voltage and the RMS, respectively.

### III.2.5 Presentation of SVPWM

SVPWM enhances voltage source inverter performance by optimizing the usage of the DC bus, reducing harmonics, and minimizing losses. It synthesizes voltage vectors in the $\alpha$-$\beta$ frame [94], and as illustrated in Figure III.10, two-level switching states of the inverter are shown.

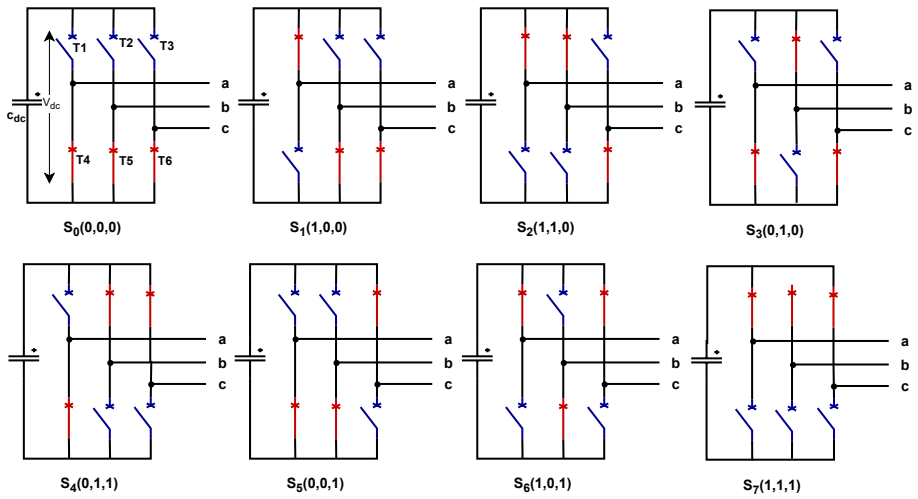


Figure III.10: Configurations of VSI switching states

Where (Sa, Sb, and Sc) are control signals that have the following conditions:

$$S_a = \begin{cases} 1 & \text{if } T_1 \text{ ON then } T_4 \text{ OFF,} \\ 0 & \text{if } T_1 \text{ OFF then } T_4 \text{ ON.} \end{cases} \tag{III.22}$$

$$S_b = \begin{cases} 1 & \text{if } T_2 \text{ ON then } T_5 \text{ OFF,} \\ 0 & \text{if } T_2 \text{ OFF then } T_5 \text{ ON.} \end{cases} \tag{III.23}$$

$$S_c = \begin{cases} 1 & \text{if } T_3 \text{ ON then } T_6 \text{ OFF,} \\ 0 & \text{if } T_3 \text{ OFF then } T_6 \text{ ON.} \end{cases} \tag{III.24}$$

The following equations express the output voltage of the inverter between phases:

$$\begin{cases} v_{ab} = \mathrm{v_{dc}}\,(S_a - S_b) \\ v_{bc} = \mathrm{v_{dc}}\,(S_b - S_c) \\ v_{ca} = \mathrm{v_{dc}}\,(S_c - S_a) \end{cases} \tag{III.25}$$

The equations for simple output voltages can be expressed as follows [63]:

$$\begin{cases} v_a = v_{dc}.(\frac{2}{3}S_a - \frac{1}{3}S_b - \frac{1}{3}S_c) \\ v_b = v_{dc}.(\frac{2}{3}S_b - \frac{1}{3}S_a - \frac{1}{3}S_c) \\ v_c = v_{dc}.(\frac{2}{3}S_c - \frac{1}{3}S_a - \frac{1}{3}S_b) \end{cases} \tag{III.26}$$

The possible cases of the output voltages are summarized in Table III.1 [95].

| **State** | $S_a$ | $S_b$ | $S_c$ | $v_a$ | $v_b$ | $v_c$ |
|---|---|---|---|---|---|---|
| 0 | 0 | 0 | 0 | 0 | 0 | 0 |
| 1 | 1 | 0 | 0 | $2v_{dc}/3$ | $-v_{dc}/3$ | $-v_{dc}/3$ |
| 2 | 1 | 1 | 0 | $v_{dc}/3$ | $v_{dc}/3$ | $-2v_{dc}/3$ |
| 3 | 0 | 1 | 0 | $-v_{dc}/3$ | $2v_{dc}/3$ | $-v_{dc}/3$ |
| 4 | 0 | 1 | 1 | $-2v_{dc}/3$ | $v_{dc}/3$ | $v_{dc}/3$ |
| 5 | 0 | 0 | 1 | $-v_{dc}/3$ | $-v_{dc}/3$ | $2v_{dc}/3$ |
| 6 | 1 | 0 | 1 | $v_{dc}/3$ | $-2v_{dc}/3$ | $v_{dc}/3$ |
| 7 | 1 | 1 | 1 | 0 | 0 | 0 |

Table III.1: Switch states for three-phase two-level VSI

As shown in Figure III.11, the three-phase voltage inverter generates eight states, including six active and two inactive states. In a plane with the d-axis as the horizontal axis and the q-axis as the vertical axis, these states form a hexagon depicted in Figure III.11. This hexagon is divided into six sectors, each consisting of a triangle whose vertices correspond to the null state (0 or 7) and two consecutive active states, such as (1 2), (2 3)... (6 1). Specific vectors bound these sectors [96].

The objective of SVPWM is to approximate the reference voltage $V_{ref}$ using the eight available state vectors. To achieve this, a straightforward approximation method is employed: it generates an average inverter output over a small period T, which is equivalent to the reference voltage $V_{ref}$ during that interval. Thus, vector pulse-width modulation can be implemented by following these steps; for more details, see [96]:

- Identify the Sector of Operation.
- Calculate the duty cycles.
- Determine the switch sequence.

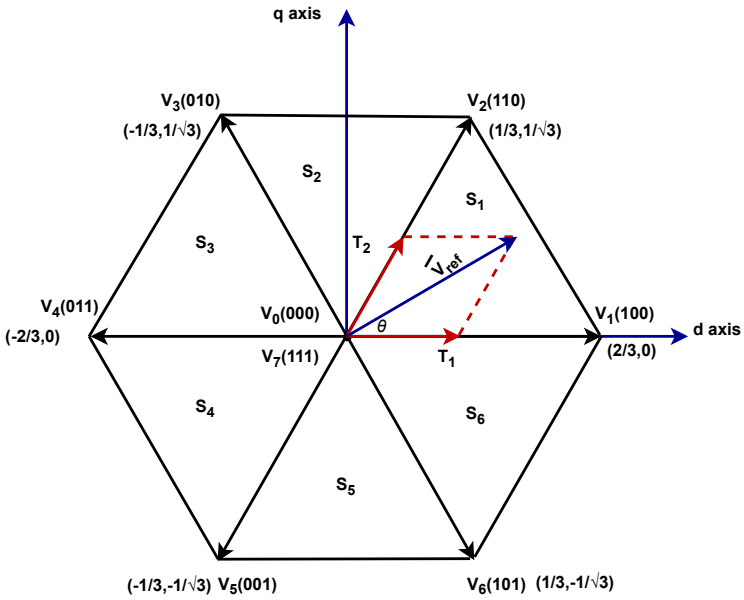


Figure III.11: Possible switching states and sectors

### III.2.6 Techniques of MPPT

The strategies of MPPT have a crucial role in maximizing the output energy of PV systems through dynamically adjusting the operating point to align with changing environmental factors, such as irradiance and temperature. The basic principle behind MPPT is to continuously adjust the system's operating voltage and current to achieve the highest possible power output. Traditional MPPT methods include techniques such as perturbation and observation (P&O) and incremental conduction (IC), both of which are widely used due to their simplicity and ease of implementation.

However, these methods may struggle with accuracy under rapidly changing conditions. Advanced MPPT strategies, such as those based on metaheuristic algorithms such as PSO, GWO, and controllers such as fuzzy logic control (FLC), artificial neural networks (ANN), have emerged to address these limitations [55, 97].

These techniques provide faster and more accurate tracking by predicting optimal performance, making them particularly effective in environments with dynamic weather patterns or complex system configurations.In this section, we will present the proposed Dandelion Optimization (DO) method, while the P&O, PSO, and GWO methods are detailed in (Appendix A).

#### III.2.6.1 Description of the dandelion plant

The DO algorithm is a nature-inspired algorithm inspired by the dispersal behavior of the dandelion plant, Herba taraxacaci, a perennial herbaceous species of the Asteraceae family. It grows up to 20 cm in height. This plant is characterized by its unique seed structure, which consists of a seed body, a thin beak, and a tuft of fine hairs, and it exhibits an effective natural mechanism for seed dispersal.

Its seeds are carried by the wind for varying distances, and their spread is primarily influenced by wind speed and environmental conditions. This biological process is mathematically modeled in the DO algorithm, where the seed distribution and colonization behavior guide the search for optimal solutions. As such, the algorithm leverages the wind-driven dispersal and adaptability of dandelion seeds to efficiently explore and exploit the solution

space [3, 98]. Figure III.12 depicts the dandelion floating in the wind.

Figure III.12: The dandelion floating in the wind

The dandelion plant reproduces to transmit seeds to the succeeding generation according to a strategy based on the following three main stages:

1. **Rising stage:** During this stage, dandelion seeds ascend, influenced by factors to wind speed and humidity. This stage is defined by its simulation under diverse environmental conditions, as detailed as follows:

   - **The case of a clear day:** The wind speeds take a normal distribution ($\ln y$), which makes the random numbers spread more widely along the Y-axis, and this increases the probability of dandelion seeds moving to more distant areas. Due to the change in wind speed, the vortices above the dandelion seeds adapt to allow the seeds to flow upward in a spiral [3,98]. This behavior can be expressed mathematically through the following equation:

$$d_{t+1} = d_t + c \times u_x \times u_y \times \ln y \times (d_s - d_t) \tag{III.27}$$

   where $d_t$ and $d_{t+1}$ represent the positions of the dandelion seed at the current and subsequent iterations, respectively. The parameter $c$ denotes the step size, $\ln y$ corresponds to a log-normal distribution, and $d_s$ indicates the random initial

position. The terms $u_x$ and $u_y$ are lift coefficients that influence the seed's movement along the $x$ and $y$ axes, respectively.

The mathematical formula for the random location is given as follows:

$$d_s = r \cdot (d_{\max} - d_{\min}) + d_{\min} \tag{III.28}$$

where r is a random number between [0,1].

$\ln(y)$ is the natural logarithmic distribution with mean $\mu = 0$ and variance $\sigma^2 = 1$, and is given by the following mathematical formula:

$$\ln y = \begin{cases} \frac{1}{y\sqrt{2\pi}} \exp\left[-\frac{1}{2\sigma^2}(\ln y)^2\right] & y \geq 0 \\ 0 & y < 0 \end{cases} \tag{III.29}$$

where the variable $y$ refers to the standard normal distribution $N(0,1)$, and $C$ is a parameter that guides the algorithm to initiate with a global search and subsequently transition to a local search, thereby achieving accurate convergence. This behavior is expressed mathematically as:

$$C = \text{rand} \times \left(\frac{t}{T_{\max}} - 1\right)^2 \tag{III.30}$$

The coefficients $u_x$ and $u_y$ on the variable dimension are calculated as follows:

$$\begin{cases} r = \frac{1}{e^{\theta}} \\ u_x = r \times \cos\theta \\ u_y = r \times \sin\theta \end{cases} \tag{III.31}$$

where, $\theta$ is a random number between [-$\pi$,$\pi$].

- **The case of a rainy day:** The dispersal behavior of dandelion seeds is influenced by increased humidity and air resistance. Under such conditions, the seeds tend to ascend slowly with the wind while exhibiting a tendency to remain within local regions, enhancing their chances of survival [3]. The equation expresses this behavior mathematically as follows:

$$d_{t+1} = d_t \times K \tag{III.32}$$

The parameter K defines the local search range for dandelions and is calculated using the following formula:

$$K = 1 - \text{rand} \times q \tag{III.33}$$

With q is given by the following formula:

$$q = \frac{1}{T^2 - 2T + 1} t^2 - \frac{2}{T^2 - 2T + 1} t + 1 + \frac{1}{T^2 - 2T + 1} \tag{III.34}$$

The rising stage of dandelion seeds can be summarized by the following mathematical formula:

$$d_{t+1} = \begin{cases} d_t + c \times u_x \times u_y \times \ln y \times (d_s - d_t) & \text{randn } < 1.5 \\ d_t \times K & \text{else} \end{cases} \tag{III.35}$$

The algorithm dynamically balances exploration and exploitation by utilizing random values sampled from a normal distribution. Additionally, setting a cut-off threshold at 1.5 enhances its inclination toward global exploration, thereby improving its ability to search broadly across the solution area.

2. **Declining stage:** In this stage, the algorithm emphasizes exploration, where dandelion seeds progressively migrate over a defined distance by repeatedly updating their positions across all individuals, thereby covering a broader search space. During each update, individuals retain a normal distribution pattern, and seed movement follows a Brownian motion dynamic [3, 98]. The following equation can mathematically represent this behavior:

$$d_{t+1} = d_t - c \cdot B_t \cdot (d_{\text{avg},\,t} - (B_t \cdot c \cdot d_t)) \tag{III.36}$$

where $B_t$ represents Brownian motion based on a normal distribution, while $d_{\text{avg},\,t}$ denotes the average seed position during the $t^{\text{th}}$ iteration and is calculated by the following equation:

$$D_{\text{avg,t}} = \frac{1}{pop} \sum_{i=1}^{\text{pop}} D_i \tag{III.37}$$

3. **Landing stage:** In this stage, the focus is on exploitation, where dandelion seeds choose a random landing site with the potential to reach global convergence. Here, the optimal location is the one that gives dandelion seeds the better opportunity to survive. Relying on the search information gained from the present elite, the seeds tend to converge on the global optimum in the total search area [98]. This behavior is expressed mathematically by the following equation:

$$d_{t+1} = d_{\text{elite}} + \text{Levy}(\lambda) \cdot c \cdot (d_{\text{elite}} - d_t \cdot \delta) \tag{III.38}$$

where $d_{\text{elite}}$ denotes the optimal location of the dandelion seed in the $t^{\text{th}}$ iteration, Levy($\lambda$) represents the Levy flight function, and $\delta$ is a linearly increasing function within the range $[0, 2]$, calculated using the following equation:

$$\delta = \frac{2t}{T_{\max}} \tag{III.39}$$

The Levy flight is mathematically expressed as follows:

$$\text{Levy}(\lambda) = s \cdot \left( \frac{w \cdot \rho}{|N|^{1/\beta}} \right) \tag{III.40}$$

where $\beta$ represents a random value in the range [0, 2], typically set to 1.5, $s$ is set to 0.01, and $w$ and N are random numbers uniformly distributed in $[0, 1]$. The parameter $\rho$ is calculated using the following formula:

$$\rho = \left( \frac{\Gamma(1+\beta) \times \sin\left(\frac{\pi\beta}{2}\right)}{\Gamma\left(\frac{1+\beta}{2}\right) \times \beta \times 2^{\left(\frac{\beta-1}{2}\right)}} \right) \tag{III.41}$$

Figure III.13 (a) depicts the movement behavior of dandelion seeds under varying climatic conditions. During clear weather, the seeds initiate an exploratory phase by updating positional data within randomly selected regions. Their motion is influenced by the presence of vortices above, which alter the direction of movement through rotational vectors modulated by the lift coefficients $u_x$ and $u_y$. In contrast, rainy conditions promote a more exploitative behavior, wherein the surrounding neighborhood is intensively searched in all directions to facilitate localized seed dispersal. Figure III.13 (b) illustrates the regeneration process of dandelion seeds as they descend, highlighting the global exploratory trajectory influenced by Brownian motion. This irregular and stochastic migration pattern allows the population to investigate regions in proximity to the global optimum, thereby improving the algorithm's ability to avoid premature convergence to local optima. As shown in Figure III.13 (c), the search intensity is progressively refined as the algorithm converges toward the global optimum. To mitigate excessive exploitation, individuals are directed using a linearly increasing control function, while a Levy flight mechanism is employed to regulate the magnitude of step sizes in subsequent movements.

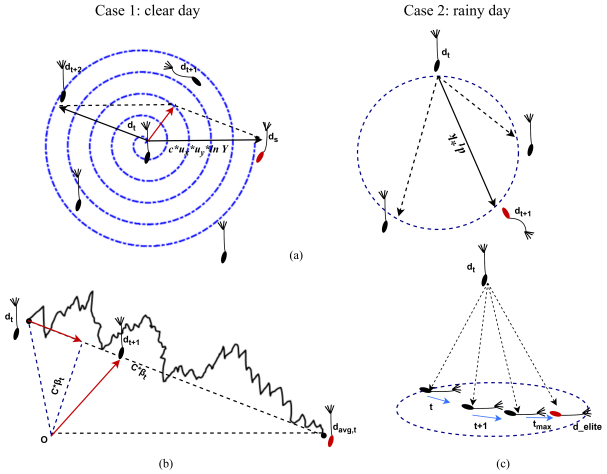


Figure III.13: Sequential stages of dandelion seed motion modeled for global optimal solution: (a) rising phase, (b) descending phase, and (c) landing phase

#### III.2.6.2 Adaptation of the DO algorithm for MPPT

To ensure a precise and stable operation in PV systems, the implementation of the DO algorithm for MPPT requires the incorporation of specific operational constraints and control adaptations. A fundamental aspect of this algorithm involves the manipulation of duty ratios, which serve as the primary control inputs for the power converter. Analogous to the dispersal of dandelion seeds, these duty ratios must be confined within clearly defined operational boundaries specifically, a minimum value $d_{\min} = 0.1$ and a maximum value $d_{\max} = 0.9$.

Enforcing these bounds ensures that the optimization process remains within a safe and functionally viable region, thereby avoiding instability and preventing violations of the converter's permissible operating conditions. This contributes significantly to the overall reliability and efficiency of power conversion within the PV system.

The DO algorithm advances through a structured sequence of three distinct phases: an initial exploration phase (rising), a focused exploitation phase (descending), and a convergence phase (landing). During the rising phase, the algorithm initiates a broad exploration by generating random trajectories for the duty ratios, enabling a wide-ranging search of the solution space.

In the descending phase, search intensification is achieved using principles derived from Brownian motion, directing computational effort toward areas with promising performance indicators.

Finally, in the landing phase, the search is refined using a linearly increasing function in conjunction with Levy flight dynamics, facilitating convergence toward the global maximum power point (GMPP) with improved precision.

Throughout this iterative process, duty ratios are continuously updated and refined until convergence criteria are satisfied. Upon identifying the optimal duty ratio, it is applied to the power converter, thereby enabling the PV system to operate at its MPP. The detailed flowchart of the DO-based MPPT method is illustrated in Figure III.14.

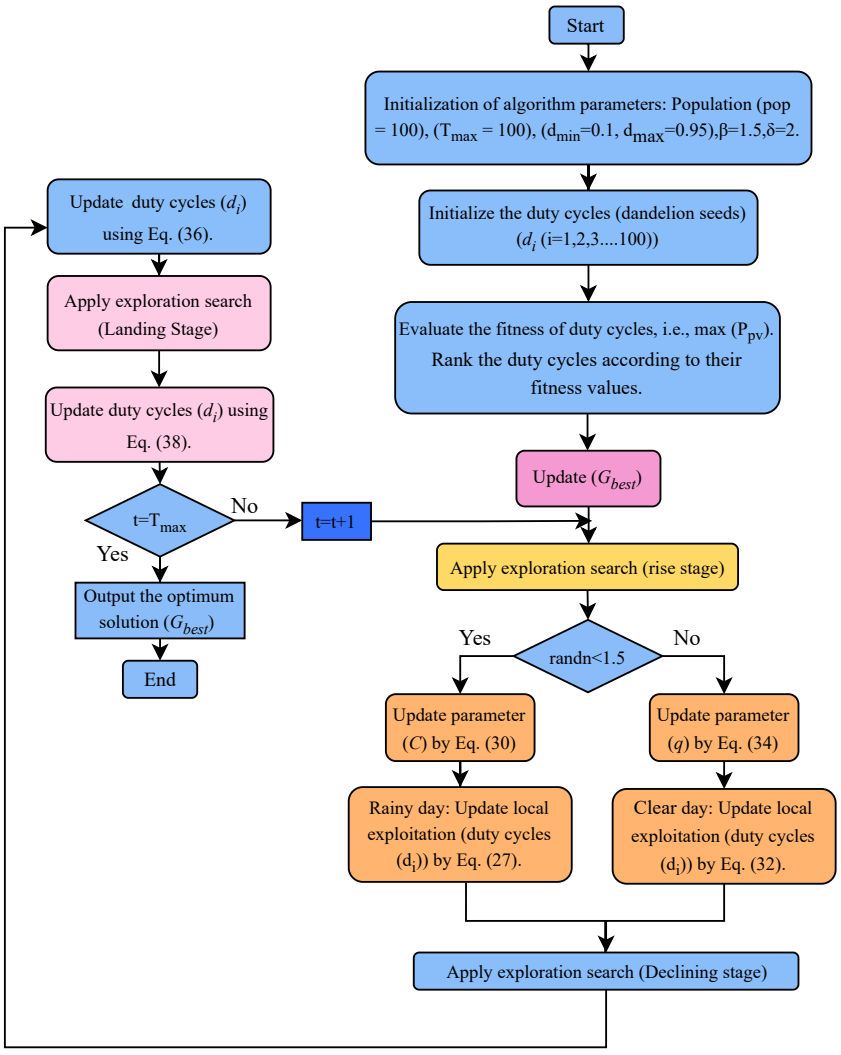


Figure III.14: Flowchart of the proposed MPPT based on the DO algorithm

### III.2.7 Look-up table techniques

A wind turbine model based on lookup tables is a highly effective method to simulate turbine performance under varying operating conditions. This approach relies on precomputed data for parameters such as the power coefficient, torque coefficient, and aerodynamic properties, all of which are functions of the tip-speed ratio and the angle of rotation of the blade [99]. The utilization of multidimensional lookup tables enables the model to expedite the calculation of aerodynamic torque and power for designated wind and rotor speeds, thereby substantially diminishing the computational demands when contrasted with real-time aerodynamic calculations [100]. This efficiency renders it particularly advantageous

for control system development and dynamic analyses. Furthermore, the utilization of preprogrammed two-dimensional tables, which store optimal generator speeds and their corresponding maximum power or torque values at varying wind speeds, or the employment of cubic mapping functions to derive reference signals for optimal power or torque, are additional features of MPPT techniques based on lookup tables. Combining these techniques ensures adaptability to diverse turbine designs and efficient tracking of maximum power points, dependent on the availability of precise and comprehensive data [101]. As demonstrated in figure III.15, the wind speed and the rotational speed are employed as input, with the mechanical torque serving as the output.

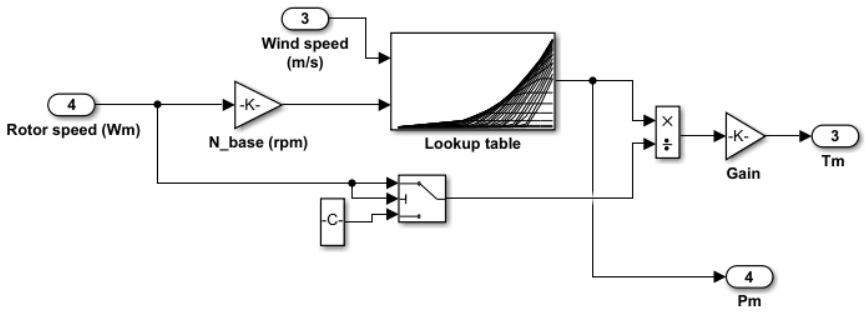


Figure III.15: Simulink model of the studied wind turbine

### III.2.7.1 Tip Speed Ratio method

The tip speed ratio (TSR) control method is designed to regulate the rotor speed, ensuring the TSR remains at its optimal value. Achieving this requires the precise measurement of both the wind speed and the turbine's rotational speed. The optimal TSR, specific to each wind turbine system, is determined based on the turbine-generator characteristics and varies across different configurations.

According to equations III.42 and III.43, maintaining the optimal rotational speed $\lambda_{opt}$ of the wind turbine rotor for a given wind speed allows the system to achieve maximum turbine efficiency, thus maximizing mechanical power output [102].

The TSR control method achieves this by adjusting the generator's rotational speed to sustain the TSR at its optimal point, where power extraction is at its peak. Despite

being straightforward in its implementation, this approach necessitates accurate real-time measurement or estimation of both wind speed and turbine speed. However, measuring wind speed directly at the turbine rotor poses challenges in practice, particularly in small-scale systems, as it adds complexity and increases costs [103]. Additionally, the method requires knowledge of the turbine's optimal TSR, which may vary with changes in the turbine's parameters. A block diagram illustrating a PMSG Wind Energy Conversion System (WECS) utilizing TSR control is provided in figure III.16.

To maximize the efficiency of mechanical transmission in a wind turbine, the optimal angular speed, $\Omega_{m,opt}$, is determined as follows:

$$\Omega_{m,opt} = \frac{\lambda_{opt} v}{R} \tag{III.42}$$

The maximum power of a wind turbine at different speeds is as follows:

$$P_{\max} = \Omega_{m,opt} T_{opt} \tag{III.43}$$

Where $\lambda_{opt}$ is the optimal tip speed ratio , R is the radius of a turbine, v is the wind speed, and $T_{opt}$ is optimal torque.

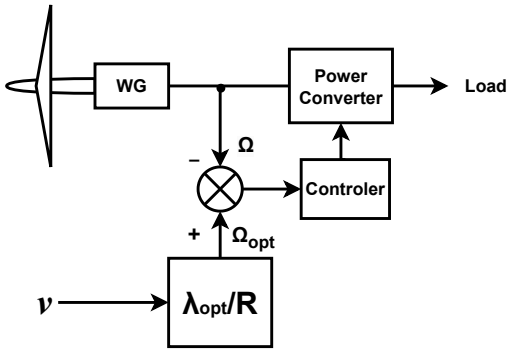


Figure III.16: TSR control system.

### III.2.7.2 Optimal Torque Control

In the OTC approach, variations in wind speed are managed by continuously regulating the generator torque to maintain operation at the optimal point, as defined by Eq III.44.

$$T_{opt} = K_{opt}\Omega_{opt}^2 \tag{III.44}$$

And

$$K_{opt} = \frac{1}{2}\pi\rho\frac{R^5}{\lambda_{\text{opt}}^3}C_{p,\max} \tag{III.45}$$

The block diagram of the OTC MPPT strategy is illustrated in Fig III.17. This method involves measuring the rotor speed of the generator and calculating the optimal torque $T_{opt}$, which corresponds to the torque that maximizes the turbine's power output. The calculated optimal torque serves as the reference torque for the vector control strategy applied to the PMSG [97].

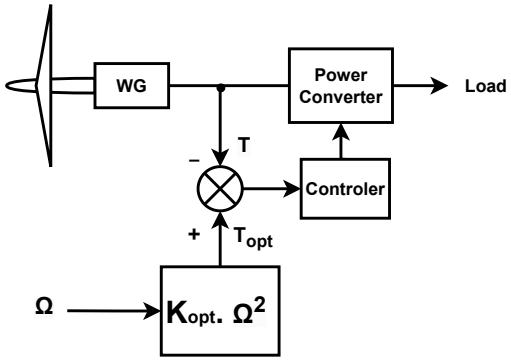


Figure III.17: OTC control system.

### III.2.7.3 Power Signal Feedback Control

The PSF control method requires prior knowledge of the wind turbine's maximum power curve, which is tracked through its control mechanisms. These maximum power curves are typically derived from simulations, off-line experiments conducted on individual wind turbines, or from the turbine's datasheet, posing challenges to achieving precise implementation in practical scenarios [102]. In this approach, the reference power is determined either from a predefined maximum power data curve or by employing the turbine's mechanical power equation, where wind speed or rotational speed serves as input. Figure III.18 depicts the block diagram of the PSF control for maximum power extraction. The

PSF control block generates the optimal power command $Popt$, which is subsequently used in the grid-side converter control system to extract maximum power. Using Eq III.43, this process can involve measuring the generator's rotor speed $\omega$ to define the reference turbine power $P_t$ [104].

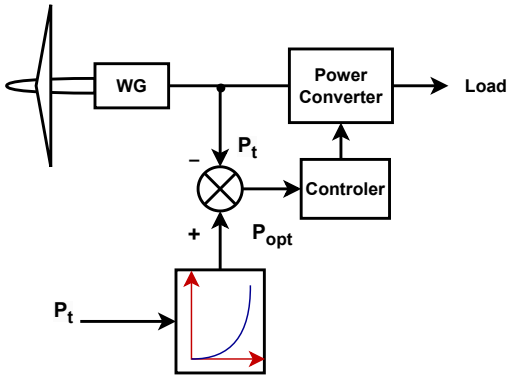


Figure III.18: PSF control system.

## III.3 Control of VSC-HVDC system

The philosophy of control in Voltage Source Converters (VSCs) focuses on generating an alternating current (AC) voltage from a direct current (DC) source, emphasizing simultaneous regulation of both phase and amplitude. A stable VSC-HVDC link requires precise control of the DC voltage to balance active power delivery and absorption between converter stations, accounting for system losses. Control strategies may include maintaining constant power, modulating power based on frequency, or maximizing available AC network output, particularly in renewable applications. Active power is managed by adjusting the phase angle ($\delta$) relative to the AC network voltage, while reactive power control is achieved via modulation index adjustments, as Figure III.19 shows. can choose between reactive power regulation and AC voltage regulation for each end of the VSC-HVDC link. A cascade control system facilitates this by employing an inner current loop and various external regulators to ensure efficient operation across different applications. Each regulator's selection depends on specific operational requirements, highlighting the complexity of VSC control in modern power systems.

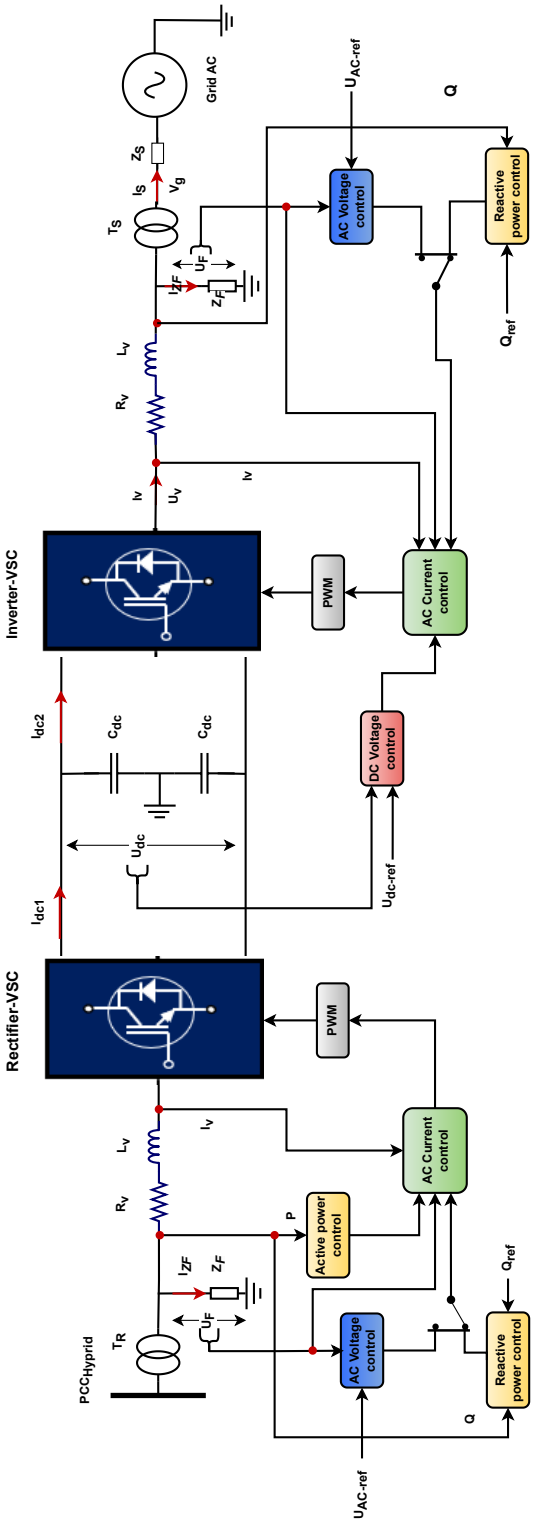


Figure III.19: Control diagram of a VSC-HVDC link

### III.3.1 AC control

Implementing AC control is essential to prevent overloading of the converter valves. This control may be achieved either directly or through vector control, where current management serves as an intermediate process for regulating parameters like active and reactive power. The AC control loop operates within the dq reference frame, utilizing model equations to ensure precision. A comprehensive understanding of the control system is based on these model equations, as shown in Figure III.19. Here, the secondary voltages from the transformer and the converter currents are separated into two balanced systems: one with a positive sequence (p) and the other with a negative sequence (n).

The equation for the voltages the secondary transformer delivers to the converter is given by:

$$\begin{cases} u_{La} = u_{Lap} + u_{Lan} \\ u_{Lb} = u_{Lbp} + u_{Lbn} \\ u_{Lc} = u_{Lcp} + u_{Lcn} \end{cases} \tag{III.46}$$

And for currents:

$$\begin{cases} i_{va} = i_{vap} + i_{van} \\ i_{vb} = i_{vbp} + i_{vbn} \\ i_{vc} = i_{vcp} + i_{vcn} \end{cases} \tag{III.47}$$

When the system is operating in a balanced state, then, $i_{\text{van}}$ , $i_{\text{vbn}}$ , $i_{\text{vcn}}$ , $u_{\text{Lan}}$ , $u_{Lbn}, u_{Lcn}$, are zero.

For each phase:

$$u_v - u_L = L_v \frac{di_v}{dt} + R_v i_v \tag{III.48}$$

In an unbalanced system, the voltage drop across the reactance terminals can be expressed in terms of both voltage and current's positive and negative sequence components [74]. The positive sequence voltages across the reactance, represented as $(R_v + j\omega L_v)$, are represented by the following differential equation:

$$\begin{aligned}\frac{d}{dt}\begin{bmatrix} i_{vap} \\ i_{vbp} \\ i_{vcp} \end{bmatrix} &= \begin{bmatrix} -\frac{R_v}{L_v} & 0 & 0 \\ 0 & -\frac{R_v}{L_v} & 0 \\ 0 & 0 & -\frac{R_v}{L_v} \end{bmatrix} \begin{bmatrix} i_{vap} \\ i_{vbp} \\ i_{vcp} \end{bmatrix} \\ &+ \begin{bmatrix} \frac{1}{L_v} & 0 & 0 \\ 0 & \frac{1}{L_v} & 0 \\ 0 & 0 & \frac{1}{L_v} \end{bmatrix} \begin{bmatrix} u_{vap} \\ u_{vbp} \\ u_{vcp} \end{bmatrix} - \begin{bmatrix} \frac{1}{L_v} & 0 & 0 \\ 0 & \frac{1}{L_v} & 0 \\ 0 & 0 & \frac{1}{L_v} \end{bmatrix} \begin{bmatrix} u_{Lap} \\ u_{Lbp} \\ u_{Lcp} \end{bmatrix}\end{aligned} \tag{III.49}$$

for the negative sequence voltage given by:

$$\begin{aligned}\frac{d}{dt}\begin{bmatrix} i_{van} \\ i_{vbn} \\ i_{vcn} \end{bmatrix} &= \begin{bmatrix} -\frac{R_v}{L_v} & 0 & 0 \\ 0 & -\frac{R_v}{L_v} & 0 \\ 0 & 0 & -\frac{R_v}{L_v} \end{bmatrix} \begin{bmatrix} i_{van} \\ i_{vbn} \\ i_{vcn} \end{bmatrix} \\ &+ \begin{bmatrix} \frac{1}{L_v} & 0 & 0 \\ 0 & \frac{1}{L_v} & 0 \\ 0 & 0 & \frac{1}{L_v} \end{bmatrix} \begin{bmatrix} u_{van} \\ u_{vbn} \\ u_{vcn} \end{bmatrix} - \begin{bmatrix} \frac{1}{L_v} & 0 & 0 \\ 0 & \frac{1}{L_v} & 0 \\ 0 & 0 & \frac{1}{L_v} \end{bmatrix} \begin{bmatrix} u_{Lan} \\ u_{Lbn} \\ u_{Lcn} \end{bmatrix}\end{aligned} \tag{III.50}$$

The equations III.49 and III.50 for voltages and currents are given when transformed to the $(\alpha, \beta)$ frame as follows:

$$\begin{aligned}\frac{d}{dt}\begin{bmatrix} i_{v\alpha p} \\ i_{v\beta p} \end{bmatrix} &= \begin{bmatrix} -\frac{R_v}{L_v} & 0 \\ 0 & -\frac{R_v}{L_v} \end{bmatrix} \begin{bmatrix} i_{v\alpha p} \\ i_{v\beta p} \end{bmatrix} + \begin{bmatrix} \frac{1}{L_v} & 0 \\ 0 & \frac{1}{L_v} \end{bmatrix} \begin{bmatrix} u_{v\alpha p} \\ u_{v\beta p} \end{bmatrix} \\ &- \begin{bmatrix} \frac{1}{L_v} & 0 \\ 0 & \frac{1}{L_v} \end{bmatrix} \begin{bmatrix} u_{L\alpha p} \\ u_{L\beta p} \end{bmatrix}\end{aligned} \tag{III.51}$$

And

$$\begin{aligned}\frac{d}{dt}\begin{bmatrix} i_{v\alpha n} \\ i_{v\beta n} \end{bmatrix} &= \begin{bmatrix} -\frac{R_v}{L_v} & 0 \\ 0 & -\frac{R_v}{L_v} \end{bmatrix} \begin{bmatrix} i_{v\alpha n} \\ i_{v\beta n} \end{bmatrix} + \begin{bmatrix} \frac{1}{L_v} & 0 \\ 0 & \frac{1}{L_v} \end{bmatrix} \begin{bmatrix} u_{v\alpha n} \\ u_{v\beta n} \end{bmatrix} \\ &- \begin{bmatrix} \frac{1}{L_v} & 0 \\ 0 & \frac{1}{L_v} \end{bmatrix} \begin{bmatrix} u_{L\alpha n} \\ u_{L\beta n} \end{bmatrix}\end{aligned} \tag{III.52}$$

Assuming the system is in balance ($x_a + x_b + x_c = 0$), the transformed in the $(\alpha, \beta)$ frame is given by the following equation:

$$\bar{x}_{\alpha\beta} = x_\alpha + jx_\beta = \sqrt{\frac{2}{3}}\left[x_a + x_b e^{j\frac{2\pi}{3}} + x_c e^{j\frac{4\pi}{3}}\right] \tag{III.53}$$

The transformed in $(\alpha, \beta)$ frame can be written as follows:

$$\begin{bmatrix} x_\alpha \\ x_\beta \end{bmatrix} = \begin{bmatrix} \sqrt{\frac{2}{3}} & -\sqrt{\frac{1}{6}} & -\sqrt{\frac{1}{6}} \\ 0 & \sqrt{\frac{1}{2}} & -\sqrt{\frac{1}{2}} \end{bmatrix} \begin{bmatrix} x_a \\ x_b \\ x_c \end{bmatrix} \tag{III.54}$$

And for the inverse transformation :

$$\begin{bmatrix} x_a \\ x_b \\ x_c \end{bmatrix} = \begin{bmatrix} \sqrt{\frac{2}{3}} & 0 \\ -\sqrt{\frac{1}{6}} & \sqrt{\frac{1}{2}} \\ -\sqrt{\frac{1}{6}} & -\sqrt{\frac{1}{2}} \end{bmatrix} \begin{bmatrix} x_\alpha \\ x_\beta \end{bmatrix} \tag{III.55}$$

The process of converting three-phase system variables, such as voltages and currents, into symmetrical components is typically performed in the complex plane. However, this approach is less efficient for time-domain signals, as it relies on applying both a digital Fourier transform (DFT) and its inverse. Several time-domain algorithms have been developed that offer improved efficiency to address this limitation. The approach utilized in this thesis is depicted in Figure III.20 Here, the ($\alpha$, $\beta$) transformation remains identical for both positive and negative sequences, making a single transformation adequate [105].

Figure III.20 shows the schematic used to calculate the positive and negative sequences of the dq components.

$$\begin{cases} x_{\alpha n}(k) = \frac{1}{2}\left[x_\alpha(k) + x_\beta\left(k - \frac{1}{4}\frac{T}{T_S}\right)\right] \\ x_{\beta n}(k) = \frac{1}{2}\left[x_\beta(k) + x_\alpha\left(k - \frac{1}{4}\frac{T}{T_S}\right)\right] \end{cases} \tag{III.56}$$

$$\begin{cases} x_{\alpha p}(k) = x_\alpha(k) - x_{\alpha n}(k) = \frac{1}{2}\left[x_\alpha(k) \text{ - } x_\beta \ \left(k - \frac{1}{4}\frac{T}{T_S}\right)\right] \\ x_{\beta p}(k) = x_\beta(k) - x_{\beta n}(k) = \frac{1}{2}\left[x_\beta(k) + x_\alpha\left(k - \frac{1}{4}\frac{T}{T_S}\right)\right] \end{cases} \tag{III.57}$$

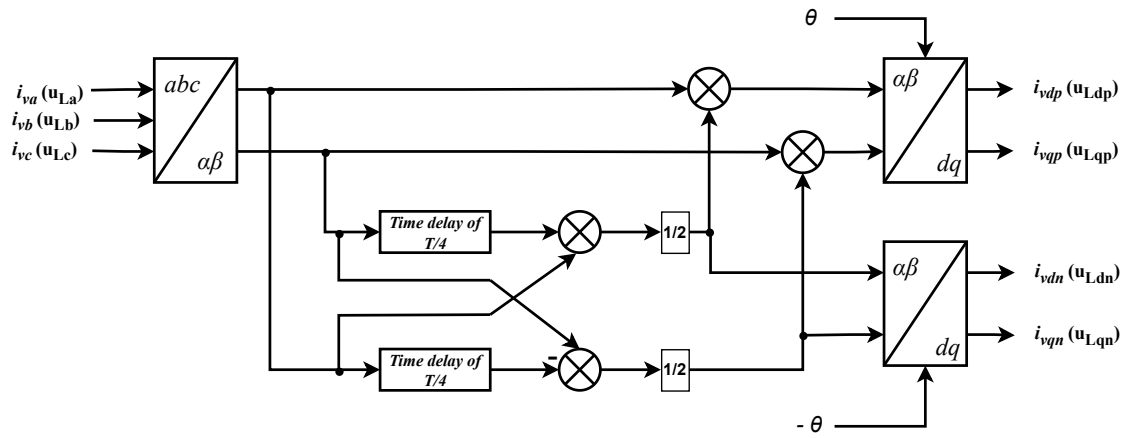


Figure III.20: Separation block of positive and negative sequence dq current

Where $x_{ap}, x_{cn}, x_{\beta p}$, and $x_{\beta n}$ represent the positive and negative sequence components along the ($\alpha$) and ($\beta$) axes, respectively. ( T ) denotes the period of the AC network, while ($T_S$) is the sampling interval of the control system. Voltage and current equations are subsequently converted from the ($\alpha\beta$) frame to the (dq) frame [105]. For the positive sequence components, this transformation follows the expression:

$$\begin{bmatrix} x_{dp} \\ x_{qp} \end{bmatrix} = \begin{bmatrix} \cos\theta & \sin\theta \\ -\sin\theta & \cos\theta \end{bmatrix} \begin{bmatrix} x_{\alpha p} \\ x_{\beta p} \end{bmatrix} \tag{III.58}$$

And for negative sequences:

$$\begin{bmatrix} x_{dn} \\ x_{qn} \end{bmatrix} = \begin{bmatrix} \cos\theta & -\sin\theta \\ \sin\theta & \cos\theta \end{bmatrix} \begin{bmatrix} x_{\alpha n} \\ x_{\beta n} \end{bmatrix} \tag{III.59}$$

Where $\theta = \omega t$, with $\omega$ representing grid pulsation, the equations III.51 and III.52 can be expressed in the (dq) frame as below:

$$\begin{aligned} \frac{d}{dt}\begin{bmatrix} i_{vdp} \\ i_{vqp} \end{bmatrix} &= \begin{bmatrix} -\frac{R_v}{L_v} & \omega \\ -\omega & -\frac{R_v}{L_v} \end{bmatrix} \begin{bmatrix} i_{vdp} \\ i_{vqp} \end{bmatrix} + \begin{bmatrix} \frac{1}{L_v} & 0 \\ 0 & \frac{1}{L_v} \end{bmatrix} \begin{bmatrix} u_{vdp} \\ u_{vqp} \end{bmatrix} \\ &- \begin{bmatrix} \frac{1}{L_v} & 0 \\ 0 & \frac{1}{L_v} \end{bmatrix} \begin{bmatrix} u_{Ldp} \\ u_{Lqp} \end{bmatrix} \end{aligned} \tag{III.60}$$

And also

$$\frac{d}{dt}\begin{bmatrix} i_{vdn} \\ i_{vqn} \end{bmatrix} = \begin{bmatrix} -\frac{R_v}{L_v} & -\omega \\ \omega & -\frac{R_v}{L_v} \end{bmatrix}\begin{bmatrix} i_{vdn} \\ i_{vqn} \end{bmatrix} + \begin{bmatrix} \frac{1}{L_v} & 0 \\ 0 & \frac{1}{L_v} \end{bmatrix}\begin{bmatrix} u_{vdn} \\ u_{vqn} \end{bmatrix} - \begin{bmatrix} \frac{1}{L_v} & 0 \\ 0 & \frac{1}{L_v} \end{bmatrix}\begin{bmatrix} u_{Ldn} \\ u_{Lqn} \end{bmatrix} \tag{III.61}$$

where $i_{vdp}, i_{vdn}, i_{vqp}, i_{vqn}$ are positive and negative sequence active current, positive and negative sequence reactive current, respectively.

From the equations III.60 and III.61, the equations for the positive and negative voltages supplied by the VSC converter are as follows:

$$\begin{cases} u_{vdp} = u_{Ldp} + R_v i_{vdp} - \omega L_v i_{vqp} + L_v \frac{d}{dt} i_{vdp} \\ u_{vqp} = u_{Lqp} + R_v i_{vqp} - \omega L_v i_{vdp} + L_v \frac{d}{dt} i_{vqp} \end{cases} \tag{III.62}$$

For negative sequence voltages :

$$\begin{cases} u_{vdn} = u_{Ldn} + R_v i_{vdn} + \omega L_v i_{vqn} + L_v \frac{d}{dt} i_{vdn} \\ u_{vqn} = u_{Lqn} + R_v i_{vqn} - \omega L_v i_{vdn} + L_v \frac{d}{dt} i_{vqn} \end{cases} \tag{III.63}$$

The average voltages during the sampling period (k to k+1) are calculated by integrating equations III.62 and III.63 from $kT_s$ to (k + 1) $T_s$, and then dividing by Ts (the sampling period).

$$\begin{cases} \bar{u}_{vdp} = \bar{u}_{Ldp} + R_v \bar{i}_{vdp} - \omega L_v \bar{i}_{vqp} + \frac{L_v}{T_S}\{i_{vdp}(k+1) - i_{vdp}(k)\} \\ \bar{u}_{vqp} = \bar{u}_{Lqp} + R_v \bar{i}_{vqp} + \omega L_v \bar{v}_{vdp} + \frac{L_v}{T_S}\{i_{vqp}(k+1) - i_{vqp}(k)\} \end{cases} \tag{III.64}$$

And

$$\begin{cases} \bar{u}_{vdn} = \bar{u}_{Ldn} + R_v \bar{i}_{vdn} + \omega L_v \bar{i}_{vqn} + \frac{L_v}{T_S}\{i_{vvn}(k+1) - i_{vvn}(k)\} \\ \bar{u}_{vqn} = \bar{u}_{Lqn} + R_v \bar{i}_{vqn} - \omega L_v \bar{i}_{vdn} + \frac{L_v}{T_S}\{i_{vqn}(k+1) - i_{vqn}(k)\} \end{cases} \tag{III.65}$$

Average voltage values during a sampling period are defined as follows:

$$\begin{cases} \bar{u}_{vdp} = \frac{1}{T_S}\int_{kT_S}^{(k+1)T_S} u_{vdp}(t)dt \\ \bar{u}_{vqp} = \frac{1}{T_S}\int_{kT_S}^{(k+1)T_S} u_{vqp}(t)dt \end{cases} \tag{III.66}$$

For negative sequence voltages :

$$\begin{cases} \bar{u}_{vdn} = \frac{1}{T_S}\int_{kT_S}^{(k+1)T_S} u_{vdn}(t)dt \\ \bar{u}_{vqn} = \frac{1}{T_S}\int_{kT_S}^{(k+1)T_S} u_{vqn}(t)dt \end{cases} \tag{III.67}$$

Assuming a linear network current and constant voltage, during the sampling period Ts, from equations III.66 and III.67, the equations are as follows:

$$\begin{cases} u_{vdp}(k+1) = u_{Ldp}(k) + \frac{R_v}{2}\{i_{vdp}(k+1) + i_{vdp}(k)\} \\ -\frac{\omega L_v}{2}\{i_{vqp}(k+1) + i_{vqp}(k)\} + \frac{L_v}{T_S}\{i_{vdp}(k+1) - i_{vdp}(k)\} \\ u_{vqp}(k+1) = u_{Lqp}(k) + \frac{R_v}{2}\{i_{vqp}(k+1) + i_{vqp}(k)\} \\ +\frac{\omega L_v}{2}\{i_{vdp}(k+1) + i_{vdp}(k)\} + \frac{L_v}{T_S}\{i_{vqp}(k+1) - i_{vqp}(k)\} \end{cases} \tag{III.68}$$

$$\begin{cases} u_{vdn}(k+1) = u_{Ldn}(k) + \frac{R_v}{2}\{i_{vdn}(k+1) + i_{vdn}(k)\} \\ +\frac{\omega L_v}{2}\{i_{vqn}(k+1) + i_{vqn}(k)\} + \frac{L_v}{T_S}\{i_{vdn}(k+1) - i_{vdn}(k)\} \\ u_{vqn}(k+1) = u_{Lqn}(k) + \frac{R_v}{2}\{i_{vqn}(k+1) + i_{vqn}(k)\} \\ -\frac{\omega L_v}{2}\{i_{vdn}(k+1) + i_{vdn}(k)\} + \frac{L_v}{T_S}\{i_{vqn}(k+1) - i_{vqn}(k)\} \end{cases} \tag{III.69}$$

The control relies on equations III.68 and III.69; additionally, the inner current adjustment loop typically introduces a sample delay due to computation time and a brief interval between valve operations (turn-on/off) to prevent a short circuit on the continuous side of the converter, and at time (k+1), the voltages and currents are equal to their reference values at time k.

$$\begin{cases} x_{vdp}(k+1) = x^*_{vdp}(k) \\ x_{vqp}(k+1) = x^*{}_{vqp}(k) \\ x_{vdn}(k+1) = x^* v_{vnn}(k) \\ x_{vqn}(k+1) = x^*{}_{vqn}(k) \end{cases} \tag{III.70}$$

Then the control equations for voltages and currents are as follows:

$$\begin{cases} u^*_{vdp}(k) = u_{Ldp}(k) + R_v i_{vdp}(k) - \frac{\omega L_v}{2}\left(i^*_{vqp}(k) + i_{vqp}(k)\right) \\ +k_p\left(i^*_{vdp}(k) - i_{vdp}(k)\right) \\ u^*_{vqp}(k) = u_{Lqp}(k) + R_v i_{vqp}(k) + \frac{\omega L_v}{2}\left(i^*_{vdp}(k) + i_{vdp}(k)\right) \\ +k_p\left(i^*_{vqp}(k) - i_{vqp}(k)\right) \end{cases} \tag{III.71}$$

And

$$\begin{cases} u^*_{vdn}(k) = u_{Ldn}(k) + R_v i_{vdn}(k) + \frac{\omega L_v}{2}\left(i^*_{vqn}(k) + i_{vqn}(k)\right) \\ +k_p\left(i^*_{vdn}(k) - i_{vdn}(k)\right) \\ u^*_{vqn}(k) = u_{Lqn}(k) + R_v i_{vqn}(k) + \frac{\omega L_v}{2}\left(i^*_{vdn}(k) + i_{vdn}(k)\right) \\ +k_p\left(i^*_{vqn}(k) - i_{vqn}(k)\right) \end{cases} \tag{III.72}$$

Where the gain is given by:

$$k_p = k_{pf}\left(\frac{L_v}{T_S} + \frac{R_v}{2}\right) \tag{III.73}$$

The current regulator is implemented as shown in Figure III.21. Through the external regulators, the reactive and active current reference values are added.

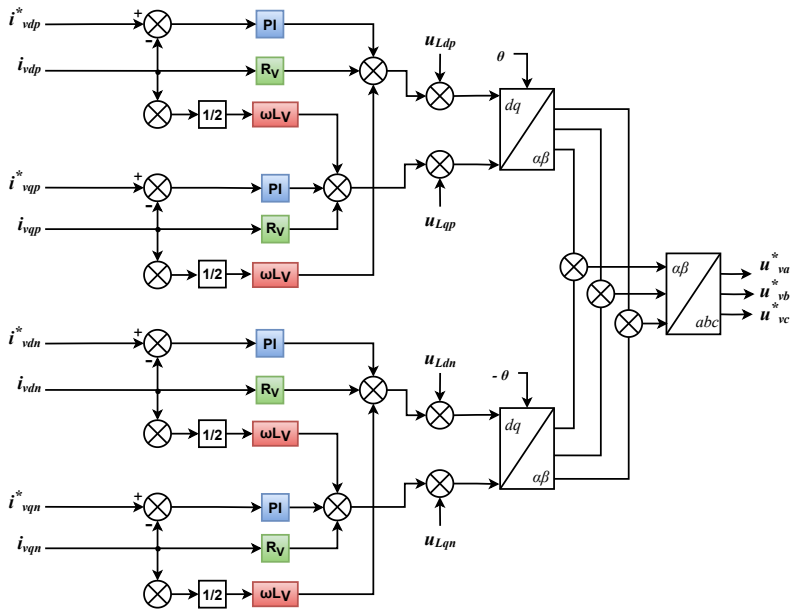


Figure III.21: Block Diagram of the Inner Current Control Loop

# III.4 External regulators

## III.4.1 DC voltage control

A converter is responsible for controlling the DC voltage by adjusting the amount of active power it exchanges with its AC network. When there's a drop in the DC voltage, the converter introduces a phase lag in the generated AC voltage, drawing more active power from the AC grid to increase the DC voltage. On the other hand, if the DC voltage is too high, the converter applies a phase lead to the AC voltage, supplying more active power to the AC network to bring the DC voltage down [74].

This adjustment provides the minimal additional power needed to charge or discharge the capacitor, maintaining the target DC voltage level. A proportional (P) or PI controller is commonly employed to perform this regulation [106].

The real-time active power, $P_{AC}$, and reactive power, $Q_{AC}$, exchanged in the AC system (the AC side of the VSC converter), along with the DC power, $P_{dc}$, transmitted through the DC link (the DC side of the VSC converter) are described by the following equations, as depicted in Figure III.19.

$$\begin{cases} P_{AC(abc)} = u_{La} \cdot i_{va} + u_{Lb} \cdot i_{vb} + u_{Lc} \cdot i_{vc} \\ Q_{AC(abc)} = (u_{La} - u_{Lb}) \cdot i_{vc} + (u_{Lb} - u_{Lc}) \cdot i_{va} + (u_{Lc} - u_{La}) \cdot i_{vb} \end{cases} \tag{III.74}$$

$$P_{dc} = u_{dc} \cdot i_{dc} \tag{III.75}$$

In normal operation, the voltages in the AC system are balanced; therefore, the components $u_{L\alpha n}$, $u_{L\beta n}$, and $u_{Ldn}$,$u_{Lqn}$ in references ($\alpha\beta$) and (dq), respectively, are zero. Then the components $u_{Ldp}$, and $u_{Lqp}$ can be described as follows:

$$\begin{cases} u_{Ldp} = 0 \\ u_{Lqp} = U \end{cases} \tag{III.76}$$

Where U represents the voltage magnitude, from equations the instantaneous forces (active and reactive) in the dq frame can be expressed by the following equations:

$$\begin{cases} P_{AC(dq)} = u_{Ldp} \cdot i_{vdp} + u_{Lqp} \cdot i_{vqp} = u_{Lqp} \cdot i_{vqp} \\ Q_{AC(dq)} = u_{Lqp} \cdot i_{vdp} - u_{Ldp} \cdot i_{vqp} = u_{Lqp} \cdot i_{vdp} \end{cases} \tag{III.77}$$

For the DC voltage regulator, a current is assumed to match the reference value. The formulas for active and reactive power are provided:

$$\begin{cases} P_{AC(dq)} = u_{Lqp} \cdot i^*_{vqp} \\ Q_{AC(dq)} = u_{Lqp} \cdot i^*_{vdp} \end{cases} \tag{III.78}$$

The equation for the transmitted power when neglecting losses in the transformer and reactor is as follows:

$$P_{AC(dq)} = u_{Lqp} \cdot i^*_{vqp} = P_{dc} = u_{dc} \cdot i_{dc} \tag{III.79}$$

Than

$$i_{dc} = \frac{u_{Lqp} \cdot i^*_{vqp}}{u_{dc}} \tag{III.80}$$

The equation for the DC voltage through the capacitors is:

$$C_{dc} \frac{d}{dt} u_{dc} = i_{dc} - i_{load} \tag{III.81}$$

Where $i_{load}$ refers to the direct current of the DC line, by Integrating equation III.81 on the interval from kTs and (k + 1)T and then dividing by Ts, and assuming both $i_{dc}$ and $i_{load}$ are constant we obtain :

$$\frac{C_{dc}}{T_s} \{u_{dc}(k+1) - u_{dc}(k)\} = i_{dc} - i_{load} \tag{III.82}$$

When the sampling period of the regulator is delayed, the reference voltage can be obtained as follows:

$$u_{dc}(K+t) = U^*_{dc}(K) \tag{III.83}$$

The current reference can be found by substituting equations III.81 and III.83 into III.82, we obtain:

$$i^*_{vqp}(k) = k_{dcp}\left(u^*_{dc}(k) - u_{dc}(k)\right) + k_{load} \cdot i_{load}(k) \tag{III.84}$$

With

$$\begin{cases} k_{dcp} = k_{dcpf}\frac{u^*_{dc}(k)}{u_{Lqp}(k)}\frac{C_{dc}}{T_s} \\ k_{load} = \frac{u^*_{dc}(k)}{u_{Lqp}(k)} \end{cases} \tag{III.85}$$

To stabilize the system, the $k_{dcpf}$ factor can adjust the gain of the DC voltage regulator Figure III.22 shows the DC voltage regulator diagram.

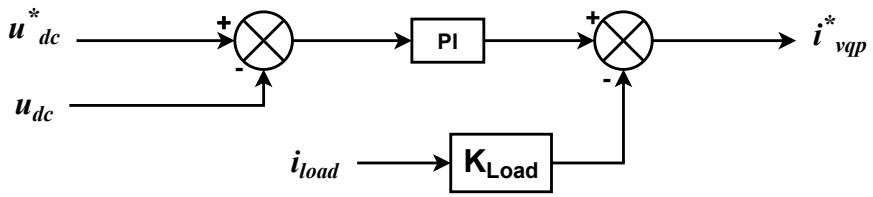


Figure III.22: Block of DC voltage control

### III.4.2 AC side active power control

The converter regulates power exchange with the AC network without managing the DC voltage. In multi-terminal systems, one converter manages DC voltage while others control active power exchange.

Active power control is accomplished by manipulating the phase angle of the converter's fundamental frequency. The active power flow is determined by the phase angle's sign, indicating whether power is absorbed or supplied. Effective power transfer in VSC-HVDC links necessitates coordinated operation of both converter stations [107, 108]. When the generated voltage aligns with the network, the current becomes orthogonal to the voltage, resulting in zero power exchange. If the generated voltage leads to the network voltage, the VSC supplies active power due to collinear current. Conversely, if the generated voltage lags, the VSC absorbs active power from the network [106].

As shown in Figure III.23, an open-loop regulator is the simplest method of active power control, assuming that the voltages are balanced. From equation III.78 the active current reference is given by:

$$i^*_{vqp} = \frac{P^*}{u_{Lqp}} \tag{III.86}$$

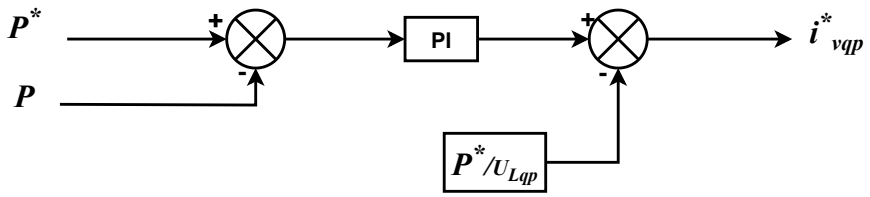


Figure III.23: Block of active power control

### III.4.3 AC side reactive power control

On the AC side, the VSC generates a three-phase voltage aligned with the network to control the phase reactance potential difference. Initially, We assume that the voltage generated in the phase is identical to the grid voltage.if the generated voltage has a lower amplitude than that of the network [81, 108], the current induced by the reactance, due to the potential difference, lags in quadrature relative to the network voltage. In this scenario, the current is in quadrature advance compared to the voltage of the network [107].

Consequently, the converter acts as a capacitor, supplying reactive energy to the network. Conversely, if the generated voltage amplitude exceeds that of the network, the VSC mimics a reactance, absorbing reactive energy from the network. The reactive power managed by the VSC is regulated by the AC voltage magnitude via the modulation index (using PWM), which is crucial for maintaining the AC voltages of other converters in the transmission system [107].

Figure III.24 shows the reactive power regulator. Through Eq III.78, the open-loop regulator is obtained by the equation:

$$i^*_{vdp} = \frac{Q^*}{u_{Lqp}} \tag{III.87}$$

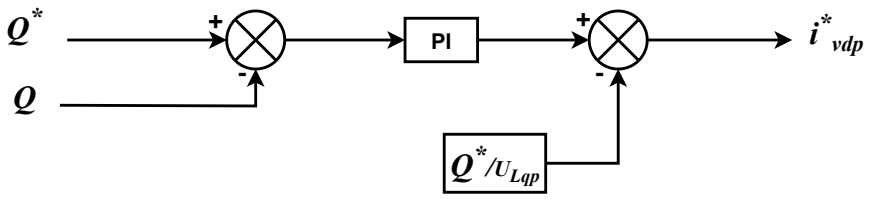


Figure III.24: Block of reactive power control

### III.4.4 Control of frequency

The regulation of the oscillator frequency, which dictates the sequence of pulses for the valves of the converter, is of paramount importance when the VSC operates as the sole power source, specifically in scenarios where the VSC-HVDC link supplies an isolated network or a passive load. Conversely, when the VSC is integrated within an active system, it can use the frequency control mechanism by modulating the power it supplies to or absorbs from the interconnected AC network. The primary function of a frequency regulator is to sustain the frequency at its designated reference value. The power variation corresponding to a change in frequency within an interconnected network is called system stiffness [109]. A linear approximation can effectively represent the power-frequency relationship:

$$\frac{\Delta P}{\Delta f} = k_f \tag{III.88}$$

Where $\Delta P$ is the change in power, $k_f$ is the system stiffness. $\Delta f$ is the frequency deviation.

A greater $k_f$ indicates a greater stiffness of the system, necessitating large changes in power to achieve small adjustments in frequency. In contrast, a lower $k_f$ indicates a more flexible system, allowing small changes in power that result in large deviations in frequency.

In the normal system, the frequency is controlled and the control error is reduced to zero by using a PI regulator in the feedback loop Figure III.25 shows the frequency regulator.

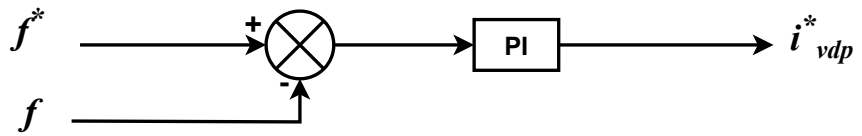


Figure III.25: Block of frequency control

### III.4.5 AC alternating voltage control

When a VSC feeds an isolated AC system, the AC voltage controller plays a key role in ensuring that the output voltage aligns with the set reference value. This controller also controls the power delivered to the load, provided that the rectifier station is responsible for managing the DC voltage of the HVDC connection. By keeping the AC voltage at the proper level, the system offers a consistent and dependable power supply to the load [109]. Additionally, the On-Load Tap-Changer (OLTC) changes the transformer taps to match fluctuations in load circumstances or system needs. As a result, the modulation index of the VSC, which governs the amplitude of the output voltage in respect to the DC-link voltage, is modified correspondingly to complement these tap variations and provide constant AC voltage stability [81].

The voltage drop $\Delta V$ across the reactance is depicted in Figure III.26.

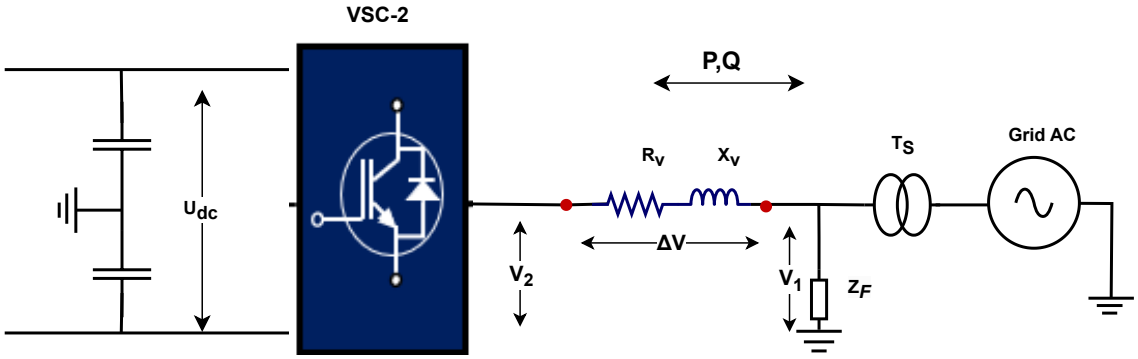


Figure III.26: A VSC-HVDC link of side VSC-2

The equation for the voltage drop $\Delta V$ across the reactance is given as :

$$\Delta V \approx \frac{R_v \cdot P + X_v \cdot Q}{V_1} \tag{III.89}$$

The voltage drop $\Delta V$ relies only on the reactive power. So the change in AC voltage $V_1$ is also dependent on the reactive power. From equations III.78 and III.89, an AC voltage regulator block diagram can be obtained as shown in Figure III.27.

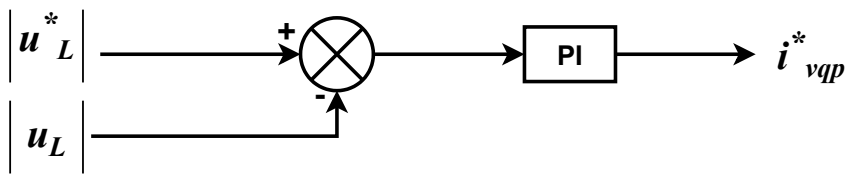


Figure III.27: Block of AC voltage regulator

Where $|u_L|$ and $|u_L^*|$ denote the magnitude of the line voltage and its reference value, respectively.

## III.4.6 Artificial neural network technology

### III.4.6.1 Definition of ANN

ANNs are computational models inspired by the structure and function of the human brain, designed to process and interpret complex, nonlinear data through interconnected processing elements known as neurons. These models are widely used in various fields, including renewable energy systems, due to their adaptability, fault tolerance, and ability to approximate nonlinear functions without explicit mathematical models [110]. An ANN typically consists of an input layer, one or more hidden layers, and an output layer, where each neuron performs a weighted sum of its inputs followed by a nonlinear activation function [110, 111]. Figure III.28 shows the structure of artificial neurons inspired by biological neurons.

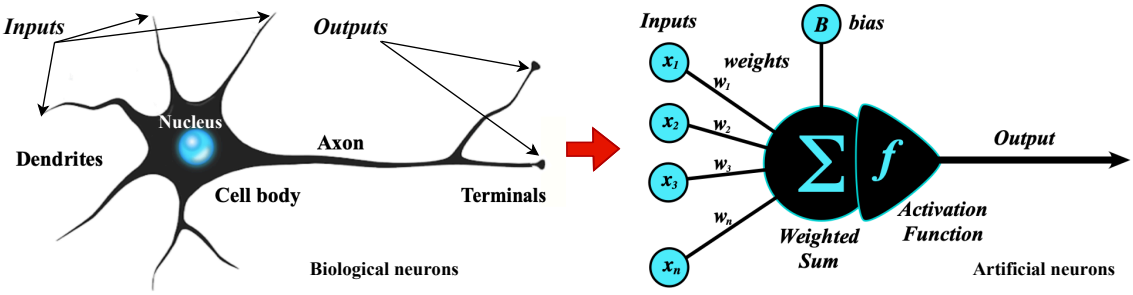


Figure III.28: The structure of artificial neurons inspired by biological neurons

### III.4.6.2 The main components of ANN

ANNs operate according to key components and working principles, which include the following [110]:

1. **Neurons (Nodes):** These are the basic processing units of an ANN, organized in layers. Each neuron receives inputs, processes them, and produces an output .

2. **Connections and weights:** Neurons in one layer are connected to neurons in subsequent layers. Each connection has an associated weight, which determines the strength and importance of the input signal. These weights are the primary parameters learned during the training process.

3. **Activation functions:** After summing the weighted inputs, an activation function is applied to the result. This function introduces non-linearity into the network, enabling it to learn complex patterns and map inputs to outputs in a non-linear fashion. Common activation functions include Sigmoid, ReLU (Rectified Linear Unit), Tanh, and Softmax.

4. **Layers:** ANNs are structured into three types of layers:
   1- input layer: Receives the initial data. The number of neurons in this layer corresponds to the number of features in the input dataset.

   2- Hidden layers: One or more layers between the input and output layers where the majority of the computation and pattern recognition occurs.

   3- Output layer: Produces the final result of the network, such as a classification label or a predicted value. The number of neurons in this layer depends on the nature of the task.

The basic working principle of an ANN involves two main phases: forward propagation and backpropagation.

- Forward propagation: In this phase, input data is fed into the input layer and propagates through the network, layer by layer, until it reaches the output layer. Each neuron in a hidden or output layer calculates its output by taking the weighted sum of its inputs from the previous layer and then applying an activation function. This process generates a prediction or output from the network.

- Backpropagation: This is the core learning algorithm for training multi-layered ANNs. After forward propagation, the network's output is compared to the actual target output, and an error is calculated. Backpropagation then calculates the gradient of this error with respect to each weight in the network, effectively determining how much each weight contributed to the error. This error information is propagated backward through the network, from the output layer to the input layer. Based on these gradients, the network's weights are adjusted iteratively to minimize the error. This iterative process of forward propagation, error calculation, and backpropagation continues until the network's predictions are sufficiently accurate or a stopping criterion is met. Figure III.29 shows a diagram of the structure of an ANN.

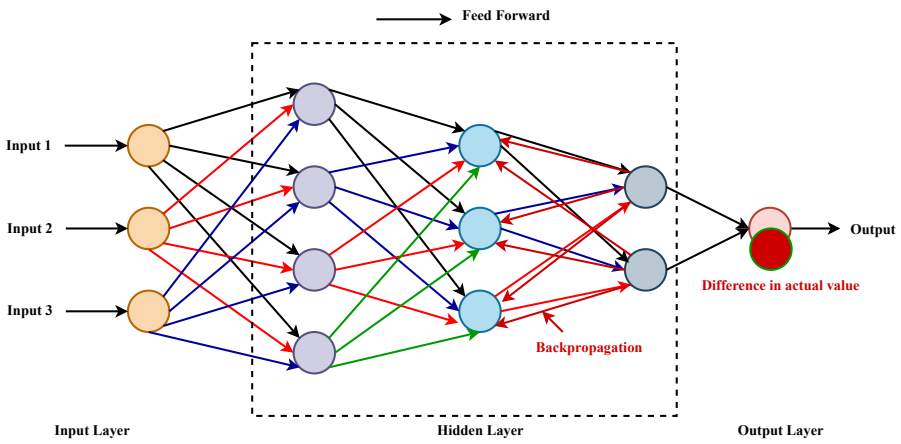


Figure III.29: The diagram of the structure of an ANN

### III.4.6.3 Types of ANN

ANNs have different types, each designed to excel at specific types of tasks and data structures. The choice of architecture significantly impacts the network's ability to learn and generalize. Among the most commonly used ANN structures are the following:

1. **Feed Forward Neural Network (FFNN)**

   A FFNN represents one of the most fundamental architectures within ANNs. In this structure, information propagates unidirectionally from the input layer, through one or more hidden layers, to the output layer without forming feedback connections

or cycles. As a result, data never re-enters a preceding layer. FNNs are generally applied to relatively straightforward tasks, such as basic classification and regression, where computational complexity and temporal dependencies are minimal [110].

2. **Convolutional Neural Network (CNN)**

   A CNN is specifically designed to process data characterized by a grid-like topology, such as images or structured spatial datasets. It incorporates convolutional layers that employ learnable filters to extract salient features such as edges, shapes, and textures from raw input data. This hierarchical feature extraction enables CNNs to excel in pattern recognition tasks, including image classification, object detection, and speech recognition, where the identification of spatial or structural patterns is essential [110].

3. **Radial Basis Function Network (RBFN)**

   A RBFN is a specialized ANN architecture suited for problems in which input data can be effectively represented using radial or spherical functions. Typically comprising an input layer, a hidden layer with radial basis activation functions, and an output layer, RBFNs transform inputs into a higher-dimensional feature space before performing the final mapping to outputs. They are particularly advantageous for classification and regression applications involving data with nonlinear relationships or distinct geometric patterns [110].

4. **Recurrent Neural Network (RNN)**

   An RNN is architected to process sequential or temporal data, such as time-series signals, text, or audio. Unlike feedforward structures, RNNs incorporate feedback connections that allow outputs from previous time steps to be reintroduced into the network's processing pathway. This recurrent mechanism equips the model with a form of memory, enabling it to capture contextual dependencies across sequences.

Consequently, RNNs are widely utilized in applications such as language modeling, speech recognition, and temporal forecasting, where prior information influences current predictions [110].

#### III.4.6.4 Training an ANN

Training an ANN involves adjusting its internal parameters (weights and biases) to minimize the difference between its predictions and the actual target values. This process is essentially an optimization problem, where the goal is to find the optimal set of parameters that allows the network to perform its task effectively. Various algorithms and techniques are employed for this purpose, such as the Gradient Descent and Levenberg-Marquardt algorithms, and details of these methods are provided in [110], each with its strengths and weaknesses.

#### III.4.6.5 Control of VSC-HVDC system based on FFNN

FFNNs are trained under a supervised learning paradigm, where weight parameters are optimized to minimize prediction errors, commonly evaluated using metrics such as mean squared error (MSE) or sum squared error (SSE). Here, the Levenberg–Marquardt optimization technique was used to ensure rapid convergence. Once trained, the network's generalization capability is evaluated using previously unseen data. Figure III.30 illustrates the steps involved in implementing the FFNN technique, while Figure III.31 illustrates the structure of an FFNN.

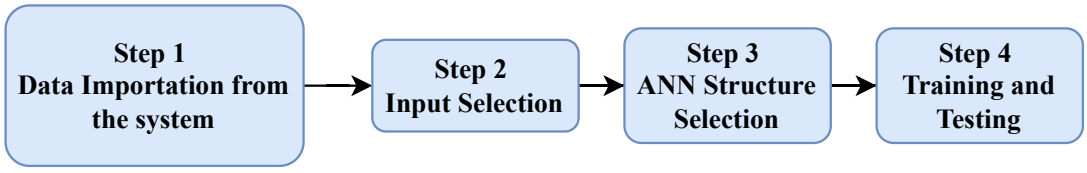


Figure III.30: The steps of FFNN technique

The mean squared error is calculated using the following formula:

$$\begin{cases} \text{MSE} = \frac{1}{n}\sum_{i=1}^{n}\left(Y_{T_i} - Y_i\right)^2 \\ Y_i = f\left(\sum_j w_{ij}x_i + b\right) \end{cases} \tag{III.90}$$

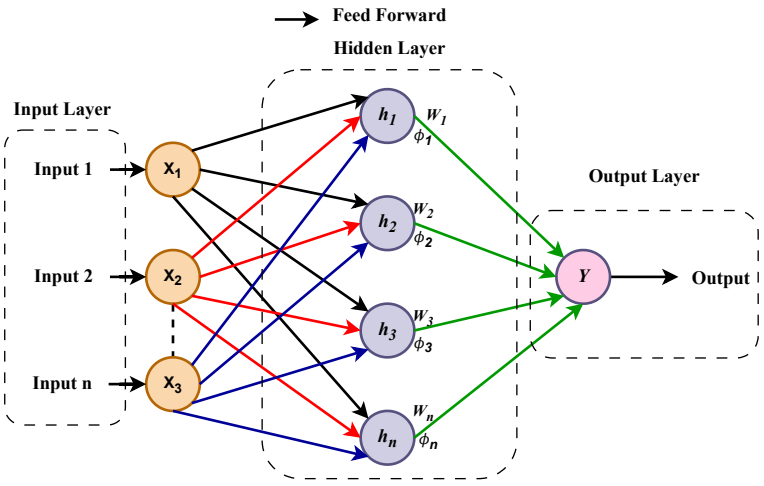


Figure III.31: The structure of an FFNN

where $n$ denotes the number of samples in the dataset, $Y_{T_i}$ represents the target value of the $i^{\text{th}}$ sample, and $Y_i$ is the predicted value for the $i^{\text{th}}$ sample. The prediction $Y_i$ is obtained by applying the activation function $f(\cdot)$, specifically the sigmoid function, to the weighted sum of the input features and the bias term. Here, $m$ denotes the number of input features, $w_{ij}$ is the weight connecting the $j^{\text{th}}$ input feature to the output neuron $i$, $x_j$ is the value of the $j^{\text{th}}$ input feature, and $b$ is the bias term.

The FFNN is implemented in the following four main steps:

In the first step, data are extracted from the simulation environment, ensuring that the dataset adequately reflects the system's dynamic response across a wide range of operating scenarios. This comprehensive representation is essential to enhance the robustness and generalization capability of the neural network.

In the second step, relevant input variables are identified based on their influence on the system output and their significance with respect to the defined control objectives. In the system studied, the selection of inputs and outputs was made according to the following approach:

$$\begin{cases} \text{Input}_1 : \ e_{V_{dc}} = V_{dc}^* - V_{dc} \quad \Rightarrow \quad \text{Output}_1 : \ i_d^* \\ \text{Input}_2 : \ e_Q = Q^* - Q_{\text{meas}} \quad \Rightarrow \quad \text{Output}_2 : \ i_q^* \\ \text{Input}_3 : \ e_d = i_d^* - i_d \quad \Rightarrow \quad \text{Output}_3 : \ V_d^* \\ \text{Input}_4 : \ e_q = i_q^* - i_q \quad \Rightarrow \quad \text{Output}_4 : \ V_q^* \end{cases} \tag{III.91}$$

The third step involves defining the architecture of the FFNN, which includes specifying the number of hidden layers, the number of neurons in each layer, and the activation functions to be employed.

Finally, in the fourth step, the network is trained using the previously collected simulation data. The Levenberg–Marquardt optimization algorithm is applied to iteratively adjust the network's internal weights to achieve optimal predictive accuracy. Upon completion of the training phase, the model is validated using previously unseen data to verify its capability to maintain accurate and reliable performance under new operating conditions.

The control of both VSC1 and VSC2 is implemented using a hierarchical dual-loop strategy composed of an inner current control loop and an outer loop. In VSC1, which manages the hybrid renewable energy source side, the inner loop regulates the grid-injected current in the synchronous rotating (d–q) reference frame, effectively decoupling the control of active and reactive power. Here, the database (inputs and outputs) is extracted through the PI controller and trained using the FFNN module, as shown in Figure III.32 and according to the approach described in Equation III.91.

The outer loop in this case governs the reference signals for active and reactive power according to the demands of the system. Similarly, VSC2 located on the grid side, regulates the DC link voltage to maintain power balance between the two terminals. It also employs an outer loop to control the DC voltage and an inner current loop for fast dynamic response. Both VSCs utilize a similar current control structure, but the VSC2 connected

to the grid has a PLL to synchronize with the phase and frequency of the grid voltage [112].

The overall control configuration of VSC1 and VSC2 is illustrated in Figure III.33, and Figure III.34 also shows that DC-link voltage control and reactive power are controlled using the FFNN module.

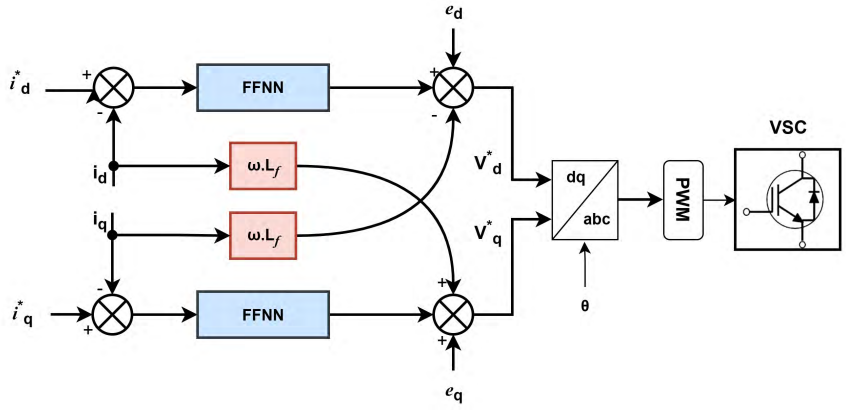


Figure III.32: Inner control loop with FFNN

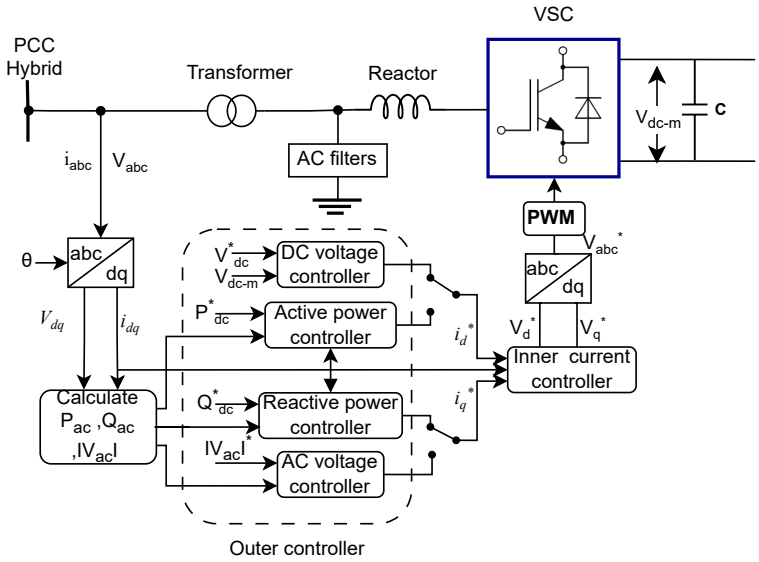


Figure III.33: The overall control configuration of VSC

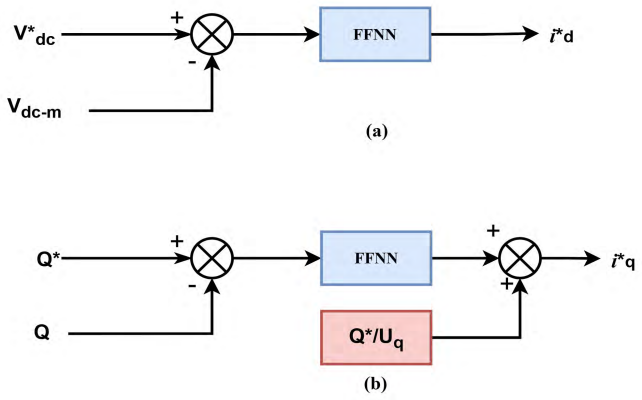


Figure III.34: The outer controllers: (a) DC-link voltage control, (b) reactive power control

## III.5 Conclusion

Integrating hybrid renewable energy systems into power grids necessitates advanced control strategies to ensure operational efficiency and reliability. Combining PV and wind energy, these systems leverage complementary characteristics to optimize performance under variable conditions. This chapter explored foundational control methods crucial for coordinating energy sources and maintaining grid stability.

The control techniques applied in this work are based on the ability to adaptively manage both active and reactive power. For PV systems, MPPT algorithms based on DO, PSO, GWO, and P&O, have been highlighted for their role in optimizing energy extraction under various dynamic conditions. For the wind energy system, a lookup table technique was used to extract the appropriate output power. The current and power controllers were integrated to maintain voltage stability and ensure compliance with the grid codes. Furthermore, dq-axis control was employed to independently regulate active and reactive power, while SVPWM was used to enhance the inverter's performance by improving the utilization of the DC link and reducing harmonic distortion. Together, these techniques contribute to the robust operation of hybrid energy systems, enabling them to respond effectively to disturbances and external changes.

For HVDC-VSC systems, the VSC-HVDC system provides independent control of active and reactive power. This is achieved through the use of inner current control loops

and the outer controllers based on an FFNN strategy, which ensure dynamic response and maintain power quality and grid stability. Additionally, the separation of positive and negative sequence components within the dq reference frame allows for precise control under unbalanced conditions, further enhancing the system's reliability. In the next chapter, we will discuss the simulation results of the studied system.

# Chapter IV

# System simulation and discussion of results

## IV.1 Introduction

The integration of renewable energy with HVDC-VSC transmission systems ensures efficient, stable, and flexible energy transmission, making it one of the most promising solutions for energy transmission. However, the system requires control strategies to achieve better robustness, performance, and stability to achieve system reliability.

This chapter focuses on two complementary aspects of renewable energy integration. First, the enhancement of PV systems through MPPT is examined using a dandelion-inspired optimization (DO) algorithm. The proposed method is evaluated against conventional MPPT techniques, including perturb and observe (P&O), particle swarm optimization (PSO), and grey wolf optimization (GWO), under varying irradiance and temperature conditions. The objective is to assess improvements in tracking accuracy, convergence speed, and operational stability.

Second, this chapter investigates the performance of HVDC-VSC integrated with HRES. A FFNN-based controller is employed to improve DC-link voltage regulation and optimize the management of active and reactive power flows. By leveraging its nonlinear and adaptive characteristics, the FFNN addresses the inherent limitations of conventional PI controllers, particularly under rapidly changing environmental and operating conditions.

This chapter presents optimized and intelligent control solutions to improve performance and reliability in renewable energy systems and power transmission grids.

Third, this chapter analyzes the behavior of HVDC-VSC systems under pole-to-pole and pole-to-ground short-circuit faults.

## IV.2 Enhancing the power of PV systems using MPPT based on the dandelion algorithm

This section presents a comparative analysis of the proposed DO algorithm with three widely used MPPT techniques: P&O, PSO, and GWO. In this work, two scenarios are employed to analyze the tracking accuracy, dynamic stability, and response speed of each method. In the first scenario, the radiation is varied at a constant temperature, while in the second scenario, the temperature is varied while the radiation value is kept constant. The technical specifications of the PV module are presented in Table (Appendix B.1), while the electrical parameters of the boost converter components employed in the system are detailed in Table (AppendixB.2). Figure IV.1 illustrates the structure of the studied system, consisting of a PV array integrated with a boost converter and connected to a stand-alone load.

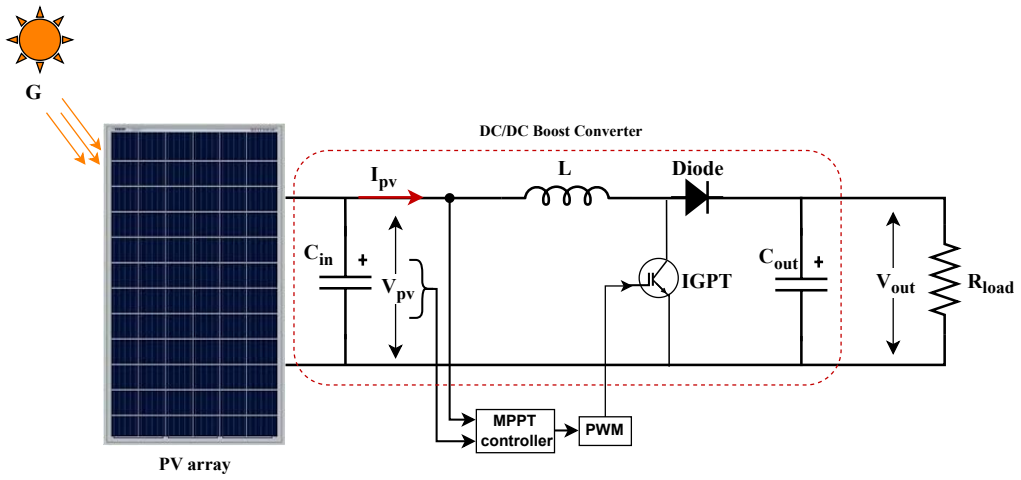


Figure IV.1: Structure of PV array with DC-DC boost converter and MPPT control

### IV.2.1 Scenario of varying solar radiation

In this scenario, the system experiences rapid changes in solar irradiance every 0.2 s, with levels sequentially set to 1000 W/m$^2$, 700 W/m$^2$, 600 W/m$^2$, 800 W/m$^2$, and returning to 1000 W/m$^2$. Throughout the process, the temperature is kept constant at 25 °C, as illustrated in Figure IV.2.

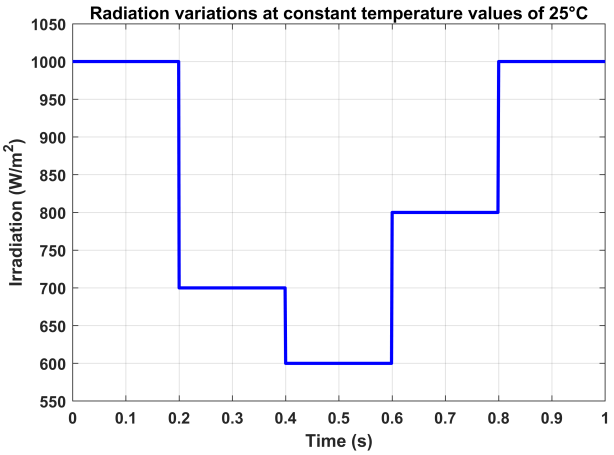


Figure IV.2: Profile of solar irradiance variations

The results of the different applied methods were obtained under previously defined solar irradiance conditions. Figure IV.3 presents the output power, voltage, and current of the boost converter. Table IV.1 presents the performance of each method under varying irradiance conditions.

Based on the analysis of boost converter outputs for different MPPT techniques, the DO algorithm consistently delivers superior performance across key metrics. It achieves the fastest tracking response, converging within 0.02 s at 1000 W/m$^2$ and sustaining this rapid performance under varying irradiance levels. The P&O method follows with a steady convergence time of 0.03 s, while PSO and GWO reach steady state more slowly, at 0.11 s and 0.075 s respectively, with GWO showing the slowest initial response. In terms of tracking efficiency, DO records the highest average value of 94.72%, followed by GWO (94.52%) and PSO (94.23%), whereas P&O achieves the lowest average efficiency of 93.82%, particularly under low irradiance conditions.

For output stability, DO maintains minimal oscillations across all test scenarios, while P&O provides stable steady-state operation. PSO and GWO exhibit moderate oscillations during initial convergence, though GWO demonstrates better stability at lower irradiance. All controllers adapt to irradiance changes in approximately 0.05 s; however, DO remains the most robust, maintaining both high efficiency and stability. GWO and PSO adapt effectively but with slightly reduced efficiency, while P&O shows the weakest adaptability,

with a noticeable efficiency drop during irradiance transitions.

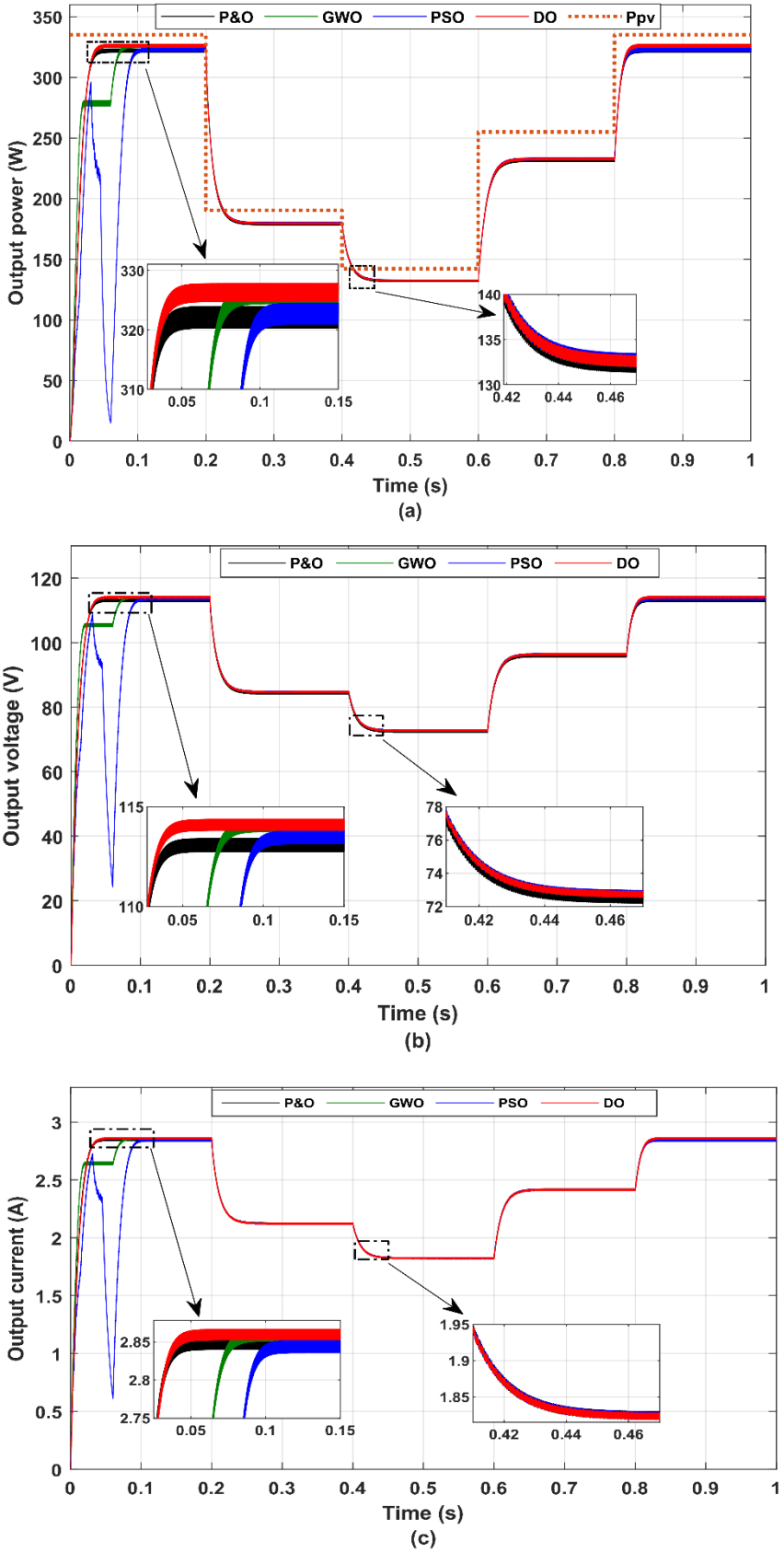


Figure IV.3: Output results of the boost converter with different MPPT methods under variable solar irradiance scenarios: (a) power, (b) voltage, (c) current

| **Irradiation (W/m$^2$)** | **1000** | **700** | **600** | **800** |
|---|---|---|---|---|
| **Theoretical $P_{max}$ from PV array (W)** | 335.2 | 190.4 | 142.2 | 255.1 |
| **DO** | | | | |
| $P_{max}$ (W) | 327.85 | 181.24 | 133.73 | 234.31 |
| $V_{max}$ (V) | 114.37 | 84.87 | 72.90 | 96.59 |
| Efficiency (%) | 97.80 | 95.18 | 94.04 | 91.85 |
| **GWO** | | | | |
| $P_{max}$ (W) | 327.72 | 180.66 | 133.28 | 233.95 |
| $V_{max}$ (V) | 114.35 | 84.90 | 72.92 | 96.61 |
| Efficiency (%) | 97.76 | 94.88 | 93.73 | 91.71 |
| **PSO** | | | | |
| $P_{max}$ (W) | 324.57 | 179.83 | 133.29 | 233.48 |
| $V_{max}$ (V) | 113.80 | 84.94 | 72.96 | 96.63 |
| Efficiency (%) | 96.82 | 94.45 | 94.15 | 91.50 |
| **P&O** | | | | |
| $P_{max}$ (W) | 324.01 | 179.03 | 132.82 | 232.65 |
| $V_{max}$ (V) | 113.42 | 84.54 | 72.62 | 96.19 |
| Efficiency (%) | 96.66 | 94.02 | 93.40 | 91.19 |

Table IV.1: The performance of each method under varying irradiance conditions

### IV.2.2 Scenario of varying temperature

In this scenario, the system experiences rapid temperature variations at 0.2 s intervals, with values of 15°C, 25°C, 35°C, 45°C, and 25°C, respectively, while the irradiance remains constant at 1000 W/m$^2$, as shown in Figure IV.4.

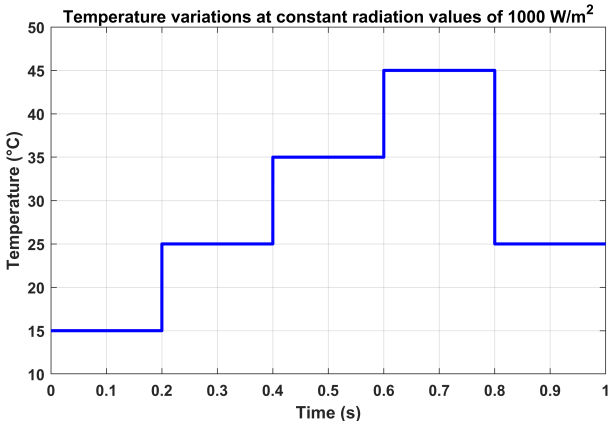


Figure IV.4: Profile of temperature variations

Figure IV.5 and Table IV.2 present the results obtained for the different MPPT methods in different temperature scenarios.

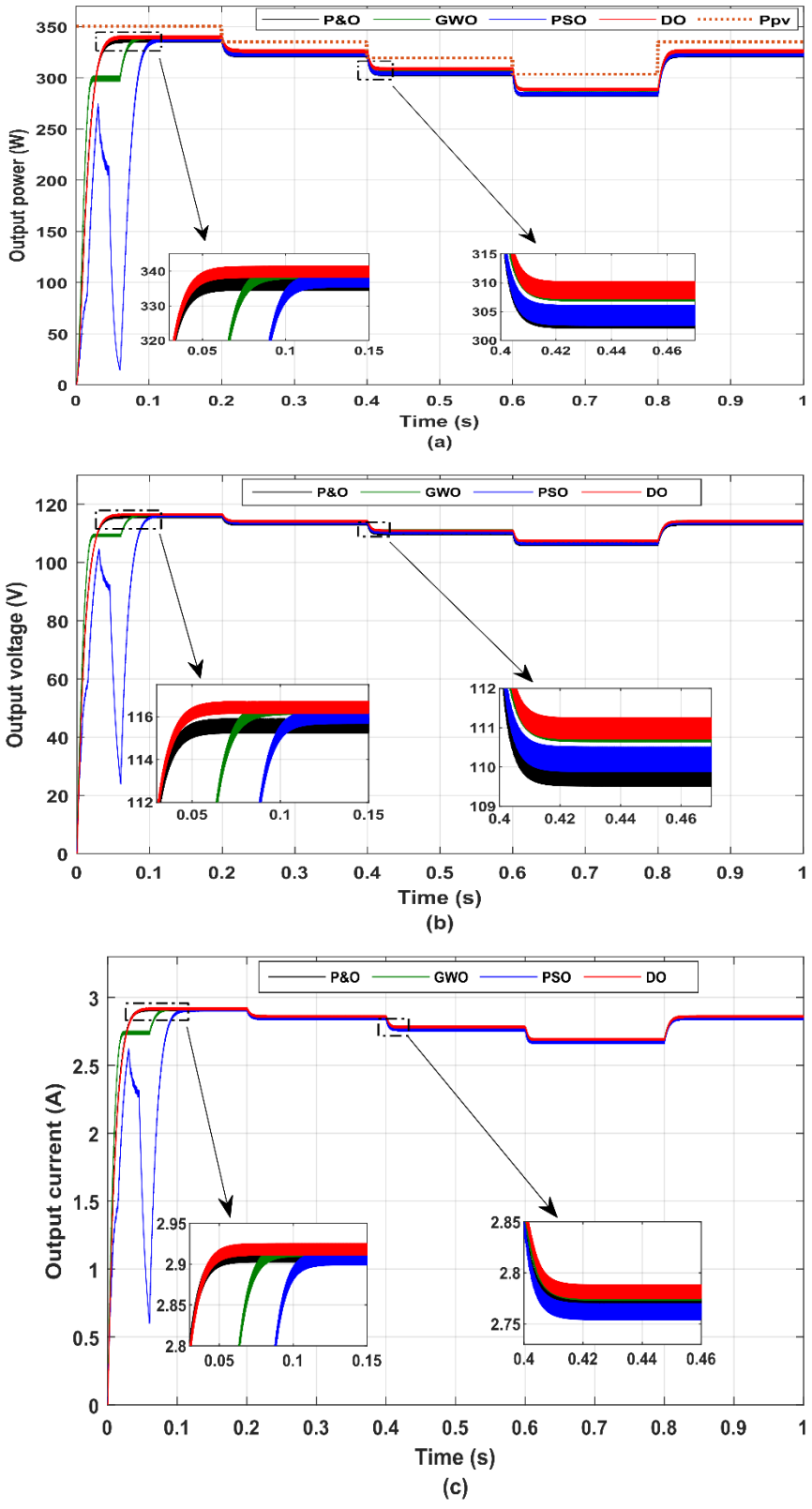


Figure IV.5: Output results of the boost converter with different MPPT methods under variable temperature scenarios: (a) power, (b) voltage, (c) current

| **Temperature (°C)** | **15** | **25** | **35** | **45** |
|---|---|---|---|---|
| **Theoretical $P_{max}$ from PV array (W)** | 350.5 | 335.2 | 319.4 | 303.5 |
| **DO** | | | | |
| $P_{max}$ (W) | 341.40 | 327.85 | 310.86 | 290.63 |
| $V_{max}$ (V) | 116.72 | 114.37 | 111.50 | 107.71 |
| Efficiency (%) | 97.35 | 97.80 | 97.33 | 95.76 |
| **GWO** | | | | |
| $P_{max}$ (W) | 341.13 | 327.72 | 310.02 | 290.00 |
| $V_{max}$ (V) | 116.72 | 114.35 | 111.22 | 107.57 |
| Efficiency (%) | 97.24 | 97.76 | 97.06 | 95.55 |
| **PSO** | | | | |
| $P_{max}$ (W) | 339.26 | 324.57 | 306.11 | 285.56 |
| $V_{max}$ (V) | 116.35 | 113.80 | 110.96 | 106.74 |
| Efficiency (%) | 96.71 | 96.82 | 95.83 | 94.09 |
| **P&O** | | | | |
| $P_{max}$ (W) | 338.47 | 324.01 | 305.68 | 285.18 |
| $V_{max}$ (V) | 115.92 | 113.42 | 110.16 | 106.40 |
| Efficiency (%) | 96.49 | 96.66 | 95.70 | 93.96 |

Table IV.2: The performance of each method under varying temperature conditions

Under variable temperature conditions, the DO algorithm consistently outperforms other MPPT techniques in key performance measures. It achieves the highest average tracking efficiency of 97.06%, demonstrating precise maximum power point (MPP) tracking across all temperature levels. The GWO algorithm follows closely with an average efficiency of 96.90%, reflecting strong adaptability to temperature variations. The PSO method attains an average efficiency of 95.86%, slightly higher than the traditional P&O method, which records 95.70%.

In terms of dynamic response, the DO algorithm exhibits the fastest adaptation to temperature changes, stabilizing at the new MPP more rapidly than GWO, PSO, and P&O. This performance is attributed to its effective balance between exploration and exploitation and its rapid convergence speed. Although GWO adapts relatively quickly, it remains marginally slower than DO, while PSO and P&O display progressively slower

responses with more noticeable oscillations during each temperature transition.

Regarding stability, the DO algorithm maintains minimal oscillations around the MPP at all temperature levels. GWO also demonstrates good stability, whereas PSO exhibits moderate oscillations, particularly during initial convergence. The P&O method shows the largest oscillatory behavior, resulting in higher steady-state errors, especially at elevated temperatures.

Table IV.3 summarizes the simulation results and compares the baseline performance of each method. Overall, the proposed MPPT algorithm consistently delivers superior results compared to both GWO and PSO across all tested conditions. In contrast, the P&O method exhibits the weakest performance, particularly in terms of tracking efficiency and its tendency to produce oscillations near the MPP.

| Criteria | DO | GWO | PSO | P&O |
|---|---|---|---|---|
| Robustness | Excellent, stable under irradiance and temperature variations | High, resilient to moderate changes | Moderate, responsive but less stable under rapid changes | Low, difficulty adapting to rapid change |
| Algorithmic Complexity | High, complex modeling and parameter tuning | Moderate–high, requires adaptive coefficients | Moderate, simple but parameter-sensitive | Low, easy to implement with low computational demand |
| Convergence Speed | Fast, adaptive exploration and exploitation and influenced by convergence coefficients such as $C$ and $q$ | Fast, adaptive exploration and exploitation and influenced by convergence coefficients such as $\vec{a}, r$ | Fast, convergence influenced by inertia ($\omega$) and acceleration coefficients | Medium, influenced by oscillates at MPP |
| Global Optimum Exploration | Strong, highly accurate under all conditions | Strong, slight degradation under rapid changes | Strong, avoids local traps effectively | Weak, often trapped in local optimum |
| Average Efficiency (%) | Highest, 94.72% (irradiance), 97.06% (temperature) | High, 94.52% and 96.90% | Moderate, 94.23% and 95.86% | Lowest, 93.82% and 95.70% |
| Oscillations around MPP | Minimal, highly stable | Minimal, minor oscillations | Minimal, mainly at initial convergence | High, significant oscillations |

Table IV.3: Comparison of Criteria for MPPT Methods

## IV.3 Improving HVDC-VSC performance with FFNN-based PI control under hybrid renewable energy operation

This section presents the application of FFNN for the control of an HVDC-VSC integrated with a HRES. Owing to the nonlinear behavior of renewable sources and the fast dynamics of power converters, conventional control techniques often struggle to ensure stability and efficient power exchange. To address this, an FFNN-based controller is employed to enhance DC-link voltage regulation, optimize active and reactive power flow, and improve overall system stability. The HRES studied combines PV and wind power generation via a common DC link, where power is conditioned through boost converters and regulated by the P&O MPPT method. The system interfaces with the utility grid through a VSI. The system is further interconnected with an HVDC-VSC transmission network, consisting of a rectifier on the sending side and an inverter on the receiving side, linked through DC cables. This architecture facilitates reliable and efficient long-distance power delivery to the receiving grid. Figure IV.6 illustrates the structure of the system studied, while Tables (Appendix B.3) and (Appendix B.4) present the values of the system parameters and all PI controller gains used in the system, respectively. Table (Appendix B.5) shows the specifications of the PV modules used. To validate the effectiveness of the proposed FFNN controller, a simulation of the system was performed in the MATLAB/Simulink environment.

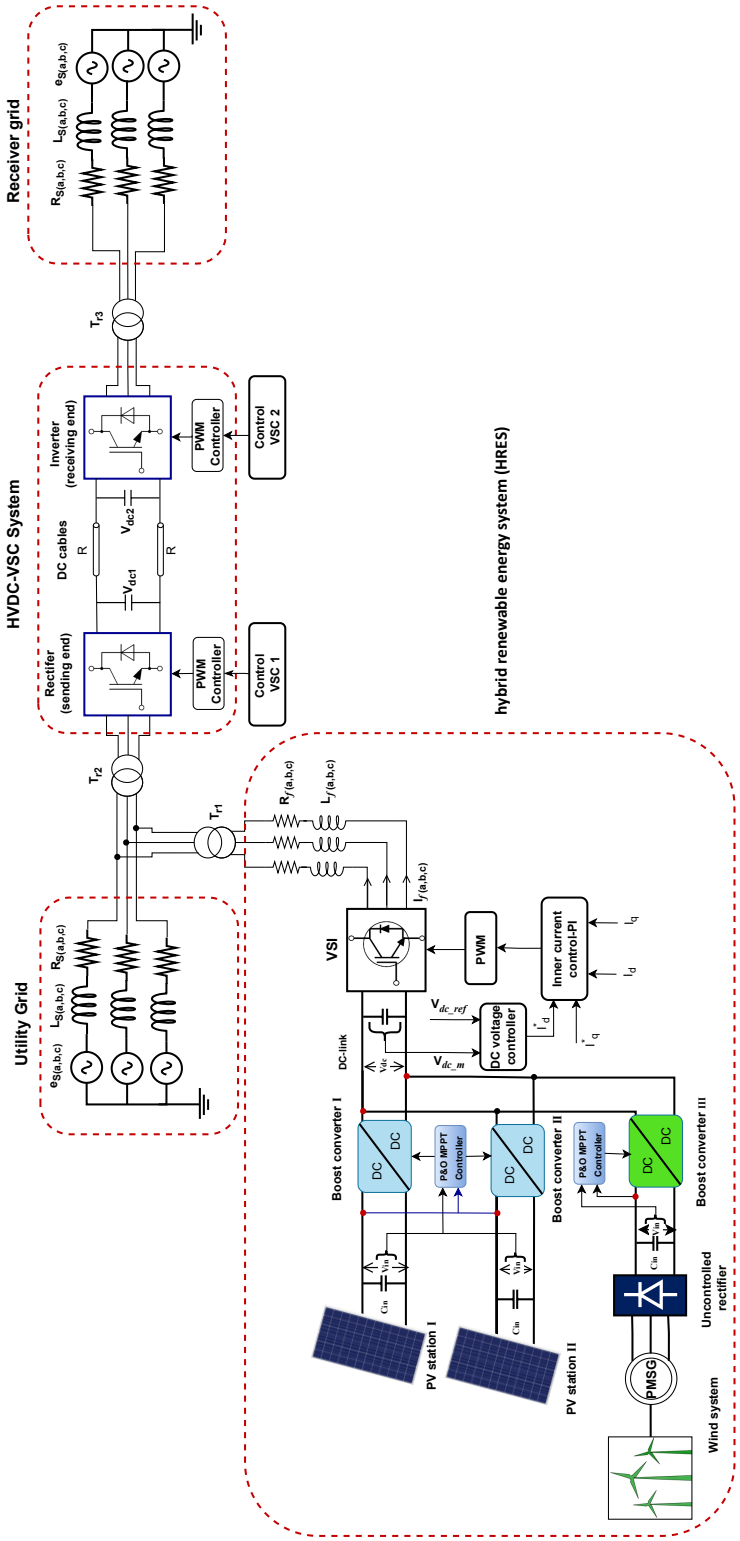


Figure IV.6: The overall structure of the system

### IV.3.1 Hybrid renewable energy injection in the utility grid

Several climatic scenarios were considered in the analysis of the hybrid energy system, incorporating variations in wind speed and fluctuations in solar irradiance, as illustrated in Figure IV.7.

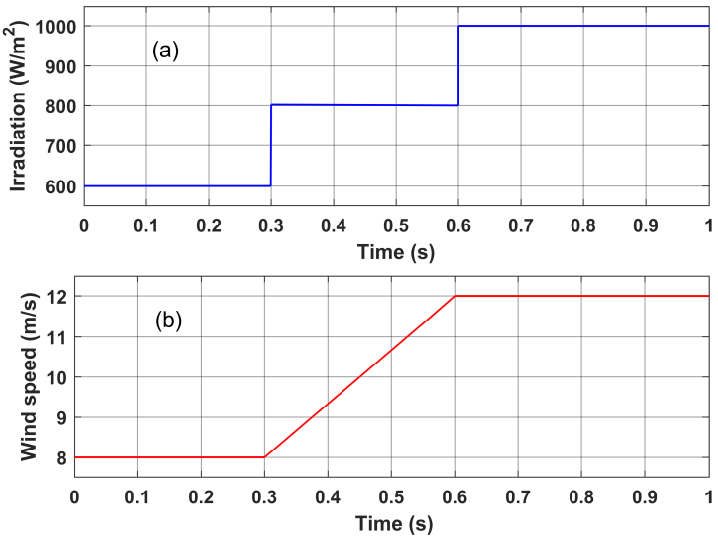


Figure IV.7: (a) Irradiation scenario; (b) Wind speed scenario

Figure IV.8 illustrates the power outputs of the PV and wind energy systems, both regulated through PI controllers. Furthermore, MPPT was implemented using the P&O method to manage the operation of the three boost converters integrated into the PV and wind subsystems, as shown in Figure IV.6. Figure (IV.8-a) demonstrates the dynamic response of the PV power output under different irradiation levels, whereas Figure (IV.8-b) presents the wind energy output corresponding to variations in wind speed.

One of the key performance indicators in hybrid renewable energy systems is the stability of the DC link voltage. Figure IV.9 illustrates the dynamic behavior of the DC link voltage under different climatic variations. The results confirm that the voltage effectively follows its reference value, particularly during transient operating conditions. This indicates the system's strong ability to sustain a nearly constant DC link voltage of 500 V, even in the presence of fluctuations in solar irradiance and wind speed, with only minimal voltage ripples observed.

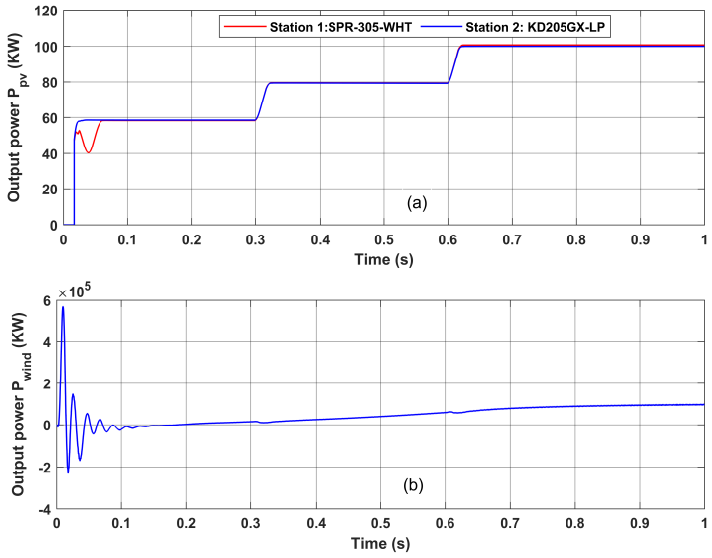


Figure IV.8: (a) PV power; (b) wind power

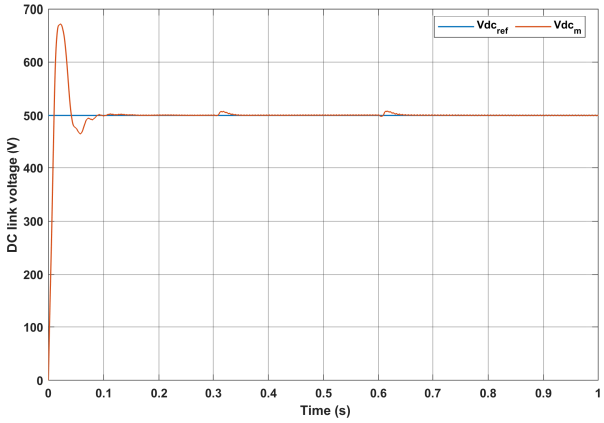


Figure IV.9: DC link voltage of HRES

Figure IV.10 shows the instantaneous active and reactive power supplied to the utility grid. The power profiles demonstrate smooth variations, with gradual increases and decreases that correspond to the energy delivered by the PV–wind hybrid system. Throughout the operation, only minor oscillations are observed, confirming stable power transfer.

Figures (IV.11-a) and (IV.11-b) represent the voltages and currents of the hybrid system at the PCC, respectively. The three-phase voltage between the lines remains balanced, sinusoidal, and stable. In contrast, temporary fluctuations in the three-phase currents injected can be observed due to sudden changes in radiation, temperature, and wind speed when the hybrid system begins to synchronize with the utility grid.

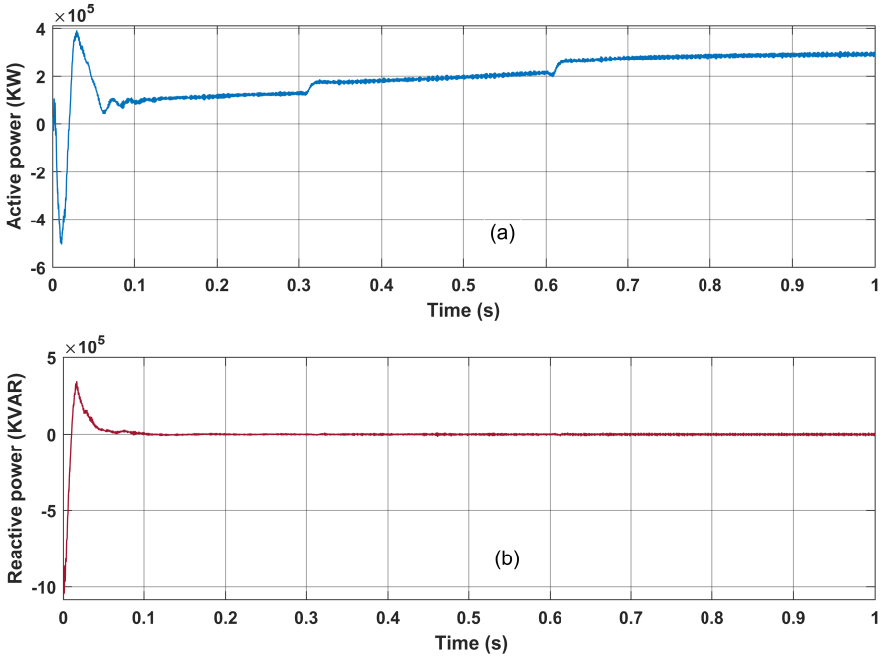


Figure IV.10: (a) instantaneous active power; (b) instantaneous reactive power

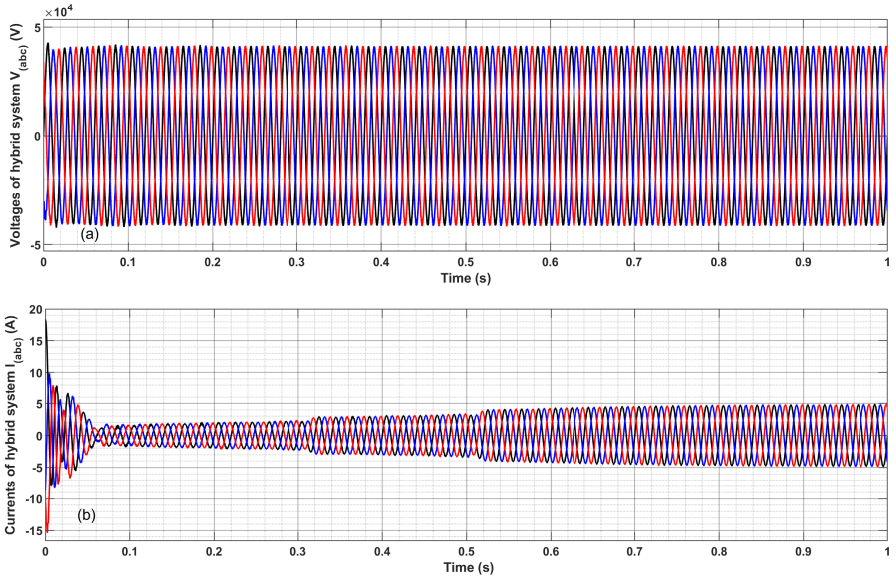


Figure IV.11: (a) Voltages and (b) Currents of the Integrated HRE Injected into the utility grid

### IV.3.2 Power injection in HVDC-VSC system

Figures IV.12 and IV.13 illustrate the comparative responses of current controllers $I_d$ and $I_q$, highlighting the enhanced dynamic behavior of the FFNN controller relative to

the conventional PI controller in the HRES integrated with the HVDC-VSC system. The FFNN demonstrates superior performance characterized by faster settling time, reduced overshoot, and significantly lower fluctuations during transient conditions. Moreover, the FFNN achieves smoother and more stable current regulation by effectively mitigating the high-frequency oscillations that persist under PI control. This improvement is primarily attributed to the adaptive learning capability of the FFNN, as further evidenced in Figures IV.14 and IV.15, which enables more efficient handling of nonlinearities and external disturbances compared to the PI controller.

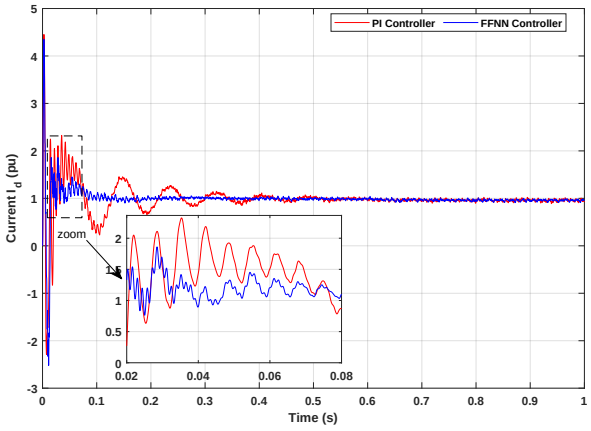


Figure IV.12: Current $I_d$ on the VSC 1 side

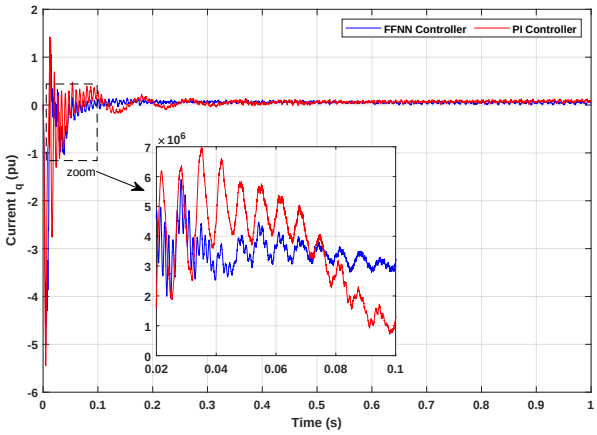


Figure IV.13: Current $I_q$ on the VSC 1 side

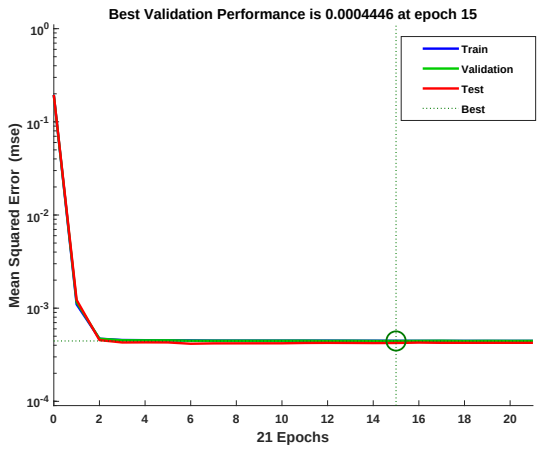


Figure IV.14: Training performance of $I_d$ current under FFNN control

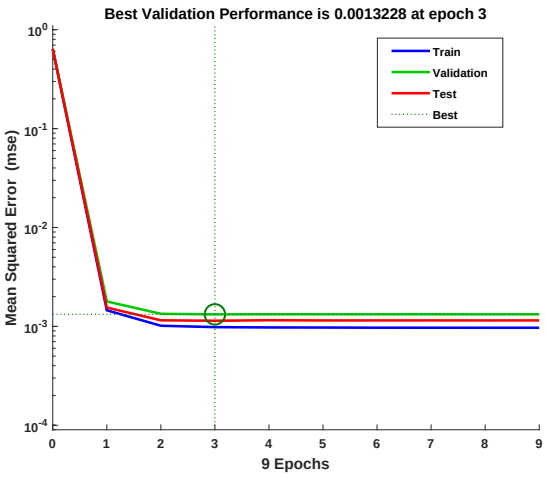


Figure IV.15: Training performance of $I_q$ current under FFNN control

The performance of the DC link voltage ($V_{\mathrm{dc1}}$) at the VSC1 terminal of the HVDC-

VSC system is shown in Figure IV.16, illustrating the superior control capability of the FFNN controller compared to the conventional PI controller. The FFNN demonstrates a faster voltage regulation response, characterized by reduced oscillations during transient conditions. At the same time, the PI controller exhibits a pronounced overshoot and an extended settling time, which may impose additional stress on transformer components. Furthermore, FFNN ensures that the DC link voltage closely tracks the reference value of 3000V with minimal steady-state error, thereby enhancing overall system stability even under rapid dynamic variations. Figure IV.17 presents the training performance of the FFNN for regulating $V_{\mathrm{dc}}$.

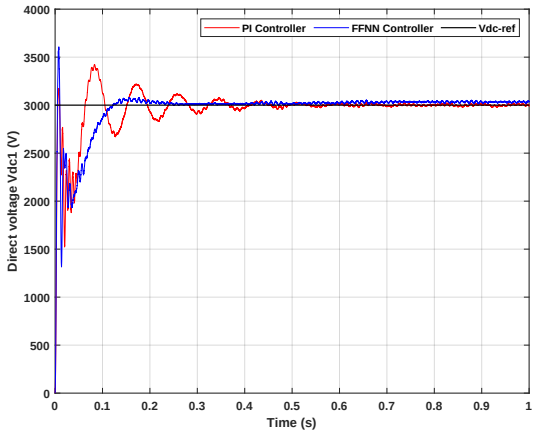


Figure IV.16: The DC link voltage on the VSC 1 side

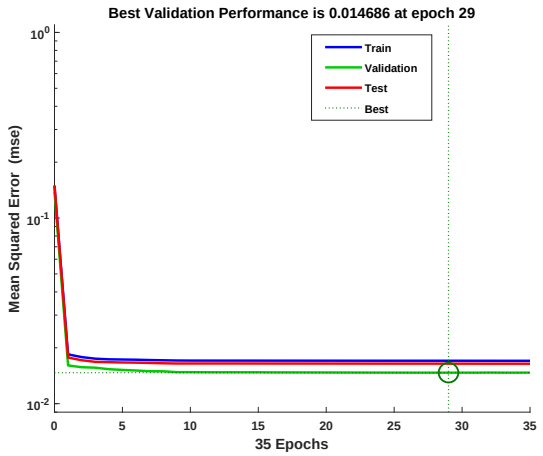


Figure IV.17: The training performance for $V_{dc}$ current under FFNN control

A bipolar HVDC-VSC system consists of two conductors, namely the positive and negative poles, referenced to a common ground or metallic return path, with each pole carrying half of the total DC voltage. This configuration reduces insulation stress, enhances transmission efficiency, and enables continuous operation in monopolar mode in the event of a pole fault, thereby improving system reliability and minimizing current return through the earth. Figures IV.18 and IV.19 illustrate the positive and negative pole voltages of the HVDC-VSC system, respectively, under the regulation of an FFNN-based controller compared with a conventional PI controller. The results indicate that the FFNN achieves faster settling responses, reduced oscillations, and closer voltage tracking to the reference in

both poles. In contrast, the PI controller exhibits larger overshoots and slower convergence. These findings demonstrate the dynamic and steady-state performance of the FFNN in managing nonlinearities and rapid system variations, ultimately reinforcing the robustness, efficiency, and stability of bipolar HVDC transmission systems.

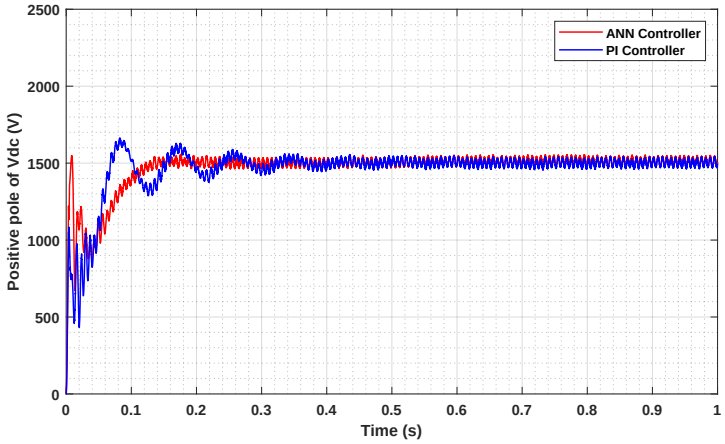


Figure IV.18: The DC link voltage of the positive pole

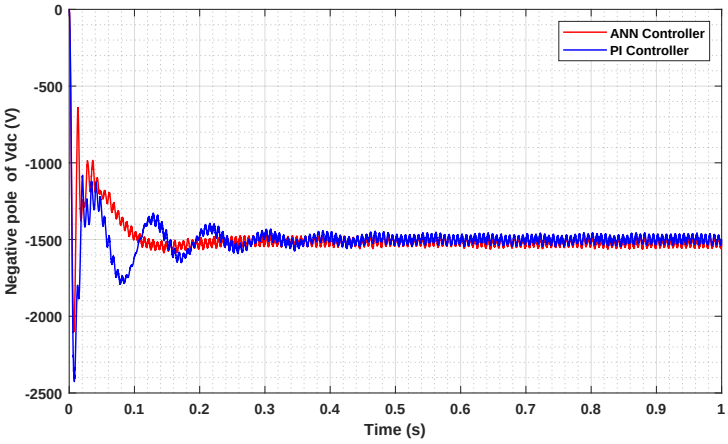


Figure IV.19: The DC link voltage of the negative pole

Figures (IV.20-a) and (IV.20-b) present the active power responses of VSC1 and VSC2, respectively. The results demonstrate that the FFNN controller outperforms the conventional PI controller by exhibiting faster damping of oscillations and reduced overshoot during transient conditions. For VSC1, the FFNN achieves smaller peak deviations and quicker stabilization compared to the PI controller. Similarly, in the case of VSC2, the FFNN controller effectively suppresses oscillatory behavior and ensures a more stable power

exchange within a shorter time frame. Furthermore, Figures (IV.20-a) and (IV.20-b) depict the reactive power responses of VSC1 and VSC2, respectively.

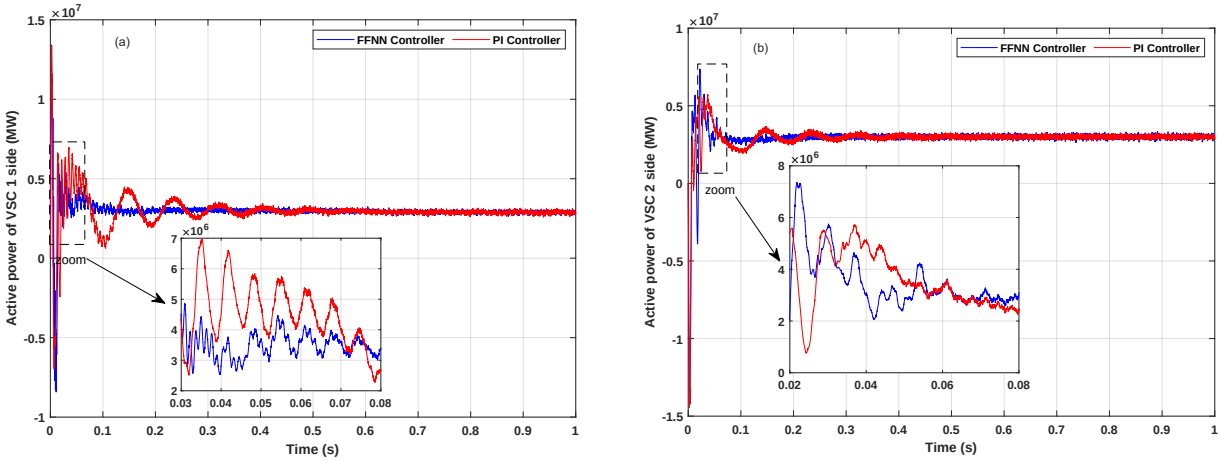


Figure IV.20: Instantaneous active power for VSCs: (a) side 1, (b) side 2

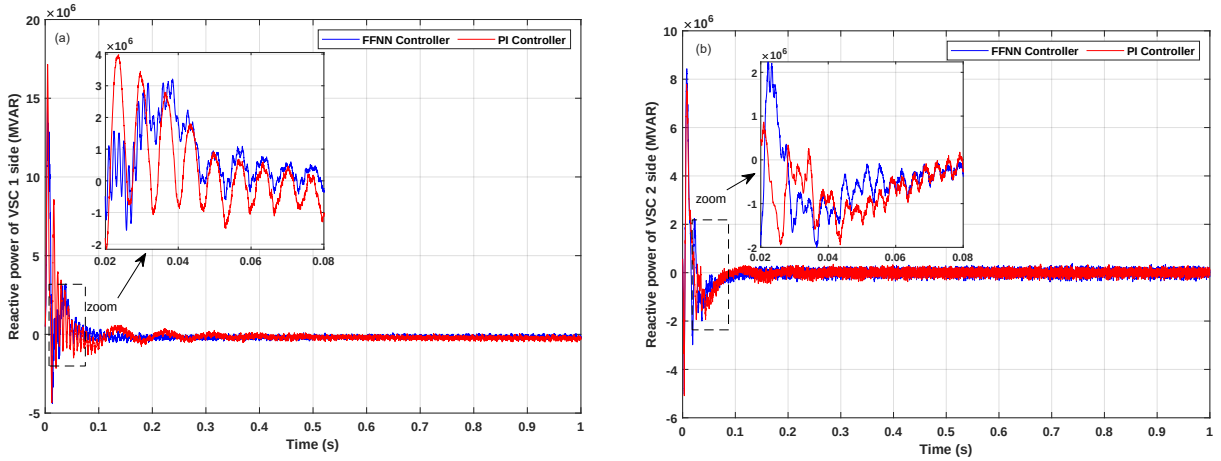


Figure IV.21: Instantaneous reactive power for VSCs: (a) side 1, (b) side 2

## IV.4 Fault analysis of HVDC-VSC transmission system

Understanding the behavior of faults in HVDC-VSC systems is essential for ensuring reliable and secure power transmission. Unlike conventional AC networks, VSC-HVDC links exhibit unique fault dynamics due to their low line inductance, fast transient response, and the absence of natural current zero crossings. These characteristics cause fault currents

to rise rapidly and impose severe stress on converter submodules, DC cables, and protection devices [113]. An analysis of pole-to-pole, pole-to-ground, and high-impedance faults is therefore necessary to assess system vulnerabilities. This section provides an analysis and simulation of the mechanisms, behavior, and operational consequences of pole-to-pole and pole-to-ground fault scenarios for HVDC-VSC transmission systems.

## IV.4.1 Pole to pole short circuit fault

A pole-to-pole fault arises when a direct electrical connection, often caused by insulation failure or physical contact, forms between the positive and negative conductors of the DC transmission line. Although such faults occur infrequently, their impact can be severe, leading to rapid escalation of current, damage to converter power switches, and complete interruption of power transfer. Upon detection, immediate blocking of the converter valves is required, followed by the isolation of the grid-side interface through AC circuit breakers to prevent further propagation of the disturbance. Once the faulted section is cleared, system restoration procedures can be initiated to return to normal operation [114]. The evolution of a pole-to-pole fault typically proceeds through three distinct transient stages before reaching a new steady-state condition, and these stages are examined in detail in the following subsection.

### IV.4.1.1 Stage of capacitor discharging

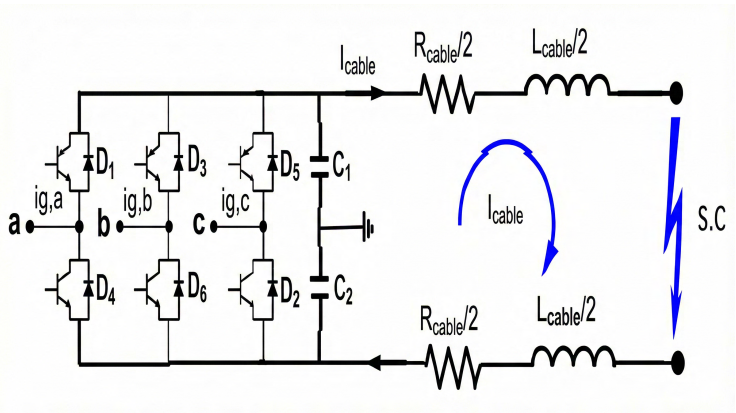


Figure IV.22: Circuit equivalent to pole-to-pole fault in DC

When a pole-to-pole short circuit occurs, it triggers the immediate discharge of the DC link capacitor into the transmission line. The specific trajectory of this free transient response is dictated by the electrical parameters of the line itself. The circuit essentially functions as a second-order RLC system—comprising the capacitor, the transmission line's inductance, and the total resistance, which includes the fault path as shown in figure IV.22. This dynamic relationship is modeled by:

$$i_{\text{cable}} = I_0 e^{-(R_{\text{cable}}/L_{\text{cable}})t} \tag{IV.1}$$

Where $R_{cable}$ and $L_{cable}$ represent the resistive and inductive properties of the line up to the fault location, and $I_0$ indicates the current value at the moment of the short circuit.

#### IV.4.1.2 Stage of diode freewheel

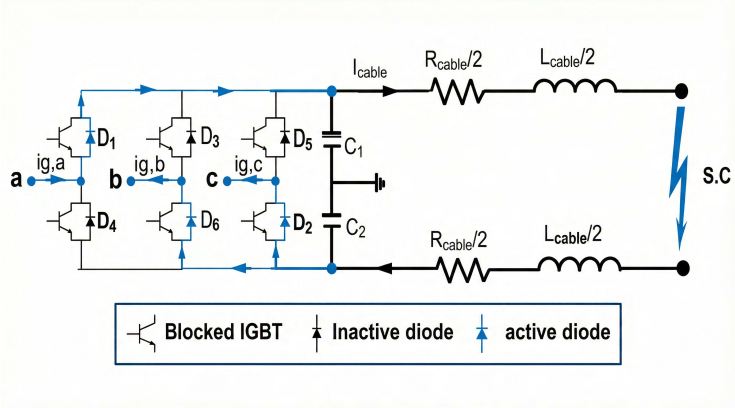


Figure IV.23: Circuit equivalent of diode freewheel

Upon reducing the DC link voltage below the grid phase voltage, the system enters the diode freewheeling stage. As the capacitor voltage approaches zero, the IGBTs are blocked for protection purposes. This action converts the VSC into a three-phase diode rectifier configuration, as shown in figure IV.23, creating a path for the grid to supply the fault current continuously.

#### IV.4.1.3 Stage of grid feeding

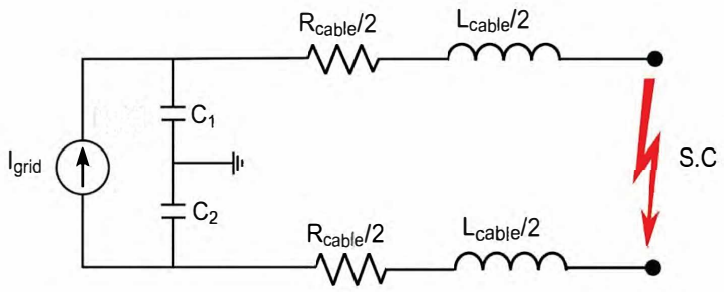


Figure IV.24: Circuit equivalent of capacitor recharging

The grid side feeding Stage represents the final, steady-state period of a DC pole-to-pole fault in a VSC-HVDC system, occurring after the initial energy stored in the DC link capacitor has been fully discharged. With the DC voltage near zero and the IGBTs blocked for protection, the VSC effectively operates as an uncontrolled three-phase diode rectifier, where the anti-parallel diodes become the conductive path (This makes it a source of the current that feeds the fault, as shown in Figure IV.24. The AC grid sustains the high-magnitude fault current, which is limited primarily by the AC-side impedance (reactors and transformers). This sustained current imposes severe thermal stress on the components and must be actively interrupted by a specialized DC Circuit Breaker.

The results shown in Figures IV.25, IV.26, and IV.27 were obtained by simulating the behavior of the VSC-HVDC transmission system when a pole to pole short circuit fault.

When a short circuit fault is applied at t=0.4s as shown in Figure IV.25, the DC-link voltage rapidly collapses to near-zero. During the capacitor discharge stage, the voltage drops sharply as stored energy depletes into the fault path. Once discharged, the voltage remains clamped at approximately zero throughout the diode freewheeling stage due to blocked converter valves and the absence of active voltage support. The grid feeding stage shows minimal voltage recovery through AC rectification via converter diodes, which is weak and unstable. This demonstrates that pole-to-pole faults cause irreversible voltage collapse without rapid DC protection.

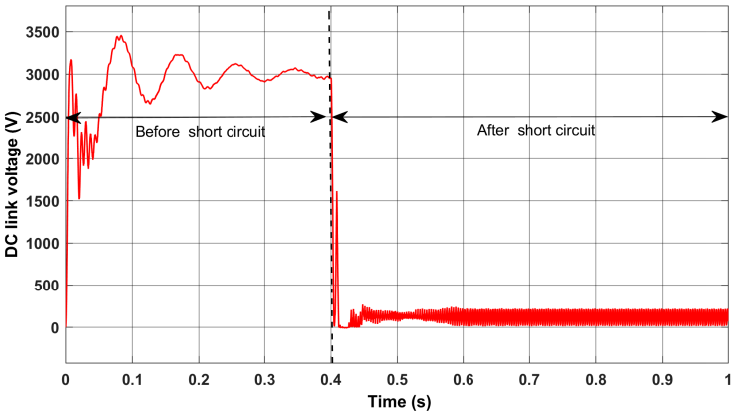


Figure IV.25: DC link voltage of pole-to-pole short circuit fault

The DC-link current shows a severe transient upon fault initiation at t=0.4s, as shown in Figure IV.26, characterized by a steep rise during capacitor discharge as stored energy rapidly releases into the low-impedance fault path, producing peak current with minimal current limitation. As capacitor energy depletes, the current transitions to the diode freewheeling stage, where it decays gradually through release of inductive energy from DC reactors and transmission lines via the converter's antiparallel diodes. Subsequently, the grid feeding stage sustains a steady-state fault current as the AC grid continuously supplies current through the converter diodes functioning as an uncontrolled rectifier.

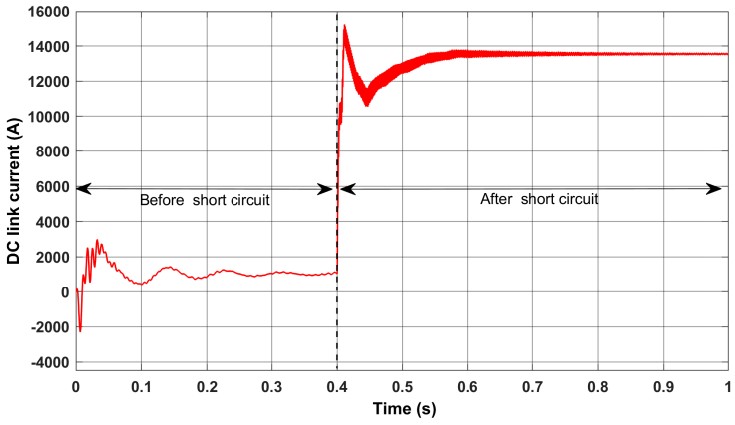


Figure IV.26: DC link current of pole-to-pole short circuit fault

The AC-side waveforms demonstrate strong DC-AC coupling during the fault event as shown in Figure IV.27. At fault initiation, grid currents surge sharply as the converter transitions from controlled operation to an uncontrolled diode bridge, while grid voltages

sag due to the large fault current and impedance voltage drops. During diode freewheeling, elevated AC currents persist through intermittent diode conduction, and the grid feeding stage sustains high currents and depressed voltages as the AC system continuously supplies power to the DC fault. Without DC-side protection, the pole-to-pole fault directly propagates disturbances into the AC grid, jeopardizing system stability and equipment safety.

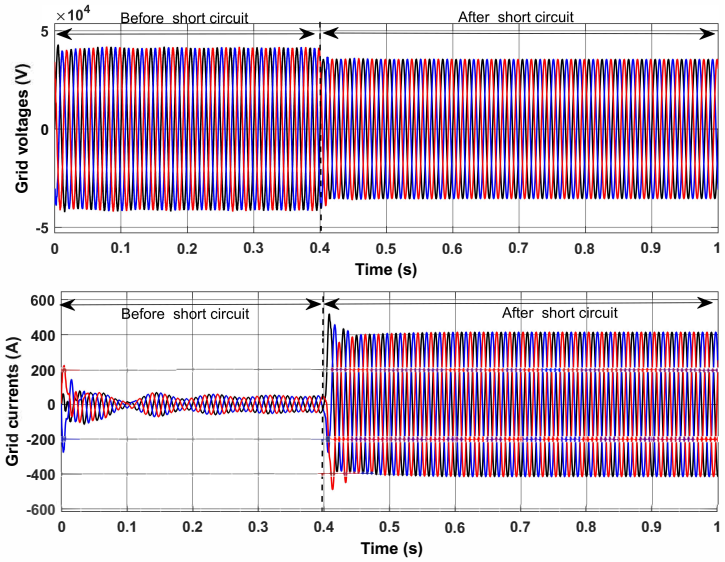


Figure IV.27: Grid voltages and grid currents of pole-to-pole short circuit fault

### IV.4.2 Pole to ground short circuit fault

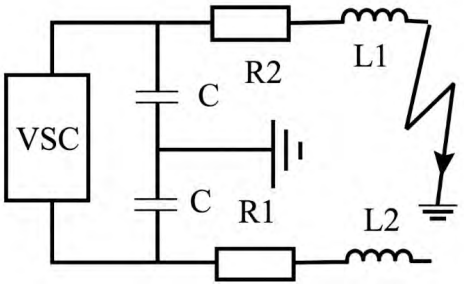


Figure IV.28: Circuit equivalent of DC line-to-ground fault

A DC line-to-ground fault in HVDC systems occurs when insulation fails, creating an additional grounding point that forms a ground loop with the transformer neutral and DC-link midpoint. The fault is modeled using $\pi$-equivalent resistances and inductances

between the VSC and the fault location as shown in figure IV.28. The sharp rise in current forces the IGBTs to block, allowing current to flow through the freewheeling diodes [115]. The fault evolves in three stages:

- **Capacitor discharge stage:** the short-circuit current is mainly the discharge of the DC capacitors, since the DC voltage is still higher than the AC phase voltage.

- **Grid-feeding stage:** once the DC voltage drops below the AC voltage, the AC grid feeds the fault through the diodes and charges the line capacitor.

- **Voltage-recovery stage:** capacitor voltages redistribute, and the DC voltage gradually returns to normal.

Based on the results obtained for the simulation of the fault between the pole and the ground shown in Figures IV.29, IV.30, and IV.31, the dynamics of the system exhibit completely different behavior compared to the fault between the poles, characterized by temporary disturbance rather than complete collapse of the system.

Upon fault inception at 0.4 s as shown in Figure IV.29, the capacitor discharge stage causes the voltage to drop from 3000 V to approximatey 1700 V, a partial rather than complete collpse. This partial response occurs because the fault affects only one pole, preserving the partial potential difference between poles. During the subsequent voltage recovery stage, DC voltage rapidly rebounds to its pre-fault nominal value of 3000 V, confirming the capacitor remains functional. The system redistributes potential, with the healthy pole voltage rising relative to ground (often doubling) while maintaining pole-to-pole voltage sufficient for continued operation.

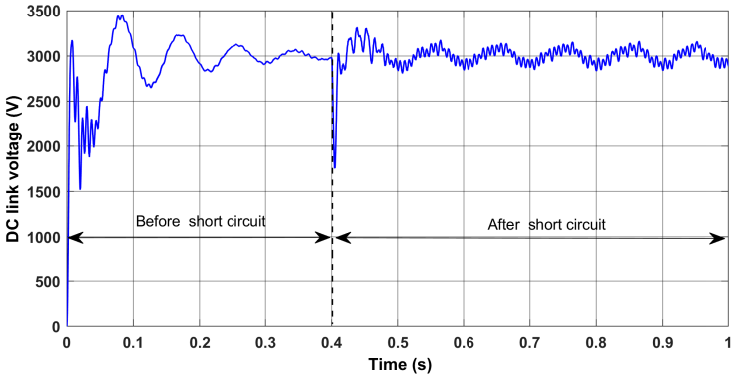


Figure IV.29: DC link voltage of pole-to-ground short circuit fault

The capacitor discharge stage is marked by an immediate, high-frequency surge in current, peaking at approximately 4500 A at 0.4 s, as shown in Figure IV.30. This spike represents the rapid release of stored energy from the capacitor of the faulted pole into the ground impedance. However, unlike the sustained high current seen in pole-to-pole faults, the current here quickly decays. As the voltage recovers, the current oscillations dampen, indicating the transition out of the discharge phase. The current eventually settles back into a stable oscillation around its nominal value, signifying that the converter has successfully ridden through the transient and is not feeding a continuous, uncontrollable short circuit current.

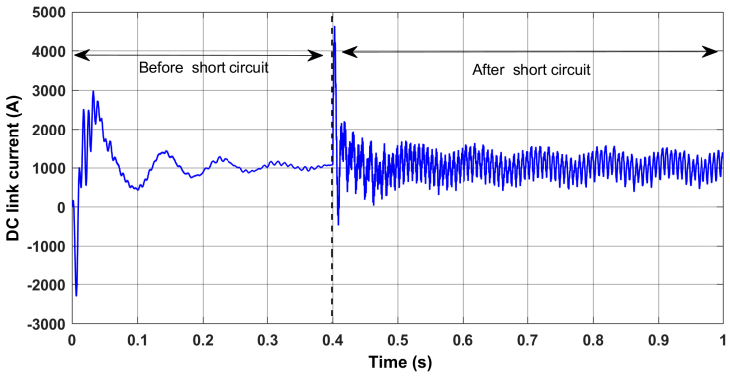


Figure IV.30: DC link current of pole-to-ground short circuit fault

The AC side dynamics illustrate the grid feeding stage, where the AC grid interacts with the DC fault disturbance. At the instant of the fault 0.4s, the grid currents exhibit a momentary transient distortion as shown in Figure IV.31, peaking and oscillating as the

grid supplies the initial surge of energy required by the fault and the subsequent recharging of the DC capacitors. Crucially, the grid voltages remain robust and do not collapse. The grid currents quickly stabilize after the initial perturbation, returning to a steady-state pattern. This behavior demonstrates that during a pole-to-ground fault, the grid provides temporary feedback to rebalance the DC link power, allowing the system to recover its operating point.

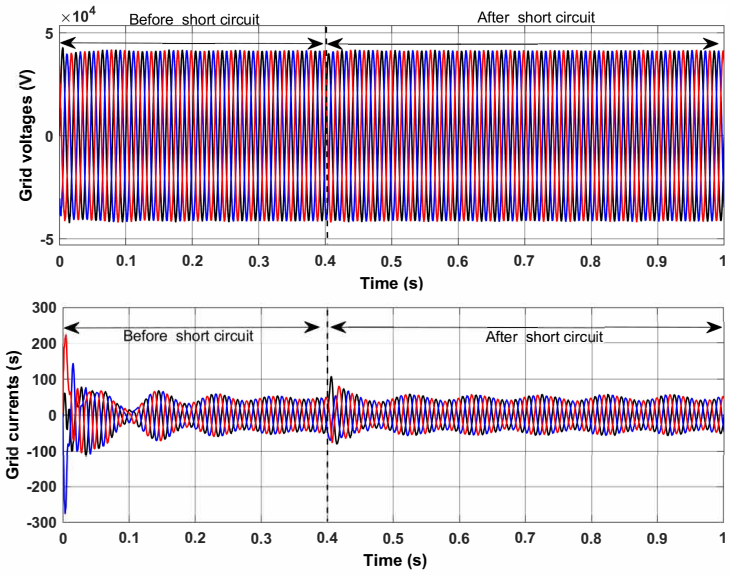


Figure IV.31: Grid voltages and grid currents of pole-to-ground short circuit fault

# IV.5 Conclusion

This chapter presented a comprehensive analysis of advanced control and optimization methods for enhancing renewable energy systems. In the first part, the dandelion-inspired optimization (DO) algorithm was applied to the MPPT of PV systems. Simulation results demonstrated that the DO algorithm outperforms conventional methods such as P&O, PSO, and GWO in terms of convergence speed, tracking efficiency, and robustness under varying irradiance and temperature conditions. The findings highlight the effectiveness of bio-inspired optimization in addressing the dynamic challenges of PV energy harvesting.

In the second part, the performance of an HVDC-VSC transmission system integrated with hybrid renewable energy was studied using an FFNN-based controller. Compared to a

traditional PI controller, FFNN showed superior performance in DC-link voltage regulation and active and reactive power flow management, especially during transient conditions. The learning capability of the neural network enabled more accurate handling of nonlinear dynamics, resulting in faster response, reduced overshoot, and improved system stability.

In general, the results confirm that combining nature-inspired optimization algorithms and intelligent neural control provides a powerful framework for enhancing the efficiency and reliability of renewable energy systems and HVDC-VSC transmission systems. These methods not only enhance the extraction of maximum energy from renewable sources, but also ensure stable and efficient energy delivery across long-distance transmission networks. Thus, the methods explored in this chapter represent promising solutions for integrating renewable energy with HVDC-VSC systems in the future within modern smart grids.

In the third part, the behavior of the HVDC-VSC transmission system was analyzed under the application of a short-circuit fault for both pole-to-pole and pole-to-ground. It is concluded that in this type of faults, the system configuration changes in time, it starts with RLC circuit and then transformed to a three phase diode bridge and end with a current source supply the fault. The line-to-ground fault leads to the unbalance of DC voltage which is difficult to rebalance; for line temporary line-to-ground faults, the rebalance of capacitors can be realized by using high impedance grounding system. In this recovery method, the discharging current is very small so that the voltage of the capacitor can maintain without any overcurrent stress. The over-current after a line-to-ground fault is not very large, so a line-to-ground is not serious fault.

# General conclusion

This thesis has investigated the modeling, control, and optimization of a hybrid renewable energy system composed of offshore wind generation and photovoltaic power, integrated into modern grids through VSC-HVDC technology. The research was driven by the growing global demand for sustainable energy and the increasing need to transmit power from remote generation sites to urban load centers in a reliable and efficient manner.

The study began with an overview of renewable energy development and highlighted the critical role of HVDC-VSC systems in supporting large-scale integration of wind and solar resources. Owing to their ability to independently control active and reactive power and reinforce AC grids, VSC-HVDC links were shown to be a flexible and resilient option for future transmission networks.

Mathematical models of the PV system, PMSG-based wind turbine, and HVDC-VSC link were then established, providing the basis for control and simulation studies. Advanced control strategies were introduced to optimize energy extraction and ensure stability. For the PV system, MPPT algorithms such as P&O, PSO, GWO, and the dandelion-inspired optimization (DO) were evaluated, with the DO algorithm demonstrating superior convergence and robustness under dynamic conditions. For the wind turbine, a lookup table method was employed to regulate output power effectively. Grid-side control was achieved using dq-axis control and SVPWM modulation, improving inverter utilization and reducing harmonic distortion.

To enhance performance further, intelligent control techniques were applied. An FFNN-based controller for the VSC-HVDC system demonstrated improved DC-link regulation and power flow management compared to conventional PI control, especially during transients. The integration of intelligent optimization and neural control thus enabled faster response, reduced overshoot, and enhanced overall system stability.

Extensive simulations validated the effectiveness of the proposed methods under a range of conditions, including irradiance variations. The results confirm that the combined use of hybrid renewable systems, intelligent MPPT techniques, and advanced VSC-HVDC

control ensures high efficiency, robust operation, and improved fault tolerance. These findings underline the potential of the proposed framework for future smart grids, where reliability, stability, and energy efficiency are paramount.

**Future Work**

Future research can expand upon the findings of this thesis in the following directions:

- Extended power quality analysis: Investigating the system's performance under voltage sags, swells, and frequency variations.
- Multi-terminal HVDC systems: Applying the proposed methods to multi-terminal VSC-HVDC networks to support large-scale renewable deployment.
- Hybrid renewable diversification: Integrating additional renewable sources, such as hydropower or biomass, to create more resilient hybrid systems.
- Advanced intelligent control: Exploring deep learning, reinforcement learning, and adaptive fuzzy controllers for greater adaptability and fault tolerance.
- Experimental validation: Conducting hardware-in-the-loop (HIL) and real-time prototype testing to confirm practical feasibility.

# Bibliography


[1] Md Ismail Hossain, Md Shafiullah, Fahad A Al-Sulaiman, and Mohammad A Abido. Comprehensive analysis of pv and wind energy integration into mmc-hvdc transmission network. *Sustainability*, 15(1):253, 2022.

[2] Guangsheng Pan, Xi Huang, and Jie Liu. System control strategies for renewable energy-integrating grids via voltage source converter-based high-voltage direct current technology. In *Actuators*, volume 13, page 505. MDPI, 2024.

[3] Injila Sajid, Ayushi Gautam, Adil Sarwar, Mohd Tariq, Hwa-Dong Liu, Shafiq Ahmad, Chang-Hua Lin, and Abdelaty Edrees Sayed. Optimizing photovoltaic power production in partial shading conditions using dandelion optimizer (do)-based mppt method. *Processes*, 11(8):2493, 2023.

[4] Vaclav Smil. *Energy and civilization: a history*. MIT press, 2018.

[5] John Perlin. *From space to earth: the story of solar electricity*. Earthscan, 1999.

[6] Daniel Yergin. *The quest: Energy, security, and the remaking of the modern world*. Penguin, 2012.

[7] Mark Z Jacobson and Mark A Delucchi. Providing all global energy with wind, water, and solar power, part i: Technologies, energy resources, quantities and areas of infrastructure, and materials. *Energy policy*, 39(3):1154–1169, 2011.

[8] Geoffrey G Jones and Loubna Bouamane. " power from sunshine": A business history of solar energy. *Harvard Business School Working Paper Series*, 2012.

[9] IEA IEA. Renewable energy market update 2021. IEA Paris, France, 2021.

[10] Akshita Gupta, Arun Kumar, and Dheeraj Kumar Khatod. Optimized scheduling of hydropower with increase in solar and wind installations. *Energy*, 183:716–732, 2019.

[11] Daniel Weisser. A guide to life-cycle greenhouse gas (ghg) emissions from electric supply technologies. *Energy*, 32(9):1543–1559, 2007.

[12] Victoria J Fabry, Brad A Seibel, Richard A Feely, and James C Orr. Impacts of ocean acidification on marine fauna and ecosystem processes. *ICES Journal of Marine Science*, 65(3):414–432, 2008.

[13] Andrew CK Lee and Ravi Maheswaran. The health benefits of urban green spaces: a review of the evidence. *Journal of public health*, 33(2):212–222, 2011.

[14] Ricardo Raineri Bernai. Renewable energy sources and climate change mitigation, special report of the intergovernmental panel on climate change (ipcc), 2013.

[15] Kirk R Smith and Sameer Akbar. Health-damaging air pollution: A matter of scale. In *Air pollution and health in rapidly developing countries*, pages 21–34. Routledge, 2012.

[16] International Energy Agency. *Energy Security and Climate Policy-Assessing Interactions*. OECD Publishing, 2007.

[17] Richard Burrett, Corrado Clini, Robert Dixon, Michael Eckhart, Mohamed El-Ashry, Deepak Gupta, Amal Haddouche, David Hales, Kirsty Hamilton, Chatham House, et al. Renewable energy policy network for the 21st century. *REN21 Renewables Global Status Report*, 2009.

[18] Ryan Wiser, Karen Jenni, Joachim Seel, Erin Baker, Maureen Hand, Eric Lantz, and Aaron Smith. Forecasting wind energy costs and cost drivers: the views of the world's leading experts. 2016.

[19] Benjamin K Sovacool. Valuing the greenhouse gas emissions from nuclear power: A critical survey. *Energy Policy*, 36(8):2950–2963, 2008.

[20] Thomas P. Hughes. *Networks of Power: Electrification in Western Society, 1880-1930*. Johns Hopkins University Press, 1983.

[21] Lorand Szabo, Karoly Agoston Biro, Cosmina Nicula, and Florin Jurca. Useful simulation tool for induction generators used in wind power plants. In *2007 International Conference on Clean Electrical Power*, pages 574–579. IEEE, 2007.

[22] Global Wind Energy Council. Global wind report 2021, 2021.

[23] WindEurope. Wind energy in europe in 2021 statistics and the outlook for 2022-2026, 2022.

[24] International Energy Agency. Global wind power outlook, 2021.

[25] The International Renewable Energy Agency. Renewable energy statistics 2020, 2023.

[26] International Renewable Energy Agency. Renewable power generation costs in 2020, 2021.

[27] Ricardo A Marques Lameirinhas, João Paulo N Torres, and João P de Melo Cunha. A photovoltaic technology review: History, fundamentals and applications. *Energies*, 15(5):1823, 2022.

[28] John Perlin. *Let it shine: the 6,000-year story of solar energy*. New World Library, 2022.

[29] Himanshu J Bahirat, Bruce A Mork, and Hans Kr Høidalen. Comparison of wind farm topologies for offshore applications. In *2012 IEEE Power and Energy Society General Meeting*, pages 1–8. IEEE, 2012.

[30] Dirk Van Hertem, Oriol Gomis-Bellmunt, and Jun Liang. *HVDC grids: for offshore and supergrid of the future*. John Wiley & Sons, 2016.

[31] Anne Berit Mogstad, Marta Molinas, et al. Power collection and integration on the electric grid from offshore wind parks. In *Nordic Workshop on Power and Industrial Electronics (NORPIE/2008), June 9-11, 2008, Espoo, Finland*. Helsinki University of Technology, 2008.

[32] Stefan Lundberg. Evaluation of wind farm layouts. *EPE journal*, 16(1):14–21, 2006.

[33] Pavol Bauer, Sjoerd WH De Haan, CR Meyl, and Jan TG Pierik. Evaluation of electrical systems for offshore windfarms. In *Conference Record of the 2000 IEEE Industry Applications Conference. Thirty-Fifth IAS Annual Meeting and World Conference on Industrial Applications of Electrical Energy (Cat. No. 00CH37129)*, volume 3, pages 1416–1423. IEEE, 2000.

[34] Amina AZIZI. *Modélisation et optimisation d'un système de production d'énergie photovoltaïque avec un système de stockage hybride*. PhD thesis, Université de Annaba-Badji Mokhtar, 2019.

[35] Majid Jamil, M Rizwan, and Dwarkadas Pralhaddas Kothari. *Grid Integration of Solar Photovoltaic Systems*. Crc Press, 2017.

[36] Soham Deshpande and NR Bhasme. A review of topologies of inverter for grid connected pv systems. *2017 Innovations in Power and Advanced Computing Technologies (i-PACT)*, pages 1–6, 2017.

[37] S Ali Khajehoddin, Alireza Bakhshai, and Praveen Jain. A novel topology and control strategy for maximum power point trackers and multi-string grid-connected pv inverters. In *2008 Twenty-Third Annual IEEE Applied Power Electronics Conference and Exposition*, pages 173–178. IEEE, 2008.

[38] Jing Yuan, Frede Blaabjerg, Yongheng Yang, Ariya Sangwongwanich, and Yanfeng Shen. An overview of photovoltaic microinverters: Topology, efficiency, and reliability. In *2019 IEEE 13th International Conference on Compatibility, Power Electronics and Power Engineering (CPE-POWERENG)*, pages 1–6. IEEE, 2019.

[39] Michael P Bahrman. Overview of hvdc transmission. In *2006 IEEE PES power systems conference and exposition*, pages 18–23. IEEE, 2006.

[40] Christoph Buchhagen, Christian Rauscher, Andreas Menze, and Jochen Jung. Borwin1-first experiences with harmonic interactions in converter dominated grids.

In *International ETG Congress 2015; Die Energiewende-Blueprints for the new energy age*, pages 1–7. VDE, 2015.

[41] Andrei Stan, Sorina Costinaș, and Georgiana Ion. Overview and assessment of hvdc current applications and future trends. *Energies*, 15(3):1193, 2022.

[42] Willis Long and Stig Nilsson. Hvdc transmission: yesterday and today. *IEEE Power and Energy Magazine*, 5(2):22–31, 2007.

[43] André Bodin. Hvdc light®-a preferable power transmission system for renewable energies. In *Proceedings of the 2011 3rd International Youth Conference on Energetics (IYCE)*, pages 1–4. IEEE, 2011.

[44] Elkhatib Kamal. Stabilization of large power systems using vsc–hvdc and fuzzy anti-windup subject to input constraints. *Electric Power Components and Systems*, 48(6-7):572–588, 2020.

[45] Mark Venables. Back to its roots [hvdc]. *Power Engineer*, 21(6):14–19, 2007.

[46] Chan-Ki Kim, Vijay K Sood, Gil-Soo Jang, Seong-Joo Lim, and Seok-Jin Lee. *HVDC transmission: power conversion applications in power systems*. John Wiley & Sons, 2009.

[47] Pedro Rodriguez and Kumars Rouzbehi. Multi-terminal dc grids: challenges and prospects. *Journal of Modern Power Systems and Clean Energy*, 5(4):515–523, 2017.

[48] RL Sellick and Markus Åkerberg. Comparison of hvdc light (vsc) and hvdc classic (lcc) site aspects, for a 500mw 400kv hvdc transmission scheme. In *10th IET international conference on AC and DC power transmission (ACDC 2012)*, pages 1–6. IET, 2012.

[49] Samy Akkari. *Contrôle d'un système multi-terminal HVDC (MTDC) et étude des interactions entre les réseaux AC et le réseau MTDC.— Theses. fr*. PhD thesis, Université Paris-Saclay (ComUE), 2016.

[50] Jiuping Pan, Reynaldo Nuqui, Kailash Srivastava, Tomas Jonsson, Per Holmberg, and Ying-Jiang Hafner. Ac grid with embedded vsc-hvdc for secure and efficient power delivery. In *2008 IEEE Energy 2030 Conference*, pages 1–6. IEEE, 2008.

[51] Ahmed Elserougi, Ahmed Mohamed Massoud, Ayman Samy Abdel-Khalik, and Shehab Ahmed. Three-wire bipolar high-voltage direct current line using an existing single-circuit high-voltage alternating current line for integrating renewable energy sources in multiterminal dc networks. *IET Renewable Power Generation*, 10(3):370–379, 2016.

[52] Nemanja Savić and Vladimir Katić. Overview of the configuration and power converters in high voltage direct current transmission systems. *Kladovo, Srbija*, 2017.

[53] Gianluigi Migliavacca. *Advanced technologies for future transmission grids*. Springer Science & Business Media, 2012.

[54] Lasantha Meegahapola, Siqi Bu, and Mingchen Gu. *Hybrid AC/DC Power Grids: Stability and Control Aspects*. Springer, 2022.

[55] Cherif Kellal, Mazouz Lakhdar, Abdellah Kouzou, and Abdelkdaer Ouacel. An ann-based maximum power point tracking using dc/dc boost converter for pv system. In *2023 1st International Conference on Renewable Solutions for Ecosystems: Towards a Sustainable Energy Transition (ICRSEtoSET)*, pages 1–6. IEEE, 2023.

[56] Mohammed Aidoud, Chams-Eddine Feraga, Mohcene Bechouat, Moussa Sedraoui, and Sami Kahla. Development of photovoltaic cell models using fundamental modeling approaches. *Energy Procedia*, 162:263–274, 2019.

[57] Tareq Kareri. Modeling and simulation of a hybrid pv/wind/battery storage off-grid power system. 2017.

[58] Muhammad H Rashid. *Power electronics handbook*. Butterworth-heinemann, 2017.

[59] Robert W Erickson and Dragan Maksimovic. *Fundamentals of power electronics*. Springer Science & Business Media, 2007.

[60] Fateh Slama. *Amélioration de l'intégration des énergies renouvelables au réseau électrique (smart grid)*. PhD thesis, 2021.

[61] Marian K Kazimierczuk. *Pulse-width modulated DC-DC power converters*. John Wiley & Sons, 2015.

[62] Ghadbane Ismail. *etude et réalisation d'un filtre actif parallèle en utilisant différentes stratégies de contrôle*. PhD thesis, Université Mohamed Khider de Biskra, Département: Electrotechnique, 2016.

[63] TETA Ali. *Investigation on Active Power Filter based on Z-Source Inverter Topology*. PhD thesis, University of de Djelfa-Ziane Achour, Département: Electrotechnique, 2021.

[64] T Burton, N Jenkins, D Sharpe, and E Bossanyi. Wind energy handbook, viewed 10 april 2023¡ https://www. academia. edu/27754946, 2001.

[65] Yumei Ma, Donghai Zhu, Ziqin Zhang, Xudong Zou, Jiabing Hu, and Yong Kang. Modeling and transient stability analysis for type-3 wind turbines using singular perturbation and lyapunov methods. *IEEE Transactions on Industrial Electronics*, 70(8):8075–8086, 2022.

[66] Bin Wu, Yongqiang Lang, Navid Zargari, and Samir Kouro. *Power conversion and control of wind energy systems*, volume 76. John Wiley & Sons, 2011.

[67] Jinghan Cui, Su Liu, Jinfeng Liu, and Xiangjie Liu. A comparative study of mpc and economic mpc of wind energy conversion systems. *Energies*, 11(11):3127, 2018.

[68] Siemens AG. Siemens wind turbine swt-2.3-108, 2011.

[69] Gabriele Michalke and Anca D Hansen. Modelling and control of variable speed wind turbines for power system studies. *Wind Energy: An International Journal for Progress and Applications in Wind Power Conversion Technology*, 13(4):307–322, 2010.

[70] Paul C Krause, Oleg Wasynczuk, Scott D Sudhoff, and Steven Pekarek. *Analysis of electric machinery and drive systems*, volume 2. Wiley Online Library, 2002.

[71] Henk Polinder, Frank FA Van der Pijl, G-J De Vilder, and Peter J Tavner. Comparison of direct-drive and geared generator concepts for wind turbines. *IEEE Transactions on energy conversion*, 21(3):725–733, 2006.

[72] Soltane Belakehal, Houcine Benalla, and Amar Bentounsi. Power maximization control of small wind system using permanent magnet synchronous generator. *Journal of Renewable Energies*, 12(2):307–319, 2009.

[73] Firuz Zare, Hamid Soltani, Dinesh Kumar, Pooya Davari, Hernan Andres Miranda Delpino, and Frede Blaabjerg. Harmonic emissions of three-phase diode rectifiers in distribution networks. *Ieee Access*, 5:2819–2833, 2017.

[74] MAZOUZ LAKHDAR. *Etude et analyse d'un système HVDC-VSC connecté à une ferme d'énergie éolienne*. PhD thesis, université djilali liabes, 2018.

[75] Colin Oates. Modular multilevel converter design for vsc hvdc applications. *IEEE Journal of Emerging and Selected Topics in Power Electronics*, 3(2):505–515, 2014.

[76] Vinod Kumar, Ranjan Kumar Behera, Dheeraj Joshi, and Ramesh Bansal. *Power electronics, drives, and advanced applications*. CRC Press, 2020.

[77] Anh-Vu Ho and Tae-Won Chun. Topology and modulation scheme for three-phase three-level modified z-source neutral-point-clamped inverter. *IEEE Transactions on Power Electronics*, 34(11):11014–11025, 2019.

[78] Dragan Jovcic. *High voltage direct current transmission: converters, systems and DC grids*. John Wiley & Sons, 2019.

[79] Danish Khan, Pengfei Hu, Salman Habib, Muhammad Waseem, Zhenzhi Lin, and Emad M Ahmed. A resonant damping control and analysis for lcl-type grid-connected inverter. *Energy Reports*, 8:911–928, 2022.

[80] Yao Zhou, Jinliang He, Jun Hu, Xingyi Huang, and Pingkai Jiang. Evaluation of polypropylene/polyolefin elastomer blends for potential recyclable hvdc cable insulation applications. *IEEE Transactions on Dielectrics and Electrical Insulation*, 22(2):673–681, 2015.

[81] Soledad Bernal-Perez, Salvador Ano-Villalba, Ramon Blasco-Gimenez, and Johel Rodriguez-D'Derlee. Efficiency and fault ride-through performance of a diode-rectifier-and vsc-inverter-based hvdc link for offshore wind farms. *IEEE Transactions on Industrial Electronics*, 60(6):2401–2409, 2012.

[82] Agustí Egea-Alvarez, Sajjad Fekriasl, Fainan Hassan, and Oriol Gomis-Bellmunt. Advanced vector control for voltage source converters connected to weak grids. *IEEE Transactions on Power Systems*, 30(6):3072–3081, 2015.

[83] HA Khan, Herbert HC Iu, and Victor Sreeram. Active and reactive power control of the electronically interfaced dg sources for the realization of a virtual power plant. In *IECON 2011-37th Annual Conference of the IEEE Industrial Electronics Society*, pages 808–813. IEEE, 2011.

[84] Saleh Elkelani Babaa, Matthew Armstrong, and Volker Pickert. Overview of maximum power point tracking control methods for pv systems. *Journal of Power and Energy Engineering*, 2014, 2014.

[85] IU UJU, AJ ATUCHUKWU, and OE EKEOPARA. Power system stability optimization using proportional-integral-derivative (pid) controller. 2021.

[86] Linbin Huang, Huanhai Xin, and Florian Dörfler. H-control of grid-connected converters: Design, objectives and decentralized stability certificates. *IEEE Transactions on Smart Grid*, 11(5):3805–3816, 2020.

[87] Wenping Zhang, Yiming Wang, Po Xu, Donghui Li, and Baosong Liu. A current control method for grid-connected inverters. *Energies*, 16(18):6558, 2023.

[88] Adrian Timbus, Marco Liserre, Remus Teodorescu, Pedro Rodriguez, and Frede Blaabjerg. Evaluation of current controllers for distributed power generation systems. *IEEE Transactions on power electronics*, 24(3):654–664, 2009.

[89] Remus Teodorescu, Frede Blaabjerg, Marco Liserre, and P Chiang Loh. Proportional-resonant controllers and filters for grid-connected voltage-source converters. *IEE Proceedings-Electric Power Applications*, 153(5):750–762, 2006.

[90] Daniel Nahum Zmood and Donald Grahame Holmes. Stationary frame current regulation of pwm inverters with zero steady-state error. *IEEE Transactions on power electronics*, 18(3):814–822, 2003.

[91] Waleed Al-Saedi, Stefan W Lachowicz, Daryoush Habibi, and Octavian Bass. Power flow control in grid-connected microgrid operation using particle swarm optimization under variable load conditions. *International Journal of Electrical Power & Energy Systems*, 49:76–85, 2013.

[92] Tidjani Mahni. *Etude et Conception d'un Filtre Actif Parallèle Triphasé à Quatre Fils en vue de sa Commande par des Méthodes d'Intelligence Artificielle*. PhD thesis, Université Mohamed Khider-Biskra, 2017.

[93] M Nabil, SM Allam, EM Rashad, et al. Modeling and design considerations of a photovoltaic energy source feeding a synchronous reluctance motor suitable for pumping systems. *Ain Shams Engineering Journal*, 3(4):375–382, 2012.

[94] Ayse Kocalmıs Bılhan and Erhan Akbal. Modelling and simulation of two-level space vector pwm inverter using photovoltaic cells as dc source. *International Journal of Electronics Mechanical and Mechatronics Engineering*, 2(4):311–317, 2012.

[95] Shweta Singh and AN Tiwari. Simulation and comparison of spwm and svpwm control for two level inverter. In *Conference paper, Madan Mohan Malaviya University of Technology, Gorakhpur (UP) India*, 2017.

[96] N DEBBAH and M DERBAL. Étude et commande d'un système hybride eolien photovoltaïque connecté au réseau avec stockage. contribution à l'amélioration de la qualité de l'énergie. *Mémoire du projet de fin d'études pour l'obtention du diplôme D'Ingénieur d'Etat en Électrotechnique, École Nationale Polytechnique, Alger*, 2013.

[97] J Prasanth Ram, N Rajasekar, and Masafumi Miyatake. Design and overview of maximum power point tracking techniques in wind and solar photovoltaic systems: A review. *Renewable and Sustainable Energy Reviews*, 73:1138–1159, 2017.

[98] Shijie Zhao, Tianran Zhang, Shilin Ma, and Miao Chen. Dandelion optimizer: A nature-inspired metaheuristic algorithm for engineering applications. *Engineering Applications of Artificial Intelligence*, 114:105075, 2022.

[99] Hind Djeghloud, Amar Bentounsi, and Hocine Benalla. Sub and super-synchronous wind turbine-doubly fed induction generator system implemented as an active power filter. *International Journal of Power Electronics*, 3(2):189–212, 2011.

[100] Yahia Bouzelata, Necmi Altin, Rachid Chenni, and Erol Kurt. Exploration of optimal design and performance of a hybrid wind-solar energy system. *International journal of hydrogen energy*, 41(29):12497–12511, 2016.

[101] AM El-Sebaii, MS Hamad, and AA Helal. A sensorless mppt technique for a grid-connected pmsg wind turbine system. 2013.

[102] Samir Kouro, Jose I Leon, Dimitri Vinnikov, and Leopoldo G Franquelo. Grid-connected photovoltaic systems: An overview of recent research and emerging pv converter technology. *IEEE Industrial Electronics Magazine*, 9(1):47–61, 2015.

[103] Liang Ji, Jiabin Shi, Qiteng Hong, Yang Fu, Xiao Chang, Zhe Cao, Yang Mi, Zhenkun Li, and Campbell Booth. A multi-objective control strategy for three phase grid-connected inverter during unbalanced voltage sag. *IEEE Transactions on Power Delivery*, 36(4):2490–2500, 2020.

[104] Ali M Eltamaly, AI Alolah, Hassan M Farh, and Hasan Arman. Maximum power extraction from utility-interfaced wind turbines. *New Developments in Renewable Energy*, pages 159–192, 2013.

[105] SA Zidi. *Contribution à l'étude des réseaux de transport d'énergie électrique à courant continu haute tension (CCHT) en régime dynamique*. PhD thesis, thèse de doctorat d'état en électrotechnique, Université Djillali Liabès de ..., 2005.

[106] Viktor Träff and Oscar Lennerhag. Modelling of vsc-hvdc for slow dynamic studies. 2013.

[107] Johel José Rodríguez D'Derlée. *Control strategies for offshore wind farms based on PMSG wind turbines and HVdc connection with uncontrolled rectifier*. PhD thesis, Universitat Politècnica de València, 2013.

[108] Subhasis Jhampati, Bhim Singh, and Amit Kumar. Optimal controller design for multilevel voltage source converter based hvdc system. In *2012 IEEE International Conference on Power Electronics, Drives and Energy Systems (PEDES)*, pages 1–6. IEEE, 2012.

[109] A Iván Andrade, Ramon Blasco-Gimenez, and G Ruben Pena. Distributed control strategy for a wind generation systems based on pmsg with uncontrolled rectifier hvdc connection. In *2015 IEEE International Conference on Industrial Technology (ICIT)*, pages 982–986. IEEE, 2015.

[110] Jinming Zou, Yi Han, and Sung-Sau So. Overview of artificial neural networks. *Artificial neural networks: methods and applications*, pages 14–22, 2008.

[111] Roheen Qamar and Baqar Ali Zardari. Artificial neural networks: An overview. *Mesopotamian Journal of Computer Science*, 2023:124–133, 2023.

[112] Lakhdar Mazouz, Sid Ahmed Zidi, Mohamed Khatir, Tahar Benmessaoud, and Slami Saadi. Particle swarm optimization based pi controller of vsc-hvdc system connected to a wind farm. *International Journal of System Assurance Engineering and Management*, 7(Suppl 1):239–246, 2016.

[113] Sul Ademi, Dimitrios Tzelepis, Adam Dysko, Sankara Subramanian, and Hengxu Ha. Fault current characterisation in vsc-based hvdc systems. In *13th International Conference on Development in Power System Protection 2016 (DPSP)*. IET, 2016.

[114] Sobhy S Dessouky, Mahmoud Fawzi, Hamed A Ibrahim, and Nagwa F Ibrahim. Dc pole to pole short circuit fault analysis in vsc-hvdc transmission system. In *2018 Twentieth International Middle East Power Systems Conference (MEPCON)*, pages 900–904. IEEE, 2018.

[115] Ashwini K Khairnar and P Shah. Dc line-to-ground fault analysis for vsc based hvdc transmission system. *Intl. Journal on Recent and Innovation Trends in Compt. and Comms.*, 5(6):773–778, 2017.

[116] Kellal Cherif, Mazouz Lakhdar, Kouzou Abdellah, Elottri Ahmed, and Karboua Djaloul. Fuzzy logic controller based maximum power point tracking using dc/dc boost converter for pv system. In *2022 19th International Multi-Conference on Systems, Signals & Devices (SSD)*, pages 1992–1997. IEEE, 2022.

[117] Hugues Renaudineau, Fabrizio Donatantonio, Julien Fontchastagner, Giovanni Petrone, Giovanni Spagnuolo, Jean-Philippe Martin, and Serge Pierfederici. A pso-based global mppt technique for distributed pv power generation. *IEEE Transactions on Industrial Electronics*, 62(2):1047–1058, 2014.

[118] Cherif Kellal, Lakhdar Mazouz, and Ahmed Elottri. Apply modified pso algorithm technology based on mppt of a photovoltaic system under condition difference. *International Journal of Advanced Studies in Computers, Science and Engineering*, 11(11):11–22, 2022.

[119] Seyedali Mirjalili, Seyed Mohammad Mirjalili, and Andrew Lewis. Grey wolf optimizer. *Advances in engineering software*, 69:46–61, 2014.

[120] Sudhakiran Ponnuru, R Ashok Kumar, and NM Jothi Swaroopan. Gwo-based mppt controller for grid connected solid oxide fuel cell with high step up dc-dc converter. *Indonesian Journal of Electrical Engineering and Computer Science*, 23(3):1794–1803, 2021.

# Appendix A

## A.1 MPPT method

### A.1.1 Perturbation and observation (P&O) method

This method is one of the simplest and most widely used in PV systems, as it relies on measuring voltage and current to track changes in power ($\Delta P$) caused by a change in voltage ($\Delta V$). The perturbed values are adjusted in one direction until the increase in power stops. If the power variation ($\Delta P/\Delta V$) is lower than zero, it indicates that the operating point is shifting away from the MPP, and the disturbance is reversed to bring the system back towards the MPP. When the perturbation and the energy change are in the same direction, either positive or negative, the perturbation is positive, and if they differ in direction, the perturbation is negative [55, 116]. Figure A.1 presents a flowchart of this method. This process can be summarized in the table A.1.

| **Sr.No** | $\Delta P$ | $\Delta V$ | $V_{\mathbf{ref}}$ | **D** |
|---|---|---|---|---|
| First case | $> 0$ | $> 0$ | Increase | Decrease |
| Second case | $> 0$ | $< 0$ | Decrease | Increase |
| Third case | $< 0$ | $> 0$ | Decrease | Increase |
| Fourth case | $< 0$ | $< 0$ | Increase | Decrease |

Table A.1: Summary of the P&O Method

#### A.1.1.1 MPPT based on PSO algorithm

The PSO algorithm is inspired by the social and cooperative behavior of various animals, such as flocks of birds, and was mathematically formulated by James Kennedy and Russell Eberhart in 1995 [117]. This method is based on a swarm of particles, The PSO algorithm is applied by calculating the output power by measuring the current and voltage of the PV array and fitting the algorithm to the duty cycle that controls the switching on the boost

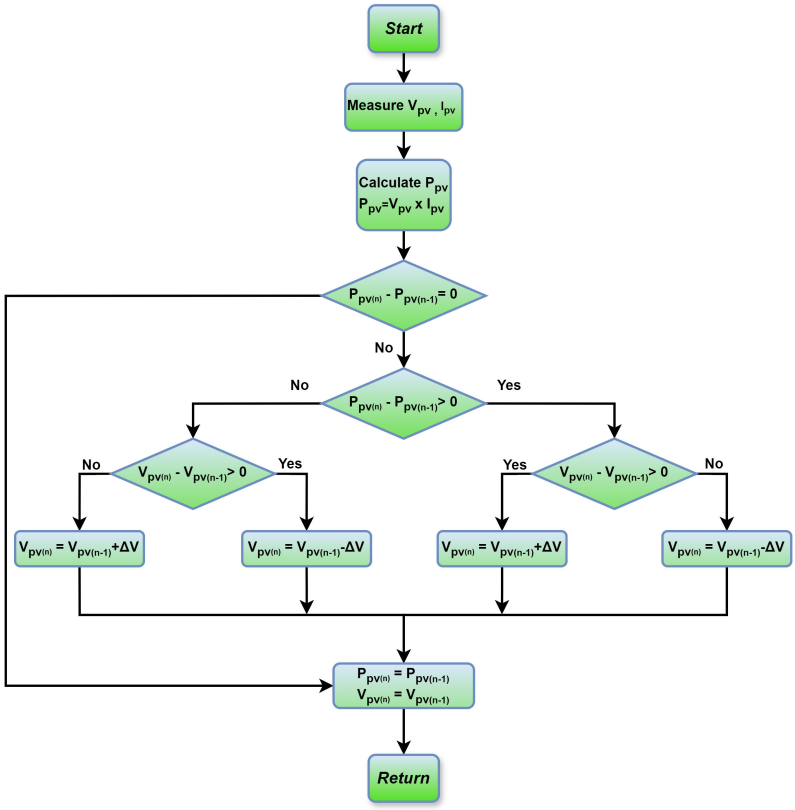


Figure A.1: The fowchart of *P&O* MPPT

converter to reach the MPP, The duty cycle of a boost converter represents the swarm particle [118],, and the flowchart of this method is illustrated in Figure A.2 .

The velocity and position of each duty cycle can be calculated through the Eq A.1 and A.2,respectively.

$$\mathbf{v}_i^{k+1} = \omega \cdot \mathbf{v}_i^k + r_1 \cdot c_1 \cdot \left(\mathbf{d}_{\text{best},i}^k - \mathbf{d}_i^k\right) + r_2 \cdot c_2 \cdot \left(\mathbf{G}_{\text{best},i}^k - \mathbf{d}_i^k\right) \tag{A.1}$$

$$\mathbf{d}_i^{k+1} = \mathbf{d}_i^k + \mathbf{v}_i^k \tag{A.2}$$

Where $v_i^{k+1}$,$v_i^k$ and $d_i^{k+1}$,$d_i^k$ are the velocity and position of each particle in the current and previous iteration,respectively.k is number of repetitions, $\omega$=0.45 is factor of the inertia weight of velocity and $c_1$=0.9 and $c_2$=1.25 are cognitive and social parameters, while $r_1$=$r_2$=0.35 are random variables between 0 and 1.

The search process is conducting through some steps as below:

1. Initialize the PSO parameters, and initialize the particle position and velocity.

2. Measure the current and voltage to calculate the output power of the PV panel.

3. Each particle explores potential solutions based on a randomly generated molecular value. It then compares its current value with the previous and upcoming values, referred to as $(X_i^{k-1})$ and $(X_i^k)$, respectively, to identify and select the optimal option. The particles' positions represent the duty cycle of the DC-DC converter, where the current power $P(d_i^k)$ is evaluated against the previous power vector $P(d_{best,i}^{k-1})$. If the current power is higher, $P(d_{best,i}^k)$ is updated, and the corresponding duty cycle is saved in the vector $d_{best,i}^k$. Otherwise, the current power is checked against the best global power value, $G_{best,i}^k$. If the current value exceeds $G_{best,i}^k$, the global power is updated, and the corresponding duty cycle is stored in the variable $G_{best,i}^k$. This procedure continues until all particles have been assessed.

4. Update the velocity and position of each particle in the swarm by equation A.1 and A.2.

5. Finally, the evaluation of all particles and number of Iteration is verified, if the criterion is not satisfied, the iteration number is increased and returns to the objective evaluation function , However, if the criterion is satisfied, the maximum power tracking process is concluded.

#### A.1.1.2 MPPT based on GWO algorithm method

The Gray Wolf Optimizer (GWO) algorithm emulates the social structure and collective hunting strategies of gray wolves in nature. This optimization technique is organized into a four-level hierarchy: alpha ($\alpha$), beta ($\beta$), delta ($\delta$), and omega ($\omega$). The alpha represents the dominant leader, responsible for decision-making and guiding the hunt. In the alpha's absence, the beta assumes leadership responsibilities, providing support and enforcing the alpha's decisions, while the delta assists both the alpha and beta in managing the pack.

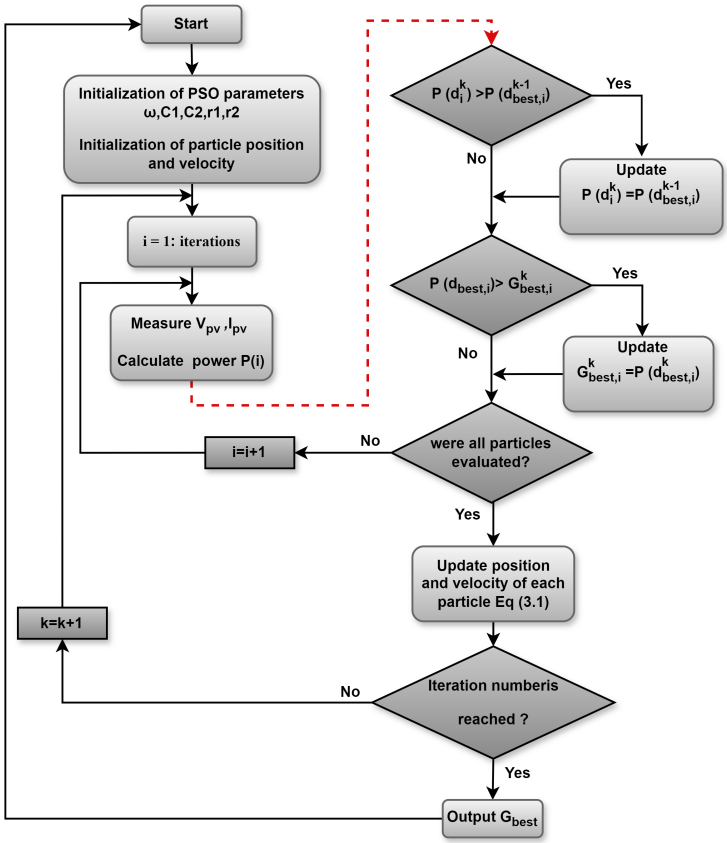


Figure A.2: The fowchart of *PSO* MPPT

The omega wolves occupy the lowest rank, following the guidance of the higher-ranking members [119, 120]. The hunting behavior is expressed mathematically by the following equation:

$$\begin{cases} \vec{d} = \left| \vec{C} \times \vec{x}_p(i) - \vec{x}_p(i) \right| \\ \vec{x}(i+1) = \vec{x}_p(i) - \vec{A} \times \vec{d} \end{cases} \tag{A.3}$$

where, $i$ denotes the current iteration, while $\vec{x}_p$ represents the position vector of the target (prey). The vector $\vec{x}$ corresponds to the position of a gray wolf, and $\vec{A}$ and $\vec{C}$ are coefficient vectors used to guide the wolves' movement toward the target. These coefficients are computed using the following expressions:

$$\begin{cases} \vec{A} = 2\vec{a} \times \vec{r}_1 - \vec{a} \\ \vec{C} = 2 \times \vec{r}_2 \end{cases} \tag{A.4}$$

In this algorithm, the parameter $a$ decreases linearly from 2 to 0 over the course of the iterations, facilitating a balance between exploration and exploitation. The terms $r_1$ and $r_2$ are randomly generated vectors within the range $[0, 1]$, introducing stochastic behavior into the search process. The leader, identified as the most optimal candidate solution at a given iteration, guides the search by having the most accurate estimate of the prey's position.

To adapt the algorithm for MPPT, each gray wolf in the population is associated with a candidate duty cycle D is defined as follows:

$$d_i(k+1) = d_i(k) - A \times D \tag{A.5}$$

Thus, the fitness function utilized within the GWO algorithm is defined as follows:

$$P\left(d_1^k\right) > P\left(d_i^{k-1}\right) \tag{A.6}$$

In this context, $P$ denotes the output power, $d$ represents the duty cycle, $i$ indicates the index of the current gray wolf, and $k$ corresponds to the iteration number. The flowchart of MPPT using the GWO algorithm is illustrated in Figure A.3.

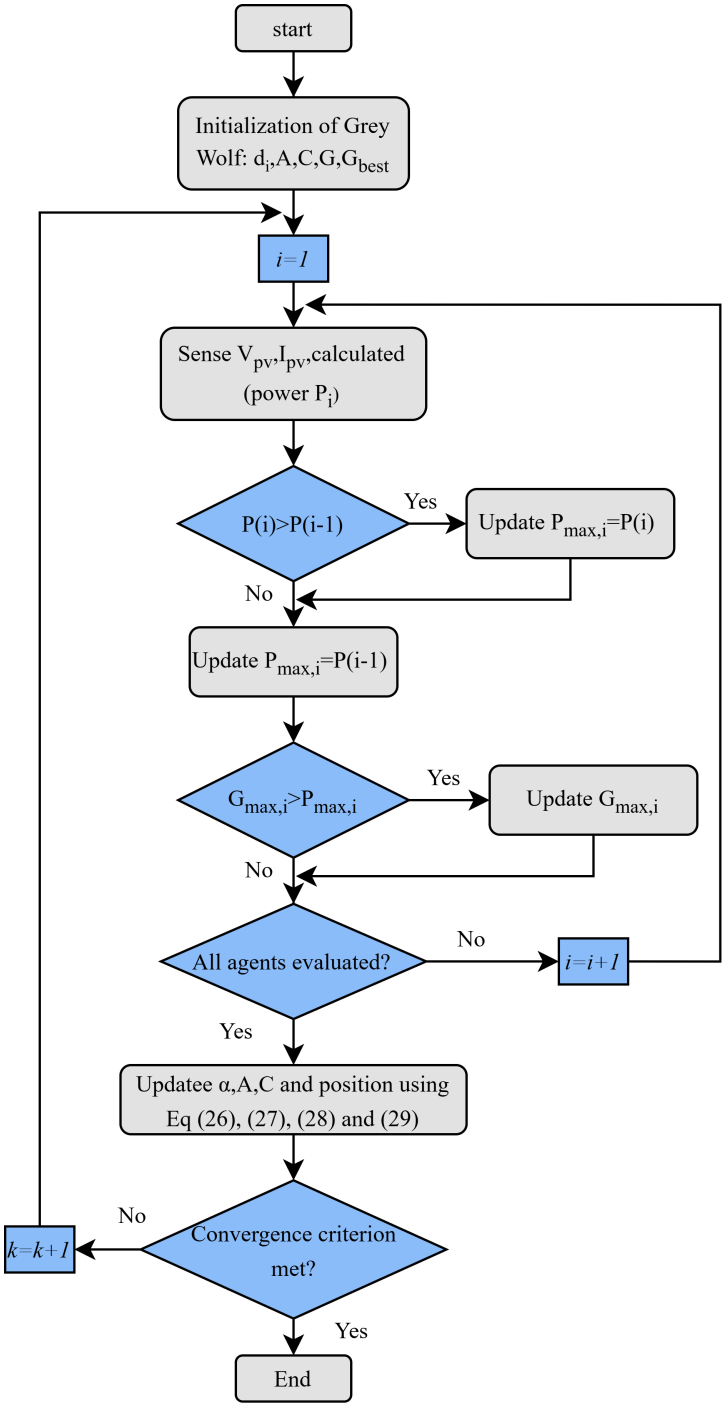


Figure A.3: The flowchart of the MPPT based on the GWO method.

# Appendix B

The table below shows the technical specifications of the photovoltaic module used in simulating of enhancing the power of PV systems through the MPPT methods mentioned previously.

| Parameters | Values |
|---|---|
| Maximum operating power ($P_{mp}$) | 335.205 W |
| Maximum operating voltage ($V_{mp}$) | 57.3 V |
| Maximum operating current ($I_{mp}$) | 5.85 A |
| Open-circuit voltage ($V_{oc}$) | 67.9 V |
| Short-circuit current ($I_{sc}$) | 6.23 A |
| Temperature coefficient of $V_{oc}$ | $-0.4$ %/°C |
| Temperature coefficient of $I_{sc}$ | 0.05 %/°C |
| Photogenerated current ($I_{ph}$) | 6.2584 A |
| Diode saturation current ($I_D$) | $7.7254 \times 10^{-10}$ A |
| Diode ideality factor (N) | 1.2076 |
| Shunt resistance ($R_{sh}$) | 587.7606 Ω |
| Series resistance ($R_s$) | 0.28856 Ω |

Table B.1: Specification of PV Panel (SPR-X21-335-BLK)

The table below shows the values of the boost converter components in simulating of enhancing the power of PV systems.

| Parameters | Values |
|---|---|
| Input capacitance ($C_{in}$) | 1000 $\mu$F |
| Output capacitance ($C_{out}$) | 255 $\mu$F |
| Inductor (L) | 3.1 mH |
| Switching frequency ($f_{sw}$) | 5 kHz |
| Load ($R_{load}$) | 39.65 Ω |

Table B.2: Components of a boost converter

The table below shows the parameters used in the simulation for improving HVDC-VSC performance with FFNN-based PI control under hybrid renewable energy operation.

| System | Parameters | Value |
|---|---|---|
| Utility grid | Utility grid voltage | 50 KV |
| | System frequency (f ) | 50 Hz |
| | Supply resistance | 1.7857 |
| | Supply inductance | 0.0398 H |
| | DC link capacitor of Vdc | 0.048 F |
| Wind system | Maximum wind power | 100 KW |
| | Stator phase resistance of PMSG (Rs) | 0.0369 |
| | Armature inductance of PMSG Ld = Lq | $3.667 \times 10^{-4} H$ |
| | Number of poles | 4 |
| | Leakage flux | 0.253 Wb |
| HVDC-VSC | DC link Power | $3 \times 10^{6} VA$ |
| | DC link voltage | 3000 V |
| | DC link capacitor | 0.068 F |
| | Line length | 25 Km |

Table B.3: The parameter values of system

The table below shows all PI controller gains used in the system used in the simulation for improving HVDC-VSC performance with FFNN-based PI control under hybrid renewable energy operation.

| Gains | Outer Control Loop | | Inner Control Loop | |
|---|---|---|---|---|
| | $K_{i1}$ | $K_{p1}$ | $K_{i2}$ | $K_{p2}$ |
| HRES | 800 | 7 | 20 | 0.3 |
| VSC1 | 275 | 2.5 | 8 | 0.1 |
| VSC2 | 40 | 0.3 | 8 | 0.1 |

Table B.4: Parameters of the PI Gains

The table below shows the technical specifications of the PV modules used in the simulation for improving HVDC-VSC performance with FFNN-based PI control under hybrid renewable energy operation.

| Parameters | KD205GX-LP | SPR-305-WHT |
|---|---|---|
| Maximum power ($P_{mp}$) | 100.7 kW | 100.1 kW |
| Maximum voltage ($V_{mp}$) | 54.7 V | 26.6 V |
| Maximum current ($I_{mp}$) | 5.58 A | 7.71 A |
| Open-circuit voltage ($V_{oc}$) | 64.2 V | 33.2 V |
| Short-circuit current ($I_{sc}$) | 5.96 A | 8.36 A |
| Number of series cells ($N_s$) | 5 | 8 |
| Number of parallel cells ($N_p$) | 66 | 61 |

Table B.5: The specifications of PV modules

# Abstract

In light of the continuously increasing global energy demand and the environmental constraints imposed on fossil fuels, renewable energy sources, such as solar and wind power, have emerged as indispensable and sustainable alternatives. Nevertheless, the fluctuating and intermittent nature of these sources presents complex technical challenges that impede their seamless and reliable grid integration, compounded by the inherent limitations of High Voltage Alternating Current (HVAC) transmission systems. To overcome these challenges, this thesis presents the modeling, control, and integration of Hybrid Renewable Energy Systems (HRES) with Voltage Source Converter-based High Voltage Direct Current (VSC-HVDC) transmission systems. This technology is leveraged for its capability to independently control active and reactive power, as well as its high efficiency and low power losses in long-distance energy transmission. From a technical perspective, this research focuses on implementing advanced control strategies and intelligent algorithms to optimize system performance and maximize efficiency. For Photovoltaic (PV) systems, improved Maximum Power Point Tracking (MPPT) techniques based on metaheuristic optimization algorithms are proposed specifically, Particle Swarm Optimization (PSO), Grey Wolf Optimizer (GWO), and Dandelion Optimizer (DO). These ensure maximum power extraction under rapidly changing solar irradiance and temperature conditions. Furthermore, robust control frameworks are applied to wind energy systems utilizing Permanent Magnet Synchronous Generators (PMSG) to optimize electromagnetic torque and regulate the DC-link voltage. Finally, the stability of the VSC-HVDC systems is enhanced by integrating Feed-Forward Neural Networks (FFNNs). This intelligent approach improves the dynamic management of active and reactive power flow, guarantees high power quality, and maintains voltage stability amidst environmental and operational fluctuations.



**Keywords:** Renewable energy, Wind power, Photovoltaic power, HVDC-VSC, HVAC, PMSG.

# Résumé

Face à la croissance continue de la demande énergétique mondiale et aux contraintes environnementales imposées aux combustibles fossiles, les sources d'énergie renouvelable, telles que l'énergie solaire et éolienne, se sont imposées comme des alternatives indispensables et durables. Néanmoins, la nature fluctuante et intermittente de ces sources pose des défis techniques complexes qui entravent leur intégration fluide et fiable au réseau électrique, des défis par ailleurs aggravés par les limites inhérentes aux systèmes de transmission en courant alternatif à haute tension (HVAC).Pour surmonter ces défis, cette thèse présente la modélisation, la commande et l'intégration de systèmes hybrides d'énergie renouvelable (HRES) avec des systèmes de transmission en courant continu à haute tension basés sur des convertisseurs de source de tension (VSC-HVDC). Cette technologie est exploitée pour sa capacité à contrôler indépendamment la puissance active et réactive, ainsi que pour sa grande efficacité et ses faibles pertes de puissance lors de la transmission d'énergie sur de longues distances.D'un point de vue technique, cette thèse se concentre sur la mise en œuvre de stratégies de commande avancées et d'algorithmes intelligents afin d'optimiser les performances du système et d'en maximiser l'efficacité. Pour les systèmes photovoltaïques (PV), des techniques améliorées de suivi du point de puissance maximale (MPPT) basées sur des algorithmes d'optimisation métaheuristiques sont proposées plus spécifiquement l'optimisation par essaim particulaire (PSO), l'optimisation du loup gris (GWO) et l'optimisation du pissenlit (DO). Celles-ci garantissent une extraction maximale de l'énergie sous des conditions d'irradiance solaire et de température variant rapidement. De plus, des structures de commande robustes sont appliquées aux systèmes d'énergie éolienne utilisant des générateurs synchrones à aimants permanents (PMSG) pour optimiser le couple électromagnétique et réguler la tension du bus continu (DC-link). Enfin, la stabilité des systèmes VSC-HVDC est renforcée par l'intégration de réseaux de neurones à propagation avant (FFNNs). Cette approche intelligente améliore la gestion dynamique du flux de puissance active et réactive, garantit une qualité d'énergie élevée et maintient la stabilité de la tension face aux fluctuations environnementales et opérationnelles.



**Mots-clés:** Énergie renouvelable, Énergie éolienne, Énergie photovoltaïque, HVDC-VSC, HVAC, PMSG.



# ملخص

في ظل التزايد المستمر للطلب العالمي على الطاقة والقيود البيئية المفروضة على الوقود الأحفوري، برزت مصادر الطاقة المتجددة، كطاقة الشمس والرياح، كبدائل حتمية ومستدامة. ومع ذلك، فإن الطبيعة المتقلبة والمتقطعة لهذه المصادر تفرض تحديات تقنية معقدة تعيق دمجها السلس والموثوق في الشبكة الكهربائية، وتتفاقم هذه التحديات بسبب القيود الكامنة في أنظمة نقل التيار المتناوب عالي الجهد (HVAC). للتغلب على هذه التحديات، تقدم هذه الأطروحة نمذجة، تحكم، ودمج أنظمة الطاقة المتجددة الهجينة (HRES) مع أنظمة نقل التيار المستمر عالي الجهد المعتمدة على محولات مصادر الجهد (VSC-HVDC). يتم استغلال هذه التقنية لقدرتها على التحكم المستقل في الطاقة الفعالة والتفاعلية، فضلاً عن كفاءتها العالية ومفاقيدها المنخفضة للطاقة في عمليات النقل لمسافات طويلة. من الناحية التقنية، يركز هذا البحث على تنفيذ استراتيجيات تحكم متقدمة وخوارزميات ذكية لتحسين أداء النظام وزيادة كفاءته إلى أقصى حد. بالنسبة للأنظمة الكهروضوئية (PV)، تم اقتراح تقنيات محسّنة لتتبع نقطة الاستطاعة القصوى (MPPT) تعتمد على خوارزميات التحسين الميتاهيروستيكية، وتحديداً: تحسين سرب الجسيمات (PSO)، ومُحسّن الذئب الرمادي (GWO)، ومُحسّن الهندباء (DO). تضمن هذه التقنيات استخلاص أقصى قدر من الطاقة في ظل التغيرات السريعة لظروف الإشعاع الشمسي ودرجات الحرارة. علاوة على ذلك، يتم تطبيق هياكل تحكم متينة لأنظمة طاقة الرياح التي تستخدم المولدات التزامنية ذات المغناطيس الدائم (PMSG) بهدف تحسين العزم الكهرومغناطيسي وتنظيم جهد وصلة التيار المستمر (DC-link). أخيراً، يتم تعزيز استقرارية أنظمة VSC-HVDC من خلال دمج الشبكات العصبية ذات التغذية الأمامية (FFNNs). يعمل هذا النهج الذكي على تحسين الإدارة الديناميكية لتدفق الطاقة الفعالة والتفاعلية، ويضمن جودة عالية للطاقة، ويحافظ على استقرار الجهد الكهربائي في ظل التقلبات البيئية والتشغيلية.



**الكلمات المفتاحية:** الطاقة المتجددة، طاقة الرياح، الطاقة الكهروضوئية، نظام التيار المستمر عالي الجهد ذو محول مصدر الجهد، نظام التيارالمتردد عالي الجهد، المولد المتزامنة ذو المغناطيس الدائم.